KAUNAS UNIVERSITY OF TECHNOLOGY

SHANKER GANESH KRISHNAMOORTHY

ATTENUATION OF VIBRATION BY CONTROLLING THE MECHANICAL TRANSMISSIBILITY OF ELECTROMECHANICAL DEVICES

Doctoral dissertation
Technological Science, Mechanical Engineering (T 009)

2021, Kaunas

This doctoral dissertation was prepared at Kaunas University of Technology, Faculty of Mechanical Engineering and Design, Department of Production Engineering during the period of 2015–2020. The studies were supported by Research Council of Lithuania.

Scientific Supervisor:

Assoc. Prof. Dr. Inga SKIEDRAITĖ (Kaunas University of Technology, Technological Sciences, Mechanical Engineering, T 009)

Doctoral dissertation has been published in:
http://ktu.edu

Editor:

Aurelija Gražina Rukšaitė (Publishing Office "Technologija")

KAUNO TECHNOLOGIJOS UNIVERSITETAS

SHANKER GANESH KRISHNAMOORTHY

VIBRACIJŲ SLOPINIMAS KONTROLIUOJANT ELEKTROMECHANINIŲ ĮTAISŲ MECHANINĮ REZONANSĄ

Daktaro disertacija
Technologijos mokslai, mechanikos inžinerija (T 009)

2021, Kaunas

Disertacija rengta 2015-2020 metais Kauno technologijos universiteto mechanikos inžinerijos ir dizaino fakultete, gamybos inžinerijos katedroje. Mokslinius tyrimus rėmė Lietuvos mokslo taryba.

Mokslinis vadovas:

Doc. dr. Inga SKIEDRAITĖ (Kauno technologijos universiteto, Technologijos mokslai, Mechanikos inžinerija, T 009)

Interneto svetainės, kurioje skelbiama disertacija, adresas:
http://ktu.edu

Redagavo:

Aurelija Gražina Rukšaitė (leidykla “Technologija”)

CONTENTS

NOMENCLATURE
LIST OF FIGURES
LIST OF TABLES

ABBREVIATIONS

VCM	Voice coil motor
DVB	Dynamic vibration absorber
APVM-TMD	Adaptive-passive variable mass tuned mass damper
TMD (SAVM-TMD)	Self-adaptive variable mass
EMD	Electromagnetic dampers
2D	Two-dimensional
SDOF	Single degree of freedom
PZT	Lead Zirconate Titanate
ECD	Eddy current dampers
FRFs	Frequency response functions
LVI	Linear vibration isolators
N-EMSD	Nonlinear electromagnetic shunt damping
PLA	Polylactic Acid

NOMENCLATURE

M	Mass
K	Stiffness
c	Damping coefficient
F	Force
t	Time
ω	Angular frequency
x	Displacement
$\dot{x}$	Velocity
ζ	Damping ratio
ω_n	Natural frequency
L	Length
w	Width
t_p	Total thickness of the triple layer bender
t_{p1}	Thickness of piezo layer 1
t_{p2}	Thickness of piezo layer 2
t_m	Thickness of middle copper shim
S_1^p	Strain in the direction of length of piezoelectric element
T_1^p	Stress acting in the direction of length of piezoelectric element
D_3^p	Electric displacement
s_{11}^E	Compliance at constant electric field
d_{31}	Transverse piezoelectric coefficient
ε_{33}^T	Permittivity at constant stress of the piezoelectric layers
S_1^m	Strain in the direction of length of elastic element
T_1^m	Stress acting in the direction of length of elastic element
s_{11}^m	Compliance of elastic element
u^p	Internal energy density
u^{lower}	Internal energy density of the upper piezo layer
u^{upper}	Internal energy density of the lower piezo layer

k_c	Curvature of the bimorph bender
v	Vertical displacement of the mid plane
k_{31}^2	Electromechanical coupling factor
E_3	Applied electric field
Q	Electric charge
C_{free}	Capacitance of a free triple layer bender
V	Applied electric voltage
F	External tip force
M_o	External moment
p	Uniform load
α	Angular deflection
δ	Tip deflection
V_{1m}	Amplitudes of voltage V_1
V_{2m}	Amplitudes of voltage V_2
(ωt)	Phase angle of V_1
$(\omega t \pm \emptyset)$	Phase angle of V_2
B_r	Remanence of magnet
H_c	Coercivity of magnet
μ_m, μ	Permeability of magnet
μ	Coefficient of friction
W_g	Width of the flux plate
l_m	Length of magnet
w_m	Width of magnet
A_m	Area of magnet
A_g	Area of the gap
H	Magnetizing field
μ_0	Permeability of space
$\vec{J}$	Current density induced in the copper walls
σ	Conductivity of conducting material
M_0	Magnetization per unit length

δ	Thickness of copper tube
σ_m	Surface charge density
ρ_m	The magnetic volume charge density

LIST OF FIGURES

LIST OF TABLES

INTRODUCTION

Research relevance

Low-amplitude vibration with a frequency ranging from 0.1 Hz to 1kHz can be defined as micro-vibration [1], [2]. Micro-vibration that propagates in mechanical systems can result in different problems which can lead to performance degradation of sensitive appliances [3], [4]. Therefore, the mitigation of micro-vibration is an essential topic that engineers and scientists have to take into consideration when developing new mechanical systems. A precise solution is therefore required for the design and control of mechanical systems because the micro-vibration that occurs with a frequency of up to 1 kHz can affect the performance of sensitive measuring tools used with payloads of spacecraft [3], [5] which are used for measuring the proximity (distance) or any other equipment used for visual imaging.

Passive vibration suppression and isolation is the first recommended approach to try to reduce these unwanted disturbances. From the practical standpoint, the reduction of the vibration level in a sensitive location of a structure can be achieved by placing the equipment on the appropriate mountings. However, high impacts and more extended services affect the mountings thus resulting in changes in the system’s resonance. The change in resonance enhances the propagation of micro-vibration.

In this case, the active damper solution is a good approach for solving micro-vibration mitigation issues. For example, a six-axis voice coil motor (VCM)-based platform [6] dynamic isolation system is one of the best proactive solutions. However, these mechanisms depend on synchronized working of different links. These issues can be curbed by implementing agile isolation, which involves using a shape-memory alloy or smart materials, such as piezoelectric elements.

The above-mentioned systems can provide optimal results, but the nature of their mechanical design is complicated, and the involvement of various parts that have to work in the synchronized increases the systems’ dependency factor. Here, the dependency factor refers to the dependency of hardware on control systems.

In recent years, significant contribution has been made towards the attenuation of micro-vibration so that to support the performance of sensitive payloads in space applications. This is in large part due to the fact that space structures possess low damping, which results in a long decay time for vibration. Therefore, this research will consider a sample problem related to space applications.

Similar research was also carried in Kaunas University of Technology by V. Ostaševičius, A. Bubulis, R. Gaidys, V, Barzdaitis, V. Jurėnas, R. Jonušas, K. Ragulskis and other researchers.

Aim and objective of the research

The aim of the research is to investigate and develop a method for attenuating micro-vibration by controlling the mechanical resonance characteristics of a transitional structure.

To achieve the aim, the following tasks should be fulfilled:

1. Scientific literature review analysis related to various methods used for vibration attenuation.
2. To evaluate theoretically and experimentally the process to control micro-vibration by varying the structural stiffness of the smart composite beam.
3. To conduct theoretical investigation of a method for varying the stiffness of an interconnecting system through controlled friction.
4. To evaluate theoretically and experimentally the design of electromagnetic dashpots which are created by using already existing systems, such as eddy current dampers and actuated coil systems.
5. To compare and to evaluate the research results in order to select the most suitable technique for practical application.

Scientific novelty

1. A theoretical model to explain the response of piezoelectric bimorph by considering two input voltages with phase shifts is presented in this research. Also, the experimental research demonstrating 50% alleviation in flutter is possible by directly shunting active and passive layers of a piezoelectric bimorph bender and without additional shunt circuit.
2. Theoretical evaluation of a novel method to attenuate vibration by controlling frictional force between two steel plates under the influence of varying magnetic flux. Also, the application of the current approach is evaluated in this research.
3. The influence of counterforce in varying stiffness of the system for an eddy current damper and a two-coil electromagnetic dashpot is theoretically and experimentally evaluated.

Statements to defend

1. A theoretical model to explain the response of piezoelectric bimorph by considering two input voltages with phase shifts can be developed. The 50% alleviation in flutter is possible by directly shunting active and passive layers of a piezoelectric bimorph bender and without any additional shunt circuit.
2. The novel method is able to attenuate vibration by controlling the frictional force between two steel plates under the influence of varying magnetic flux.
3. Out of the three methods investigated in this research, the utilization of the PZT bimorph beam or a similar smart composite structure is the most supporting technique for fulfilling the current research aim

Research methods

First, problem analysis will be conducted in order to identify the parameters necessary for investigating the proposed aim. Significance will be given to the working principle of electromechanical devices – based on structural, Coulomb and viscous methods – to attenuate vibration.

Each method will be investigated by using a theoretical model which will be evaluated through *MATLAB*, *COMSOL 5.3* and *FEMM4.2* software. For the design of the test setup and analysis, *SolidWorks 2016* software will be used. The designed test setup will be developed in the 3D printing lab under the Faculty of Mechanical Engineering and Design of Kaunas University of Technology.

The experimental analysis will be performed in order to verify the theoretical research which was carried out at the laboratory of the Institute of Mechatronics at Kaunas University of Technology. For excitation of the test setups, an electrodynamic shaker will be used and excited with the help of a wave generator (DG1032) and an amplifier (EPA-104). The amplitude of vibration on the test setup will be analyzed by using an optical sensor (OFV-505) connected to a vibrometer-controller (OFV-5000) and a PicoScope for data collection. Vibration analysis will also be performed using a laser displacement sensor from *Keyence LK Series*, LK-G82. In order to minimize the influence of external vibration, entire tests will be performed in their complete form on an optical table.

Practical value

This research gives a theoretical and practical insight into three different methods for attenuating micro-vibration by controlling the mechanical transmissibility of electromechanical devices and by controlling the stiffness of the system. The different vibration attenuation techniques proposed and investigated throughout this research are suitable for applications related to altered gravity and varying atmospheric pressure, thus making them also suitable for space applications. Furthermore, these simple methods can be used for the design and development of packing technologies which require attenuation of vibration for the transportation of fragile and valuable materials.

Research approbation

The results of this research have been published in two scientific journals, indexed on the *Web of Science* database with an impact factor. One article is under the national database, while the other one is under an international database. Furthermore, three articles have been published in conference proceedings, and one further article has been published as a peer-reviewed scientific publication. The results of this research were also presented in two international conferences: WSEAS: Applied and Theoretical mechanics 2017, Cambridge, and Mechanika 2017, Kaunas, Lithuania.

Structure of the dissertation

This thesis consists of problem analysis, three main chapters, discussion on the achieved results, general conclusions, references and the author’s publication list and other achievements.

The first section, which involves problem analysis, helps understand the issue that the research is addressing and clarifies the research aim. This chapter also explains the reason for choosing the following working principles to attenuate micro-vibration: structural vibration attenuation, reduction of micro-vibration through a controlled frictional process, and a viscous system that uses an electromagnetic device.

The second section addresses the topic related to the attenuation of micro-vibration through the use of smart composite structures. Here, the mathematical parameters required to understand the dynamic behavior of a piezoelectric bimorph bender as a response to input voltage and unmediated shunting are investigated theoretically and experimentally.

The third section elaborates on the topic related to a method that controls friction between two steel plates by using magnetic flux, thereby controlling micro-vibration. The work showcases a novel theoretical model that analyzes the aim of the research and verifies it theoretically with the help of *FEMM* and *MATLAB*.

The fourth section investigates the counter-force method that attenuates micro-vibration by using an electromagnetic device. Here, a specific test setup is developed to create micro-vibration, and 3D printed parts are used to minimize the effect of external magnetic attractive forces from ferrous materials. In this section, theoretical and experimental analyses regarding the force generated from electromagnetic devices are carried out. Also, an experimental part is included so that to study the heat generated in such systems.

The fifth section opens a discussion on each presently investigated technique and on the implementation process.

Finally, the work is concluded by a conclusion part which summarizes the accomplishments of the research work. At the end of the dissertation, a list of publications and other achievements obtained during the current research period are presented.

The volume of dissertation is 106 pages; it features 71 figures and 9 tables.

1. METHODS FOR MICRO-VIBRATION CONTROL

1.1 Problem Analysis

There have been significant contributions towards the attenuation of micro-vibration to support the performance of sensitive payloads in space applications [3], [5], [7]. Sensitive payloads in spacecraft can include mid-wave infrared surveillance sensors, laser communication devices and astronomical telescopes. Due to the low damping properties of space structures, micro-vibration that occur with frequencies of up to 1 kHz can affect the efficiency of sensitive payloads. Therefore, the micro-vibration that occurs with a low amplitude and frequencies of up to 1 kHz cannot be neglected and requires a precise solution [8]. In this case, the primary sources of micro-vibration are the onboard equipment – such as cryocoolers and data storage devices – and the operation of electric motors, a gyroscope, thrusters, and reaction wheels. Thus, comprehensive understanding of the vibration amplitude and the frequency with which the wave promulgates through the structures is essential for keeping sensitive payloads free from quivers. The latest research and devices promise almost cent percent attenuation. However, these devices are questionable in terms of the design, control, dependency and maintenance required in the long run.

The objective of this research is to examine the requirements needed to satisfy the design and implementation of devices for relaxation dampers; see Fig. 1.1. It will focus on the idea of reducing the long-term dependency and maintenance factors of such devices. This research will therefore investigate a novel idea: to attenuate micro-vibration by shifting the resonance extremity of a transitional strut.

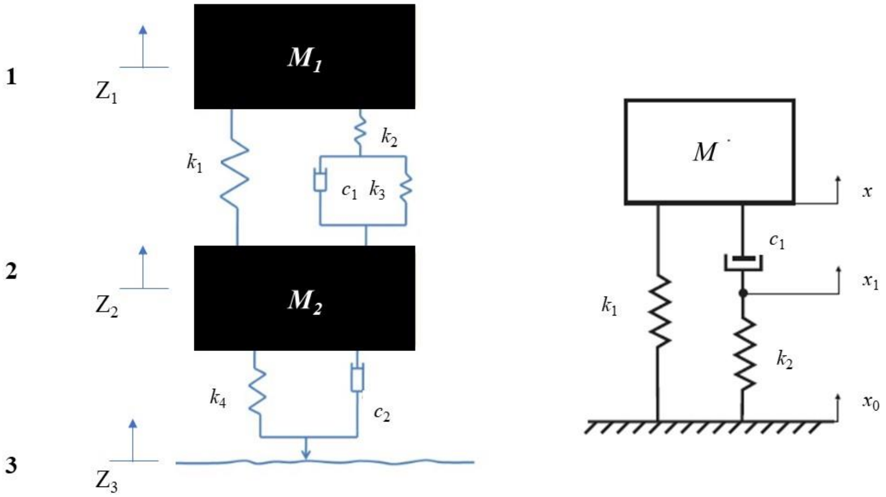

Fig. 1.1 Types of dampers: (a) skyhook damper: 1 – vehicle body; 2 – bogie; 3 – uneven path; (b) relaxation damper

Further study of the current research aim requires a model; therefore, a correlative design based on work by dr. V. Preda [9] and dr. D. Addari [10] is considered. This design is comprised of an active plate coupled to an interface plate with four isolators. The active plate is the primary source for vibration, and the interface plate is the target source that requires the attenuation of micro-vibration. The four isolators help to attenuate micro-vibration and keep the interface plate stable. Additionally, the interface plate is suspended on a string in order to emulate microgravity in the two-dimensional (2D) context. In this research, emulation of microgravity is not an ongoing concern. The concept of dr. V Preda and team test setup is shown in Fig. 1.2.

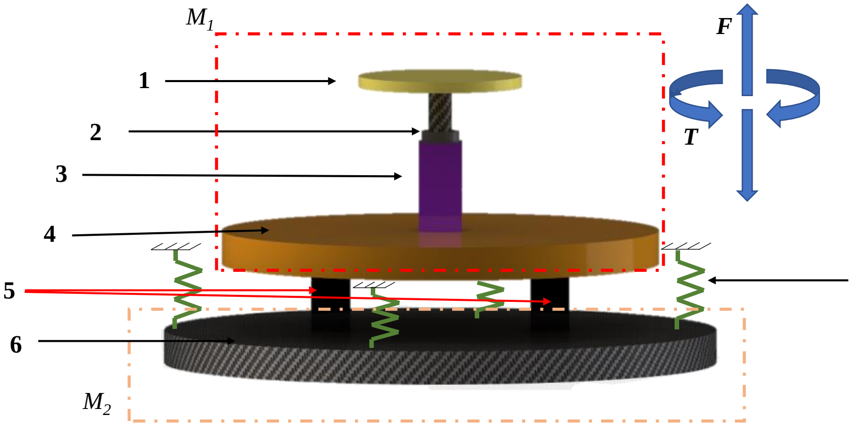

Fig. 1.2 Concept of dr.V. Preda and team test setup: 1 – reaction wheel; 2 – bearing; 3 – motor; 4 – active plate; 5 – isolator; 6 – interface plate; 7 – mechanism to emulate micro gravity in 2D

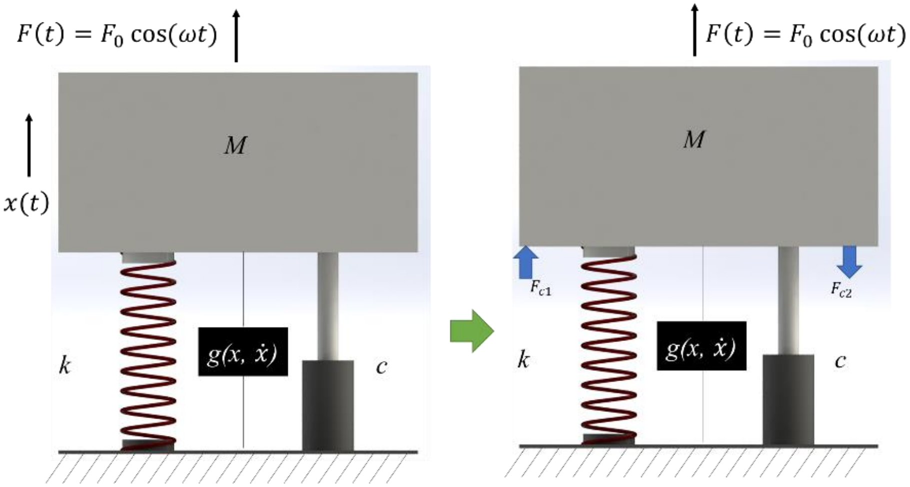

(a) (b)

Fig. 1.3 Lumped model representation: (a) considering dr. V. Preda's work as relaxation dampers; (b) implementation of a counter force to the system

In order to scrutinize the research aim by considering the problem – as mentioned in Dr. V. Preda's work – that the excited harmonic force travels from the active plate to the interface plate due to the disturbance from the reaction wheel, we simplify the system and represent it in the form of a lumped model (a single degree of freedom (SDOF)) and as a relaxation damper setup (Fig. 1.3 (a)).

In Fig. 1.3 (a) and (b), force $F(t) = F_0 \cos(\omega t)$ represents the lateral vibration experienced by the interface plate of mass M. The intermediate structure connecting the interface plate and the active plate is considered to have a stiffness of k and is expected to have a low damping coefficient of c. Also, in reality, nonlinearity could be involved in the system. Therefore, a nonlinear element $g(x, \dot{x})$ is also considered, which has a function of displacement x and velocity $\dot{x}$.

The damping coefficient and stiffness of a structure can change over time, thus resulting in the propagation of micro-vibration and resonance. This research analyzes and investigates methods featuring the capacity to attenuate micro-vibration by implementing linear counterforce $F_c = F_{c1} + F_{c2}$ almost equal in magnitude to the amplitude of excitation force F_0.

The respective governing equation for the SDOF system, Fig. 1.3 (b), is represented as:

$$\ddot{x} + 2\,\zeta\omega_n\dot{x} + \omega_n x \pm (F_{c1} + F_{c2}) + g(x,\dot{x}) = F_0 \cos(\omega t) \tag{1}$$

Here, $\zeta = c/(2\,m\omega_n)$ – damping ratio, and $\omega_n = \sqrt{\frac{k}{M}}$ – natural frequency.

1.2 Different methods that could be used to create counter force *F_c*

The principle of creating the counterforce of F_c can be achieved through several ways, such as

a. Adaptive-passive variable mass tuned mass damper [11]
b. Vibration and noise control using a shunted piezoelectric transducer [12]
c. practical dampers with the frictional effect [13], [14]
d. electromagnetic dampers [15].

1.2.1 Adaptive-passive variable mass tuned mass damper (APVM-TMD)

One of the classical and effective methods to reduce vibration in a structure without any isolation between the target and the vibration source is obtained with a dynamic vibration absorber (DVB) [1–5]. Figure 1.4 (a) illustrates the schematic diagram of the latest research on the adaptive-passive variable mass tuned mass damper (APVM-TMD) which is used for vibration attenuations in the footbridge, and Fig 1.4 (b) represents the respective experimental setup. The results obtained from the research are shown as a response plot sampled from the primary structure, Fig. 1.5 (a) acceleration response spectrum and Fig. 1.5 (b) displacement response spectrum. Figure 1.5 (a) shows that the maximum dynamic amplification factor of ‘without TMD case’ is 70.60, ‘mistuned TMD case’ is 26.66, and ‘retuned TMD case’ is 14.90. Here, the maximum dynamic amplification factor of the retuned TMD case has a decrement of 78.90% compared to ‘without TMD case’, and a decrement of 44.11% compared to the ‘mistuned TMD case’ is observed. From Fig. 1.5 (b) displacement response spectrum, the maximum dynamic amplification factor of the ‘retuned TMD case' has a decrement of 76.70% and 42.20%, respectively. The conclusion of this research was retuned; TMD has an excellent effect in controlling both acceleration and displacement responses.

The APVM-TMD system can retune itself by its variable mass. It is feasible and effective from the engineering point of view. Also, regarding the case of robustness, APVM-TMD is better than the self-adaptive variable mass tuned mass damper (SAVM-TMD). But, for a smaller system, it is hard to implement because of the required space and the necessity for larger amplitude displacements for the proper functioning of the system APVM-TMD. But, for large systems, the required results when using DVB are effectively achieved.

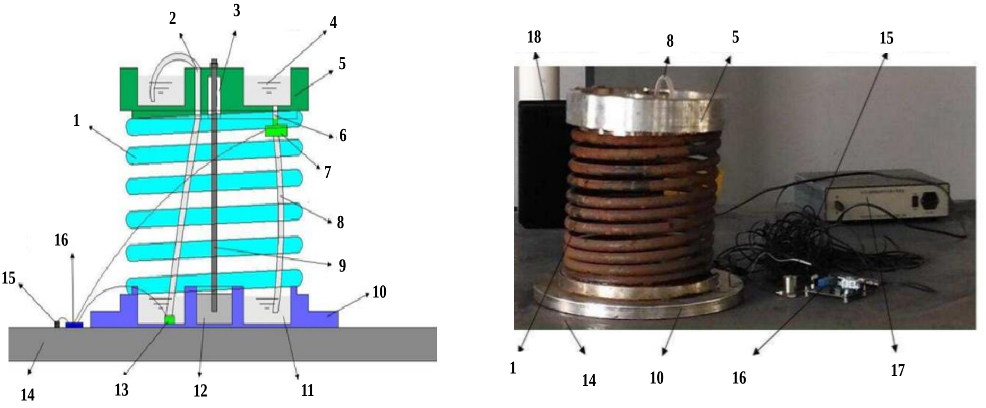

(a) (b)

Fig. 1.4 Dynamic vibration absorber (DVB): (a) Schematic diagram of the APVM-TMD which is used for vibration attenuations in foot-bridge and (b) its experimental setup [11] Where: 1 – spring; 2 – channel 1; 3 – channel 2; 4 – upper water tank; 5 – mass; 6 – channel 3; 7 – electromagnetic valve; 8 – water pipe; 9 – iron bar; 10– pedestal; 11 – bottom of water tank; 12 – container; 13 – water pump; 14 – primary structure; 15 – acceleration sensor; 16 – microcontroller; 17 – data acquisition machine; 18 – computer

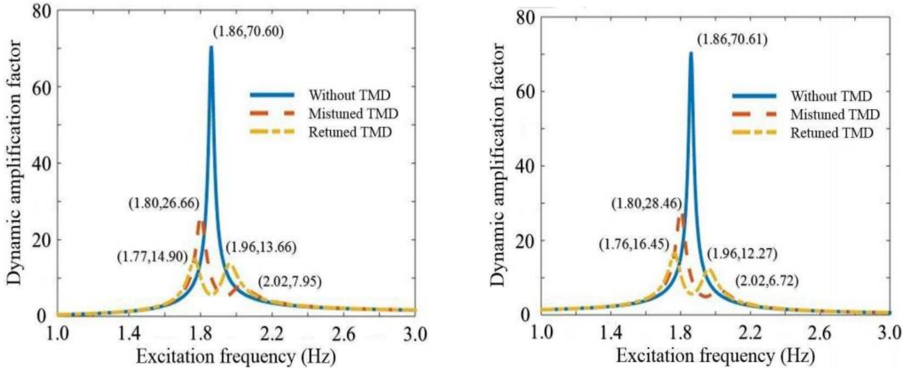

(a) (b)

Fig. 1.5 Response plot: (a) acceleration response spectrum; (b) displacement response spectrum [11]

1.2.2 Vibration control using piezoelectric transducers

Piezoelectric tools have been designed and implemented throughout the past few decades. These tools help with easy integration by abbreviating the number of implementation modules needed, thereby reducing the mass budget and increasing the power efficiency, which results in intelligible implementation. Such piezoelectric systems are capable of mitigating micro-vibration with high frequency and low-frequency ranges. The most recognized PZT devices used for the attenuation of vibration include piezoelectric Stewart platforms [6], piezoelectric inertial actuators [20], and multipurpose dynamic isolation systems [21].

For the current investigation, we are interested in a system wherein a flexible structure covered with a piezoelectric material is used for controlling the stiffness to mitigate quivers. There have been studies clarifying the static and dynamic models required for a segment of piezoelectric actuators bonded or embedded in flexible structures [22]. Research by Bailey and Ubbard also discusses surface-mounted piezoelectric dampers for reducing the free vibration decay time of cantilever beams [23]. Additionally, there have been various studies on the optimal control of vibration in flexible smart structures using piezo sensors and actuators [19, 20]. The latest research work corresponding to the current investigation involves an intelligent panel with time-varying shunted piezoelectric patch absorbers [26] and a smartboard of piezoelectric patch vibration absorbers [27], Fig. 1.6. All these works required an intricate control circuit to achieve promising results [12] and focused on the phenomena of dissipation of energy through electrical circuits rather than emphasizing the mechanism of controlling the stiffness of the structure.

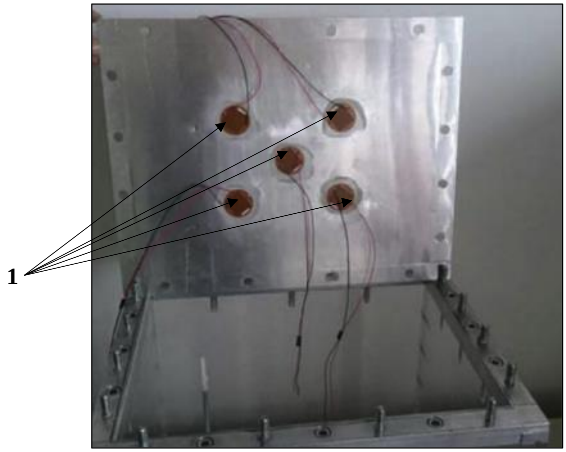

Fig. 1.6 A smartboard of piezoelectric patch vibration absorbers: 1 – piezoelectric patches [27]

Attenuation of micro-vibration by controlling the stiffness of the structure is considered in the research with smart folded beam platforms [8] using a composite structure, see Fig. 1.7. The smart folded platforms are used for passive and active attenuation of micro-vibration. The platform consists of four folded continuous beams arranged in three dimensions. Here, the reaction wheel or a source of vibration is mounted to this mechanism, and an investigation is done for frequency and response analysis by varying the number of folds and the thickness of vertical beams. The obtained results concluded that lower frequency attenuation is possible by increasing the number of folds and by decreasing the thickness of the blade. Also, the work stated that vibration suppression under a wide variety of loading conditions is effective by using the optimal control.

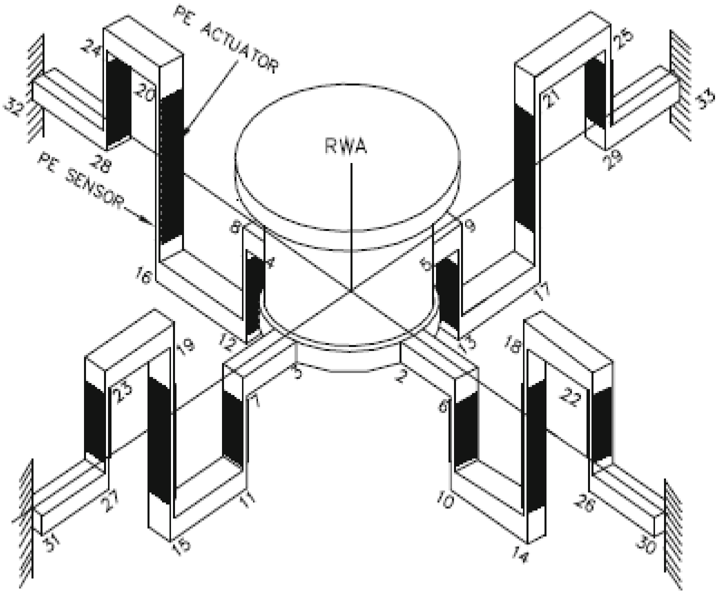

Fig. 1.7 Smart folded beam [8]

1.2.3 Vibration attenuation with the frictional effect

Coulomb dampers are widely used in the structural system to reduce vibration. The normal force between the contact areas is the most important design parameter for the development of Coulomb dampers, and it is often assumed to remain constant in most applications [28–33].

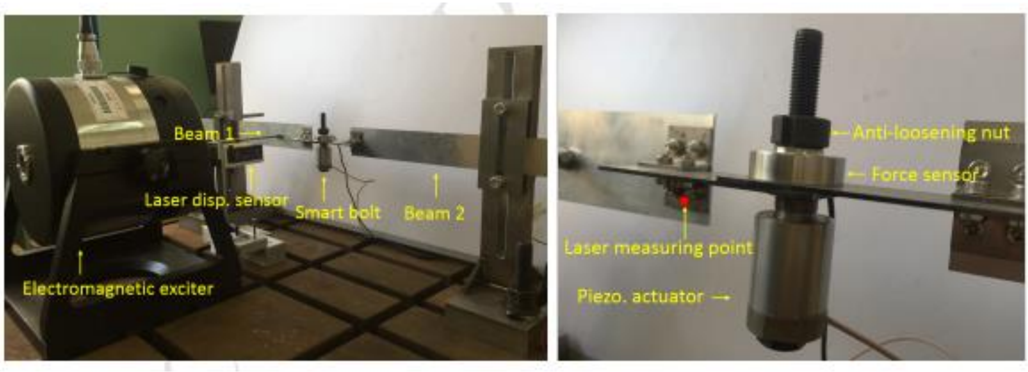

Fig. 1.8 Experimental setup: design of semi-active dry friction dampers for steady-state vibration [14]

Yet, the normal force can be time-varying, for example if the direction of the vibratory displacement is not parallel to the friction surface. There are research works [14], [31], [34] stating that the damping performance can be altered when the normal load is time-varying (Fig. 1.8), and the effect strongly depends on the dynamic coupling between the normal force and the relative displacement (Fig. 1.9).

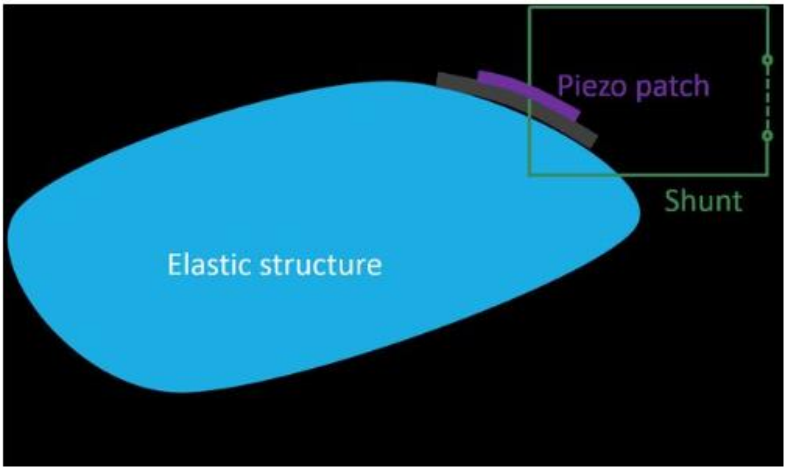

Fig. 1.9 Investigation of the vibration of a blade with friction damper [31]

The frictional force exists as the opposing force when two surfaces slide over each other. The applied force required to push a surface over another surface becomes trivial when the frictional force reduces. The condition of increased friction is inevitable for good grip between surfaces. The roughness between the two surfaces can be improved by using various strategies [35–37], by creating more adhesive or rougher points of contact, or by pressing the two surfaces harder, or by removing lubrication between the surfaces. The current research investigation will be conducted to improve the normal force between two steel surfaces by implementing magnetic flux.

1.2.4 Electromagnetic dampers

For smaller systems, electromagnetic dampers (EMD) are significant alternatives to generate controlled counter forces. EMDs can be sub-classified as passive and active dampers [38]. Among passive dampers, the most commonly used ones are eddy current dampers [39–42]. Figure 1.10 illustrates the experimental setup of a novel design of eddy current dampers (ECD) for vibration suppression in robotic milling. Figure 1.11 represents the cross-sectional scheme of ECD. Here, the results show cased damping of 15.5% in the *x*-axis and 22.1% in the *z*-axis for the peaks of the tool tip frequency response functions (FRFs) caused by the milling tool modes. One main disadvantage of this system is that the obtained damping result can be reduced if any of the parameters related to the feed force on the tool changes resulting in poor machining.

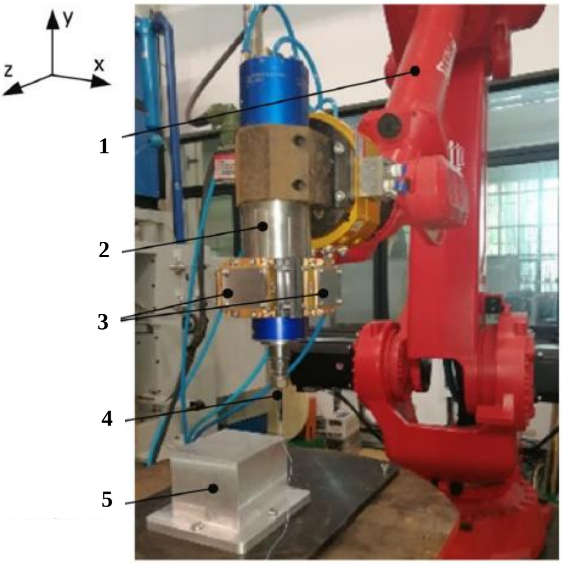

Fig. 1.10 Experimental setup of design of eddy current dampers for vibration suppression in robotic milling [41]: 1 – Comau robot; 2 – spindle; 3 – ECDs; 4 – milling tool; 5 – work piece

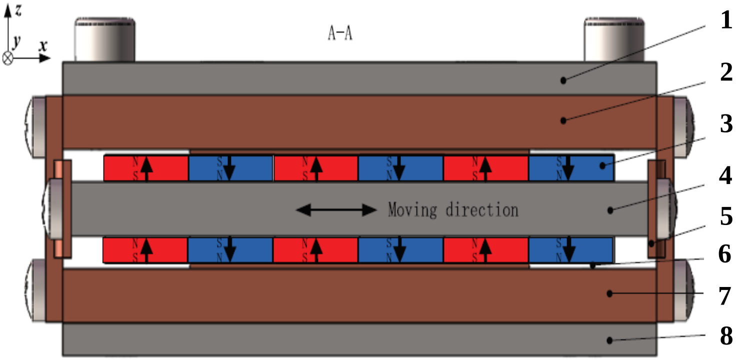

Fig. 1.11 Cross sectional view of ECD used vibration suppression in robotic milling [41]: 1 – upper steel plate; 2 – upper copper plate; 3 – permanent magnet; 4 – middle steal plate; 5 – spring; 6 – air gap; 7 – lower copper plate; 8 – lower steel plate

As a replacement of the traditional and passive absorbers, delayed resonators are also used [43], [44]. They belong to the class of active vibration absorbers with enhanced efficiency and flexibility.

A coil system is always involved for shunt electromagnetic damping, where the resonance characteristic of the dynamic mechanical system is matched with the electrical properties of the coil system, and an electrical circuit is used to achieve attenuation [39], [45–50]. Figure 4.3 represents the experimental test setup of linear vibration isolators (LVI) with nonlinear electromagnetic shunt damping (N-EMSD). This work was able to explain that the transmissibility of LVI with N-EMSD decreases with the increase of the excitation amplitude in the resonance region.

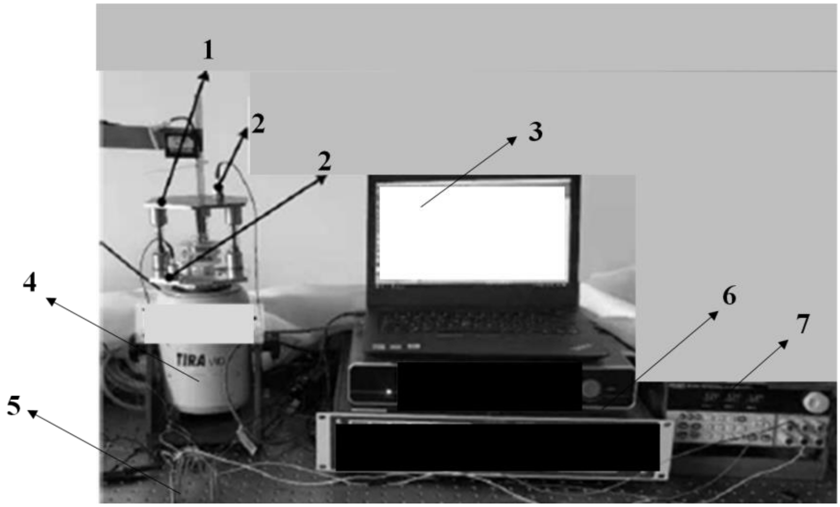

[redacted]

[redacted]

Fig. 1.12 Experimental setup of nonlinear electromagnetic shunt damping [15]: 1 – LVI with N-EMSD; 2 – accelerometer; 3 – computer; 4 – shaker; 5 – shunt circuit; 6 – power amplifier; 7 – DC power

Other possible research which could also define the use of generating counterforces for vibration control involves electromagnetic devices along with mass tuned dampers [51–54].

1.3 Current research

In the area of the current research, Kaunas University of Technology (KTU) has also contributed significant results. One of the recent research contributions from KTU was regarding the study to obtain response data related to dynamic behavior of vibrating beam with respect to changing cross sectional areas [55]. In this research, it was observed that the location of the changed cross sections influences energy dissipation in the structure and could be used for damping structural vibrations.

The experimental research on controlling vibrations in micro-cantilever beams using Electrorheological fluid (ERF) [56] gives an insight into the controllability of the vibration characteristics of a micro-piezoelectric transducer with ERF support. Another work on tuning the natural frequencies of a system by using magnetic rheological fluid (MRF) [57] used for the energy generator can also be included under the scope of the current research.

When it comes to electromagnetic devices, the work on the generator to create vibratory forces [58] based on permanent magnet interaction explains the new type of vibrations exciters whose operation is based on the forces developed by permanent magnets interacting between the input and output members of the dynamical system.

However, the above listed research works do not emphasize the control of mechanical transmissibility [16], [59], [60] by the control of stiffness *k*. Other research work [61–64] covers the current topic from the side of controls but rarely considers the perspective of generating additional forces to vary stiffness, to attenuate vibrations.

The current research therefore attempts to cover the idea that vibration can be attenuated by controlling the mechanical transmissibility by the control of stiffness K by implementing counter forces. The current research aim will be investigated and evaluated for:

a. Structural attenuation (smart composite structure).

b. Controlled Coulomb attenuation.

c. Controlled counterforce to attenuate micro-vibration while using an electromagnetic device.

2.THEORETICAL AND EXPERIMENTAL INVESTIGATION TO ATTENUATE MICRO-VIBRATION BY VARYING THE RESONANCE EXTREMITY OF PIEZOELECTRIC BIMORPH CANTILEVER

The attenuation of micro-vibration by shifting the resonance extremity of a transitional structure is theoretically and experimentally investigated in this section. The proposed research aim is analyzed by utilizing a classical cantilever piezoelectric bimorph (or trimorph) bender, wherein the resonance extremity of a cantilever composite brace is inspected by direct shunting of the active and passive layers in the absence of external shunt circuits.

Based on the research of the smart folded beam (Fig. 1.6) and considering the work by V. Preda from the problem analysis point of view (Fig. 1.2), for the current investigation, we shall consider a beam-type structure that connects the active plate and the interface plate (Fig. 2.1). Figure 2.1 represents a straightforward conceptual mechanical design for manipulating the implementation of the current research aim: attenuation of micro-vibration by shifting the resonance extremity of a transitional structure. When choosing such a model, the orientation of transitional composite braces is salient, and the ambiguous response of the system (as it concerns quiver in axial and lateral space) requires clarification. These aspects shall be examined in detail as part of future research work.

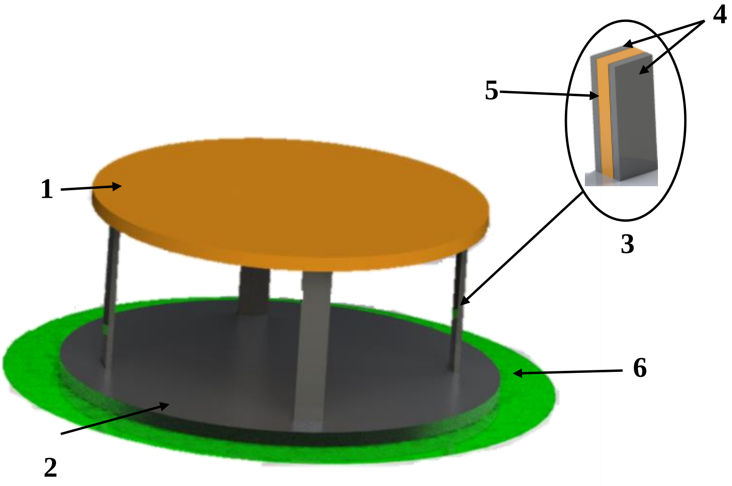

Fig. 2.1 Considered conceptual mechanical design of the beam-type structure that connects the active plate and the interface plate: 1 – active plate; 2 – interface plate; 3 – isolator; 4 – smart material; 5 – interconnecting structure; 6 – support area

In the ongoing investigation, the emphasis is on evaluating and understanding the process for attenuating shudder propagation through a connecting structure that couples two platforms, effected by controlling the stiffness of the connecting structure. This problem can be investigated by considering the coupling brace as a smart composite structure. As such, the coupling structure contemplated in the conceptual mechanical design (Fig. 2.1) can be further simplified as a traditional cantilever piezoelectric bimorph mechanism, as illustrated in Fig. 2.2.

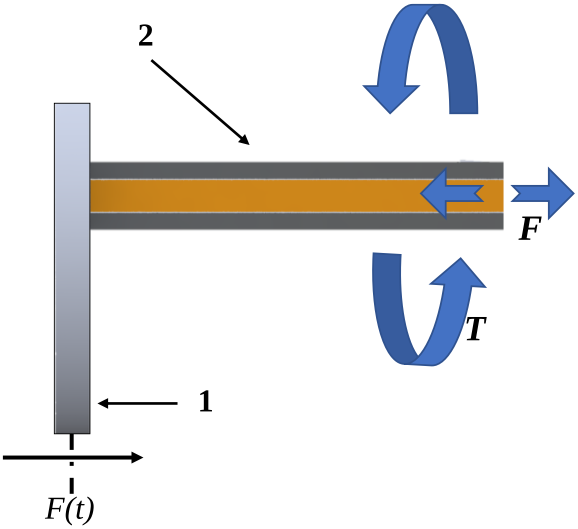

Fig. 2.2 Classical piezoelectric bimorph cantilever mechanism: 1 – excitation surface; 2 – PZT cantilever setup

The reasons to consider a classical piezoelectric bimorph cantilever mechanism for further research are the following:

a. to investigate the characteristics of the input voltage and the response of a piezoelectric bimorph, which will be useful for the further development of the conceptual design, see Fig. 2.1.
b. to attenuate micro-vibration by shifting the resonance characteristic of a transitional structure; it can be investigated by using direct shunting of the passive and active layers.
c. to evaluate the response of a smart composite beam by using the currently existing analytical methods

For the above listed reasons, the coupling structure considered in the conceptual mechanical design was simplified as a traditional cantilever piezoelectric bimorph mechanism.

2.1. Formulation of the electromechanical characteristics of piezoelectric bimorph beam

In order to investigate the proposed idea to control the stiffness of intermediate links, a simple bimorph cantilever setup is considered. Therefore, this section will theoretically investigate the electromechanical characteristics of a piezoelectric bimorph beam.

The research work conducted by J.K. Ajitsaria [65] highlighted three modelling methods for bimorph bender. They are the electrical equivalent circuit model, the energy conversion model, and the coupled field model. The coupled field model exhibited the best results as the electrical equivalent circuit failed to demonstrate the dynamics involved in the vibration of the piezoelectric bimorph bender, whereas the energy conversion model was unable to represent the effects of an electrical load on the damping behavior. For the current research, the dynamic part plays a major role; therefore, the energy conservation model [66] is used to study the contemporary mechanism. In the current section, the constitutive equation and the respective matrix form for a piezoelectric bimorph bender will be analyzed by using the energy conservation model.

For the investigation, we shall consider a piezoelectric bimorph bender consisting of an elastic layer sandwiched between two active piezoelectric layers (Fig. 2.3). For modelling, it is considered that two piezoelectric layers are connected in parallel, and each piezoelectric layer possesses the same polarization direction. The middle elastic layer is considered as a copper shim.

For numerical and experimental evaluation, the dimensions of the piezoelectric bimorph bender must satisfy the following conditions [66]: such that length L is greater than width w, and w is greater than total thickness t_p of the triple layer bender. The total thickness of the bimorph bender can be written as: $t_p = t_{p1} + t_m + t_{p2}$, where t_{p1} is the thickness of piezo layer 1, t_{p2} is the thickness of piezo layer 2 and t_m is the thickness of the middle copper shim.

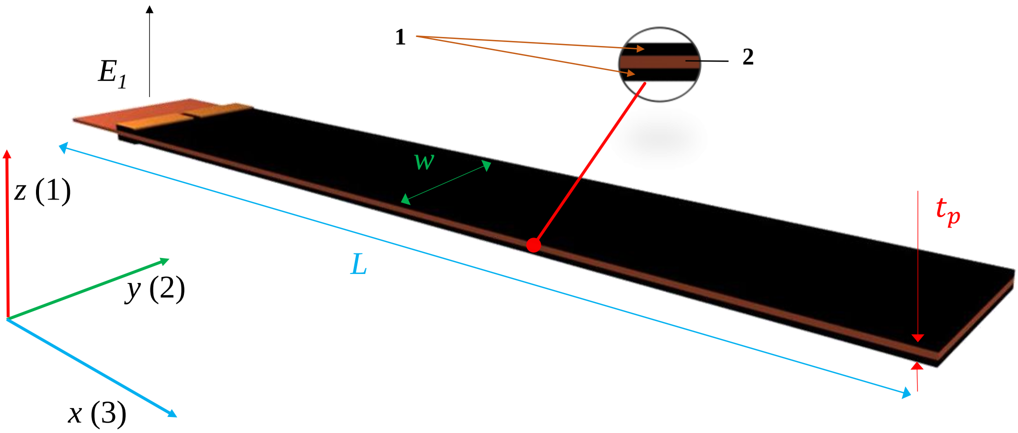

Fig. 2.3 Piezoelectric bimorph with an elastic layer in between: 1 – piezoelectric layers; 2 – copper pad; *L* – length; *w* – width; *tp* – total thickness of the triple layer bender

We assume an electrical field E_1 applied across the thickness direction of the bimorph bender (Fig. 2.3) with the polarity parallel to the upper and lower piezoelectric layer. The constitutive equation for the upper and lower piezo layer varies with the polarization direction. Since the polarity of the upper and lower layers is similar, the respective constitutive equation for both layers can be expressed by using Equations (2) and (3). The constitutive equation for the elastic layer of the bimorph bender is given by Equation (4).

$$S_1^p = s_{11}^E T_1^p + d_{31} E_3; \tag{2}$$

$$D_3^p = d_{31} T_1^p + \varepsilon_{33}^T E_1; \tag{3}$$

$$S_1^m = s_{11}^m T_1^m; \tag{4}$$

where the subscript *p* denotes the piezoelectric element, and subscript *m* denotes the elastic element. S_1^p– strain in the direction of the length of the piezoelectric element; T_1^p – stress acting in the direction of the length of the piezoelectric element; D_3^p – electric displacement; s_{11}^E – compliance at constant electric field; d_{31} – transverse piezoelectric coefficient; ε_{33}^T – permittivity at constant stress of the piezoelectric layers; S_1^m – strain in the direction of the length of the elastic element; T_1^m – stress acting in the direction of the length of the elastic element, and s_{11}^m – compliance of the elastic element.

Electric field E_3 is applied across the thickness direction of the bimorph bender with its polarity parallel to the lower and the upper piezoelectric layer, so the contraction of both layers should happen. Here, the deformation of the two piezoelectric layers is constrained by the copper pad, and bending will be produced in the whole structure. The external forces or the base vibration can also bend the triple layer bender. The extensional strain in the bimorph bender is continuous in the thickness direction as there is perfect bonding between the piezoelectric layers and the elastic layers.

The total internal energy density was studied by considering an infinitesimally small volume element in the piezoelectric material and applying the thermodynamic equilibrium [66]. The internal energy density of the upper and the lower piezo layer is given by:

$$u^p = u^{lower} = u^{upper} = \frac{1}{2} S_1^p T_1^p + D_3^p E_3. \tag{5}$$

$$u^{lower} = u^{upper} = \frac{1}{2} s_{11}^E \left(T_1^p\right)^2 + d_{31} E_3 T_1^p + \frac{1}{2} \varepsilon_{33}^T {E_3}^2. \tag{6}$$

The internal energy density for the middle elastic layer can be expressed as:

$$u^{middle} = \frac{1}{2} s_{11}^m (T_1^m)^2. \tag{7}$$

Thus, the total energy for the bimorph bender by volume integration is obtained as:

$$U_{total} = U^{upper} + U^{middle} + U^{lower} = \iiint (u^{upper} + u^{middle} + u^{lower})\, dxdydz. \tag{8}$$

To solve Equation (8), the curvature of bimorph bender k_c should be evaluated under different bending conditions [66], where the curvature of the bimorph bender can be defined as:

$$k_c = \frac{d^2 v}{dx^2}; \tag{9}$$

where *v* is the vertical displacement of the mid plane.

Now, for the sake of further simplification of extensional strain – S_1 and stress – T_1, the total internal energy of the upper, middle and lower layers will be:

$$U^{upper} = U^{lower} = \frac{1}{2}\int_0^L \int_0^w \left[\frac{1}{12}\,\frac{1}{s_{11}^E} k_c^2\left(3t_m^2 t_p + 6t_m t_p^2 + 4t_p^3\right) + \left(\varepsilon_{33}^T - \frac{1}{s_{11}^E} d_{31}^2\right) E_3^2 t_p\right] dxdz. \qquad (10)$$

$$U^{middle} = \int_0^L \int_0^w \left[\frac{Lw}{24}\,\frac{1}{s_{11}^m} k^2 t_m^3\right] dxdz. \qquad (11)$$

The simplified total internal energy of the bimorph bender will be:

$$U_{total} = \frac{1}{24}\int_0^L \int_0^w \left[\frac{1}{s_{11}^E s_{11}^m} Dk^2 + 24\left(\varepsilon_{11}^T \frac{1}{s_{11}^E} d_{31}^2\right) E_3^2 t_p\right] dxdz; \qquad (12)$$

where $D = 2s_{11}^m\left(3t_m^2 t_p + 6t_m t_p^2 + 4t_p^3\right) + s_{11}^E t_m^3$, t_p and t_m denotes the thickness of the piezoelectric layer and the middle layer, respectively.

Electromechanical coupling factor k_{31}^2must be considered during the flexure cycle of a piezoelectric actuator. The electromechanical coupling factor is defined by the ratio of the exchange of electrical and mechanical energy, which is yielded by:

$$k_{31}^2 = d_{31}^2 / \varepsilon_{33}^T s_{11}^E. \qquad (13)$$

The applied electric field E_3 across the bimorph bender is proportional to electric voltage *V* that is applied across the bottom and top electrodes. The relationship between the applied electric field and electric voltage is given by $E_3 = V/2t_p$. The applied electric voltage between the top surface and the lower surface of the bimorph bender results in the generation of electric charge – *Q*. This defines the capacitance of a free triple layer bender. Equations (14) and (15) show the capacitance of the free bimorph bender connected in series and in parallel, respectively.

$$C_{free} = \frac{Lw}{2t_p}\varepsilon_{33}^T\left(1 - \frac{D - 6s_{11}^m t_p\left(t_m + t_p\right)^2}{D} k_{31}^2\right). \qquad (14)$$

$$C_{free} = \frac{2Lw}{t_p}\varepsilon_{33}^T\left(1 - \frac{D - 6s_{11}^m t_p\left(t_m + t_p\right)^2}{D} k_{31}^2\right) \qquad (15)$$

The constitutive equation for a triple-layer piezoelectric bender involving extensive parameters, such as applied electric voltage *V*, external tip force *F*, external moment *M$_o$*, and uniform load *p*, as well as internal parameters such as angular deflection α, tip deflection δ, volume displacement *v*, and electric charge *Q*, can be characterized in the 4 x 4 matrix form. The constitutive matrix in [66] of the parallel piezoelectric bimorph bender is depicted as Equation (16), described on the following page.

$$\begin{bmatrix} \alpha \\ \delta \\ v \\ Q \end{bmatrix} = \begin{bmatrix} \frac{12 s_{11}^{m} s_{11}^{E} L}{Dw} & \frac{6 s_{11}^{m} s_{11}^{E} L^{2}}{Dw} & \frac{2 s_{11}^{m} s_{11}^{E} L^{3}}{D} & \frac{12 L s_{11}^{m} d_{31}\left(t_m + t_p\right)}{D} \\ \frac{6 s_{11}^{m} s_{11}^{E} L^{2}}{Dw} & \frac{4 s_{11}^{m} s_{11}^{E} L^{3}}{Dw} & \frac{3 s_{11}^{m} s_{11}^{E} L^{4}}{2D} & \frac{6 L^{2} s_{33}^{m} d_{31}\left(t_m + t_p\right)}{D} \\ \frac{2 s_{11}^{m} s_{11}^{E} L^{3}}{D} & \frac{3 s_{11}^{m} s_{11}^{E} L^{4}}{2D} & \frac{3 w s_{11}^{m} s_{11}^{E} L^{5}}{5D} & \frac{2 w L^{3} s_{11}^{m} d_{31}\left(t_m + t_p\right)}{D} \\ \frac{12 s_{11}^{m} d_{31}\left(t_m + t_p\right) L}{D} & \frac{6 s_{11}^{m} d_{31}\left(t_m + t_p\right) L^{2}}{D} & \frac{2 w s_{11}^{m} d_{31}\left(t_m + t_p\right) L^{3}}{D} & \frac{2Lw}{t_p} \varepsilon_{33}^{T} \left(1 - \frac{D - 6 s_{11}^{m} t_p \left(t_m + t_p\right)^{2}}{D} k_{31}^{2}\right) \end{bmatrix} \begin{bmatrix} M \\ F \\ p \\ V \end{bmatrix} . \qquad (16)$$

The terms considered in Equation (16) are as follows:

$$\frac{t_{p1}}{s_{11}^{p1}} + \frac{t_m}{s_{11}^{m}} + \frac{t_{p2}}{s_{11}^{p2}} = A\ ; \qquad (17)$$

$$\frac{t_{p1}}{s_{11}^{p1}}\left(3t_m^2 + 6t_m\left(t_{p1} - 2\vec{z}\right) + 4\left(t_{p1}^2 - 3t_{p1}\vec{z} + 3\vec{z}^2\right)\right) + \frac{t_m}{s_{11}^{m}}\left(t_m^2 + 12\vec{z}^2\right) + \frac{t_{p2}}{s_{11}^{p2}}\left(3t_m^2 + 6t_m\left(t_{p2} + 2\vec{z}\right) + 4\left(t_{p2}^2 + 3t_{p2}\vec{z} + 3\vec{z}^2\right)\right) = B\ ; \qquad (18)$$

$$t_{p1} + t_m - 2\overrightarrow{z} = H_1 \quad ; \qquad (19)$$

$$t_{p2} + t_m + 2\vec{z} = H_2; \qquad (20)$$

$$\frac{1}{2}\frac{\frac{t_{p1}}{s_{11}^{p1}}(t_{p1}+t_m)-\frac{t_{p2}}{s_{11}^{p2}}(t_{p2}+t_m)}{\frac{t_{p1}}{s_{11}^{p1}}+\frac{t_m}{s_{11}^{m}}+\frac{t_{p2}}{s_{11}^{p2}}} = \vec{z}\ . \tag{21}$$

Equation (16) expresses the dynamics of a bimorph bender by considering only one input voltage. In the case of empirical research, understanding of two input voltages, as provided in [67], [68], is required. The relevant enhanced matrix form of a piezoelectric bimorph bender is stipulated in Equation (22) as:

$$\begin{bmatrix} \alpha_y \\ \delta_y \\ v_y \\ \alpha_z \\ \delta_z \\ v_z \end{bmatrix} = \begin{bmatrix} \frac{12L}{Aw^3} & \frac{6L^2}{Aw^3} & \frac{2tL^3}{Aw^3} & 0 & 0 & 0 & -\frac{3d_{31_1}Lw^2}{2As_{11}^{p1}w^3} & \frac{3d_{31_2}Lw^2}{2As_{11}^{p2}w^3} \\ \frac{6L^2}{Aw^3} & \frac{4L^3}{Aw^3} & \frac{3tL^4}{2Aw^3} & 0 & 0 & 0 & -\frac{3d_{31_1}L^2w^2}{4As_{11}^{p1}w^3} & \frac{3d_{31_2}L^2w^2}{4As_{11}^{p2}w^3} \\ \frac{2tL^3}{Aw^3} & \frac{3tL^4}{2Aw^3} & \frac{3t^2L^5}{5Aw^3} & 0 & 0 & 0 & -\frac{d_{31_1}tL^3w^2}{4As_{11}^{p1}w^3} & \frac{d_{31_2}tL^3w^2}{4As_{11}^{p2}w^3} \\ 0 & 0 & 0 & \frac{12L}{Bw} & \frac{6L^2}{Bw} & \frac{2L^3}{B} & \frac{3d_{31_1}LH_1w}{Bs_{11}^{p1}w} & \frac{3d_{31_2}LH_2w}{Bs_{11}^{p2}w} \\ 0 & 0 & 0 & \frac{6L^2}{Bw} & \frac{4L^3}{Bw} & \frac{3L^4}{2B} & \frac{3d_{31_1}L^2H_1w}{2Bs_{11}^{p1}w} & \frac{3d_{31_2}L^2H_2w}{2Bs_{11}^{p2}w} \\ 0 & 0 & 0 & \frac{2L^3}{B} & \frac{3L^4}{2B} & \frac{3wL^5}{5B} & \frac{d_{31_1}L^3H_1w}{2Bs_{11}^{p1}} & \frac{d_{31_2}L^3H_2w}{2Bs_{11}^{p2}} \end{bmatrix} \begin{bmatrix} M_{oz} \\ F_y \\ p_y \\ M_{oy} \\ F_z \\ p_z \\ V_1 \\ V_2 \end{bmatrix} \tag{22}$$

2.2. Correlation of input voltages

The energy conservation model is unable to manifest the effects of an electrical load on the damping behavior. Therefore, the input voltage and electrical configuration is important when designing a piezoelectric actuator [69]. Ghosh and Jain [70] created a novel three-finger-based micro gripper from a piezoelectric bimorph, where precise handling is possible by tuning the voltage signal to the piezoelectric actuator. Shannon and Andrew [69] experimentally evaluated the electrical configuration required to achieve the optimal deflection; they provided conclusions on the significance of the input voltage for bimorph and multimorph piezoelectric benders. Evaluation was performed for biased unipolar, biased bi-polar, and bridged bi-polar electrical configurations. Shannon's results [69] confirmed the optimal deflection compared to the conventional electrical configuration. Thus, the input voltages required to actuate the piezoelectric layers with the respective phase shifts can be presented as follows:

$$V_1(t) = V_{1m}\, sin(\omega t) \tag{23}$$

$$V_2(t) = V_{2m}\, sin(\omega t \pm \Phi) \tag{24}$$

where, V_{1m}, V_{2m}, (ωt) and $(\omega t \pm \Phi)$ represents the voltage amplitudes and phase angles of voltage $V_1$and V_2, respectively. To investigate the contemporary aim of the research to attenuate vibration while using a piezoelectric composite beam, understanding of input voltage V_1 and V_2 alongside the corresponding phase shifts is vital. Substitution of Equations (23) and (24) for V_1 and V_2 in Equation (22) will provide deformation results related to the input voltages. Equations (23) and (24) will replace the parameters in Equation (22), thereby clarifying the model, which, in turn, can support empirical research.

2.3. Correlation of deflection of the beam and shunting of piezoelectric layers

In a piezoelectric mechanism, Young's modulus varies according to the electrical load, and the dielectric constant will differ based on mechanical pressure. Therefore, when the terminal of the piezo layer is electrically shunted or excited by using the input voltage, the mechanical stiffness of the material will decrease. Here, the efficiency of energy conversion from the electrical to the mechanical load can be evaluated by using electromechanical coupling factor k_{31}^2. The relationship between a change in stiffness of a piezoelectric material when the terminals are electrically shorted can be defined according to [71]:

$$Y_p(1 - k_{31}^2) = Y_{complex} \tag{25}$$

$$Y_p\left(1 - {d_{31}}^2/\varepsilon_{33}^T s_{11}^E\right) = Y_{complex}\ ; \tag{26}$$

where, Y_p – Young's modulus of a piezoelectric material for an open circuit, and $Y_{complex}$ – Young's modulus of a piezoelectric material's values for the shunt circuit.

Equations (25) and (26) affirm the change in stiffness of the active layers of the composite beam when their terminals are electrically shunted. However, for the initial interpretation of the composite structure's design that bolsters the conceptual mechanical design noted in Fig. 2.1 (a), it is essential to evaluate the frequency response function of the composite structure. Therefore, understanding the characteristics of solid damping is vital. Structural damping occurs due to internal energy dissipation within the material of the vibrating body, which changes alongside with the stiffness of the structure. Here, the frequency response function of the composite structure is dependent on the excitation voltage applied to the piezo layers.

For the current research, the frequency response function of a cantilever bimorph setup will be investigated by treating the cantilever configuration as a continuous beam model. For the continuous beam model, dimensional length L, width w, thickness t, mass m, density ρ, modulus of elasticity Y, and stiffness constant K are considered.

In the current investigation, empirical research was performed on the piezoelectric cantilever mechanism. The proposed idea, therefore, considered a cantilever setup by clamping one end of the beam by using a bench vice, and vertically suspending the opposite part, as shown in Fig. 2.4 (a). The equivalent single degree of freedom (SDOF) lumped parameter model of a bimorph bender is rendered in Fig. 2.4 (b).

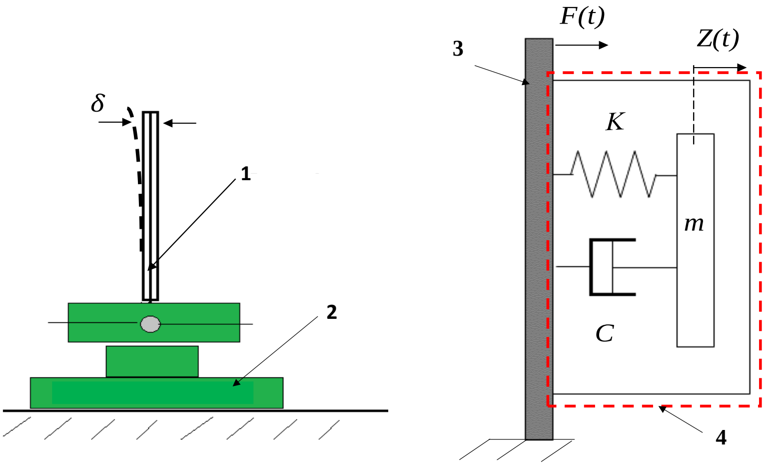

(a) (b)

Fig. 2.4 Cantilever setup: (a) bimorph bender clamped by using a bench vice: 1 – piezoelectric bimorph; 2 – vice to clamp the bimorph and (b) the setup’s equivalent SDOF lumped parameter model: 3 – piezoelectric layer – 1; 4 – elastic middle layer and piezoelectric layer – 2

One piezo layer was excited by the input voltage, resulting in the entire cantilever setup experiencing deflection δ and subsequent forced harmonic excitation $F(t)$. Considering the middle layer and the second piezo layer as one entity, the vibration transmitted to these two layers is given as $Z(t)$ (Fig. 2.4 (b)).

The complex stiffness term assisted in determining the deflection of the cantilever mechanism. Thus, the equation of motion for the entire cantilever structure Fig. 2.4 (b) is as follows [72]:

$$m\ddot{x} + K(1 + i\eta)x = Fe^{i\omega t}; \tag{27}$$

where, $K(1 + i\eta)$ is the complex stiffness term, and η is the dimensionless solid damping factor.

In a continuous beam model, beam stiffness can be defined by the elastic modulus, together with the second-moment area and the beam length. Thus, the complex elastic modulus can be expressed as:

$$Y_{complex1} = Y(1 + i\eta)\ ; \tag{28}$$

where, Y is a combination of Young's modulus for two piezo layers and the passive elastic layer.

To highlight the convenience of modelling, a relation between solid damping factor η and viscous damping ratio ζ was considered, which is expressed as [72]:

$$\zeta = \frac{\eta}{2} \tag{29}$$

Accordingly, the frequency response function at the cantilever beam's free end can be written as [72]:

$$\frac{Z_1}{F_1} = \frac{\sin\lambda L\ \ \cosh\lambda L - \cos\lambda L \sinh\lambda L}{\lambda^3 Y(1+i\eta)I(1+\cos\lambda L\ \ \cosh\lambda L)}; \tag{30}$$

where, $I = \frac{wt^3}{12}$ is the second-moment area, and $\lambda = \sqrt[4]{\frac{\rho A}{E_s I}}$ is the converting factor for the time dependence to the frequency.

2.4 Experimental setup

As mentioned at the beginning this section, the objective of this chapter will be to investigate the characteristics of the input voltage to study the response of a piezoelectric bimorph and then to investigate the research aim, to attenuate micro-vibration by shifting the resonance characteristic of a transitional structure. Therefore, two experimental analyses shall be conducted.

The first experiment, i.e., experimental setup – 1, investigates the characteristics of the input voltage and the respective response of a piezoelectric bimorph. For this, a custom-made bimorph without a passive layer will be considered. This experiment also gives insight into the construction of a bimorph for future implementation of the research results.

The second experiment, i.e., experimental setup – 2, empirically investigates the proposed aim of the current research by considering a cantilever setup comprising of an industrial grade piezoelectric bimorph. Compared to a customized bimorph, an industrial grade piezo provides a better construction with a passive layer sandwiched between two active layers. This helps to study the nature of the response of a cantilever bimorph subjected to external vibrations as well as to evaluate the attenuation of vibration possible by the combination of direct shunting between the active layers and the passive layers of the bimorph.

The experiments were carried out on an optical table so that to avoid external vibration influences on the test setup.

2.4.1 Experimental setup – 1: investigation of characteristics of input voltage and response of cantilever bimorph

For experimental setup – 1, a custom-made bimorph bender consisting of two piezoelectric layers was examined. The piezoelectric material used here was lead zirconate titanate (PZT), and the model is PZT-4 (SM121) plates. This setup is intended to study the response of a cantilever type PZT bimorph bender with respect to the input voltage with phase shifts, where each piezo layer exhibits the same polarization direction.

In order to achieve a custom-made bimorph bender, the proper bonding of layers by using adhesives is mandatory [73], but the process is complicated when three layers are involved. Therefore, bonding of two active layers while neglecting the passive layer is considered, and the piezo ceramics were bonded together by using *Loctite Super Glue*. This sample will be checked to evaluate the characteristics of the input voltages into Piezo layers and vibration attenuation.

Based on the availability of PZT ceramics, the dimensions of the PZT bimorph were: width – 10 mm, thickness – 2 mm, and the total length – 60 mm. One end of the bender was suspended freely by clamping the opposite end by using a fixed vice. The clamping extent was 5 mm, and the suspended part was 55 mm long. The vice is fixed on an optical table for stability and in order to avoid external vibration influences.

The schematic of experimental setup – 1 is shown in Fig. 2.5, and the actual experimental setup is shown in Fig. 2.6. Each PZT layer was excited by using a wave generator (DG1032) and two separate amplifiers (EPA104). The amplitude of vibration on the bimorph cantilever setup was analyzed by using an optical sensor (OFV-505) connected to a vibrometer-controller (OFV-5000) and a PicoScope to collect data.

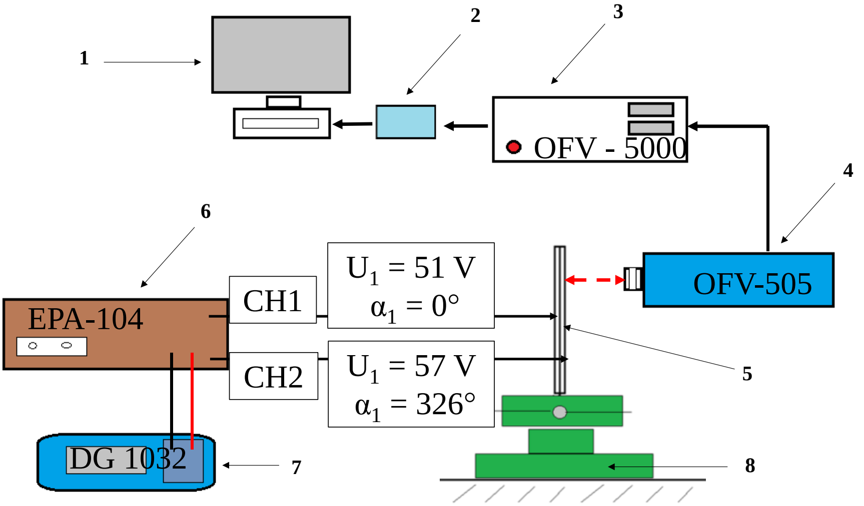

Fig. 2.5 Schematics of experimental setup – 1: scheme of experimental setup – 1: 1 – computer; 2 – PicoScope; 3 – vibrometer controller OFV-5000; 4 – optical sensor OFV-505; 5 – bimorph; 6 – amplifier EPA – 104; 7 – wave generator DG1032.; 8 – vice

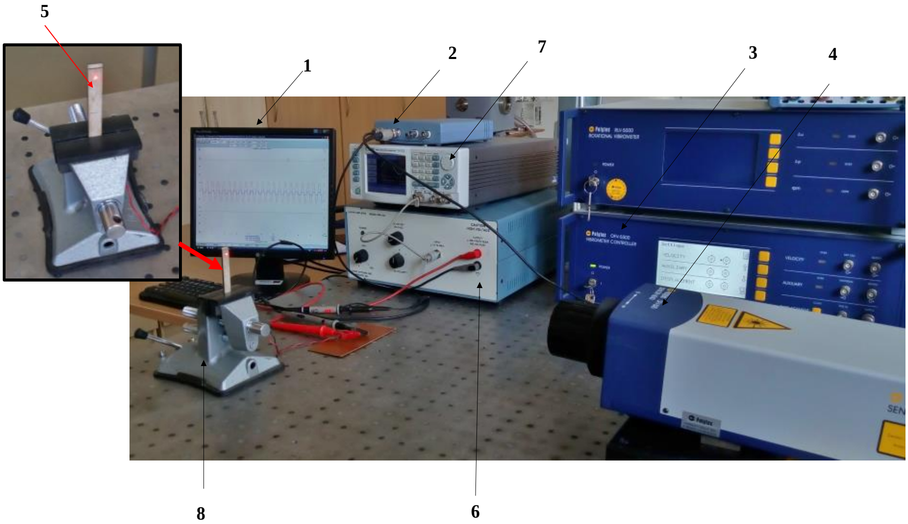

Fig. 2.6 Experimental setup – 1: 1 – computer; 2 – PicoScope; 3 – vibrometer controller OFV-5000; 4 – optical sensor OFV-505; 5 – bimorph; 6 – amplifier EPA – 104; 7 – wave generator DG1032.; 8 – vice

2.4.2 Experimental setup – 2: attenuation of vibration by controlling the resonance of cantilever bimorph setup

The objective of this setup was to study the response of a cantilever PZT bimorph bender subjected to flutter from an external source, and to investigate the possible vibration attenuation by changing the resonance characteristics of the same setup achieved through the direct shunting of active (PZT) and passive layers (a copper shim).

In order to analyze the objective of experimental setup – 2, it is mandatory that the sample is provided with a passive layer for shunting. Therefore, an industrialized parallel bimorph bender, Type – 1, from industrial *Johnson Matthey* [74] was considered. The dimension of the Type – 1 bender is the closest dimensions available, which is similar to sample from experimental setup – 1. Type – 1 bimorph bender is comprised of a thin copper shim sandwiched between two PZTs. The copper shim acted as a ground and provided flexural strength to the entire bimorph.

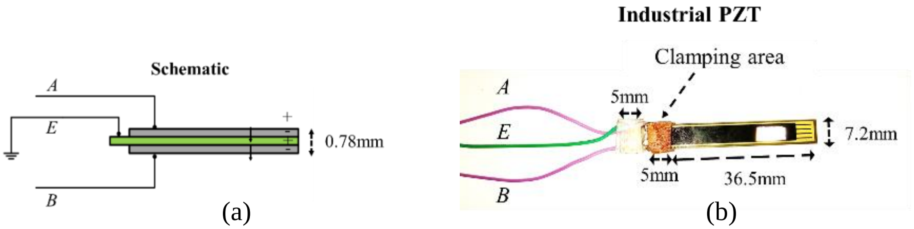

(a) (b)

Fig. 2.7 PZT bimorph bender: (a) schematics and connection of terminals to respective passive and active layers; actual sample used for experimental setup – 2

Figure 2.7 (a) illustrates the schematics and connection of a PZT bimorph bender, where, terminals *A*, *B* are attached to the upper and the lower PZT layer, respectively, and terminal *E* is connected to the middle copper shim. Figure 2.7 (b) shows the sample used for experimental setup – 2, a Type – 1 industrialized PZT bimorph bender from *Johnson Matthey* [74]. The bimorph bender features a thickness of 0.78 mm, a width of 7.2 mm, and a total length of 40.5 mm. One end of the industrialized PZT bimorph bender was suspended horizontally by clamping the opposite end to a mechanical shaker. The clamping region was 5 mm, and the suspended part was 36.5 mm long (Fig. 2.7 (b)). The shaker was placed on an optical table to avoid the influence of external vibrations.

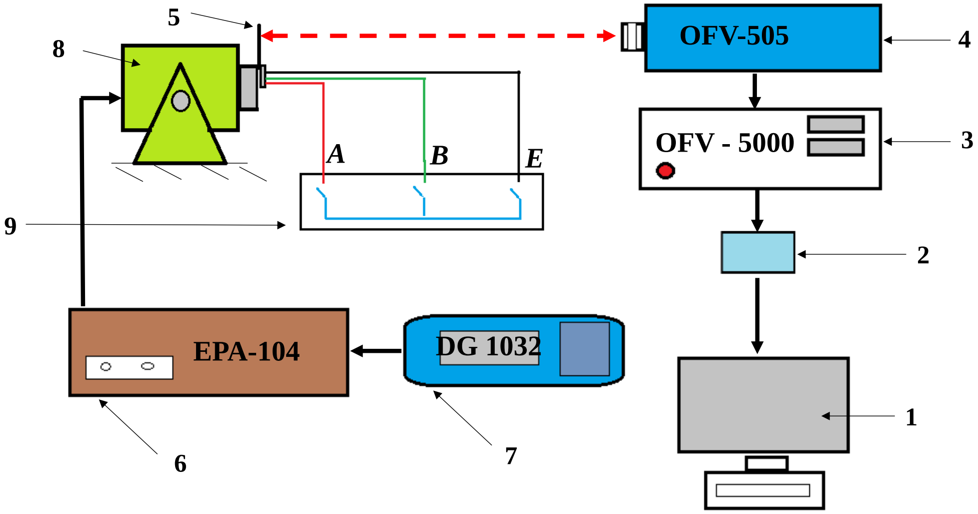

Fig. 2.8 Schematics of experimental setup – 2: scheme of experimental setup – 2: 1 – computer; 2 – PicoScope; 3 – vibrometer controller OFV-5000; 4 – optical sensor OFV-505; 5 – bimorph; 6 – amplifier EPA – 104; 7 – wave generator DG1032.; 8 – shaker; 9 – shorting board

Figure 2.8 illustrates the schematics of experimental setup – 2, and Fig. 2.9 shows the actual experimental setup – 2. Here, the shaker was excited with the help of a wave generator (DG1032) and an amplifier (EPA-104). The amplitude of vibration on the bimorph cantilever setup was analyzed by using an optical sensor (OFV-505) connected to a vibrometer-controller (OFV-5000), and to a PicoScope. A breadboard (a shorting board) was provided to shunt the terminals and to study a range of possible shunting combinations.

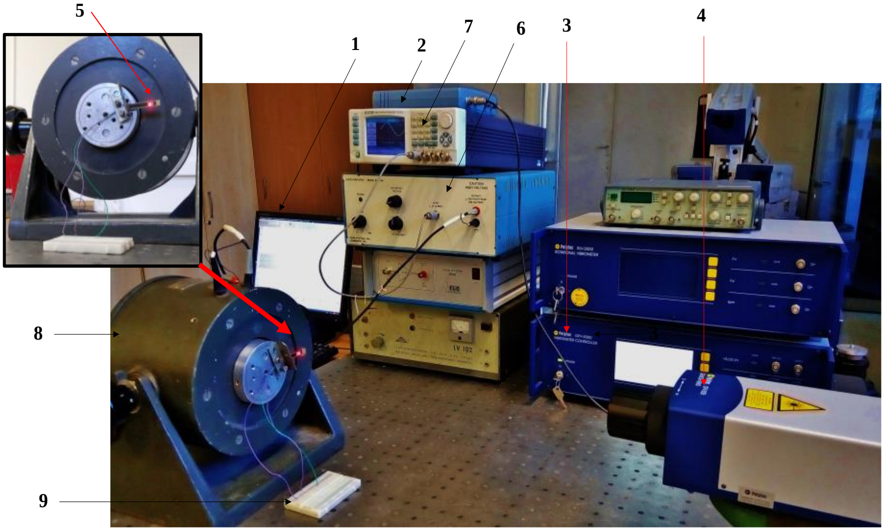

Fig. 2.9 Experimental setup – 2: 1 – computer; 2 – PicoScope; 3 – vibrometer controller OFV-5000; 4 – optical sensor OFV-505; 5 – bimorph; 6 – amplifier EPA – 104; 7 – wave generator DG1032.; 8 – shaker; 9 – shorting board

2.5 Results and discussion

The discussion about the results obtained for the investigation of the characteristics of the input voltage and the response of the cantilever bimorph (experimental setup – 1) and the attenuation of vibration by controlling the resonance of the cantilever bimorph setup (experimental setup – 2) is carried out in this section.

For experimental setup – 1, in order to achieve the maximum flutter in the cantilever setup, one of the PZT layers was actuated by the input voltage. The input voltage gains were varied by using the voltage amplifier. It was observed that for safe working of the sample without breaking apart the PZT crystal from the clamped area, the excitation closer to the second mode has to be considered. The second mode was obtained by initiating one of the PZT layers at 51 V, at a zero phase angle ($V_1 = \{51\,\mathrm{V};\ \Phi\ 0^\circ\}$). During the second mode of vibration, the maximum amplitude of oscillation at the antinode position was observed to be 4.68 μm at 2.61 kHz; this is illustrated in Fig. 2.10 (a).

Then, in order to alleviate the magnitude of vibration in the setup, the second layer was excited. The voltage close to V_1 was considered and tested. After fine tuning for the voltage and phase for the second layer, maximum possible attenuation was recorded when the voltage characteristic was 57 V, with a -326° phaseshift ($V_2 = \{57\,\mathrm{V};\ \Phi = -326^\circ\}$). The achieved result demonstrated 80% mitigation in the amplitude of oscillation, where the maximum magnitude of veer at the antinode position abated to 0.78 μm at 1.76 kHz (Fig. 2.10 (b)).

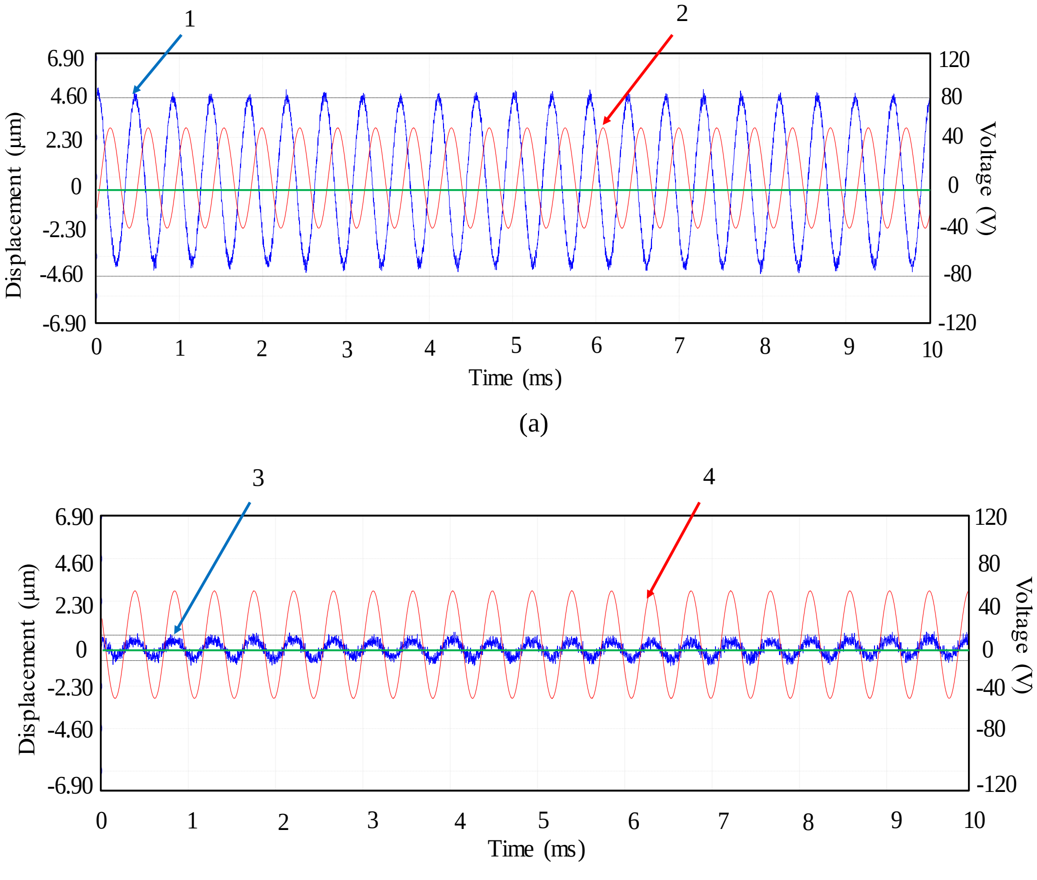

(a)

(b)

Fig. 2.10 Amplitude of flutter in the cantilever setup: (a) one piezo layer triggered: 1 – amplitude of vibration on the cantilever setup; 2 – input voltage for the first layer; (b) second layers exited with a phase shift: 3 – amplitude of vibration on the cantilever setup when the second layer is activated along with the first layer; 4 – input voltage for the second *t* layer

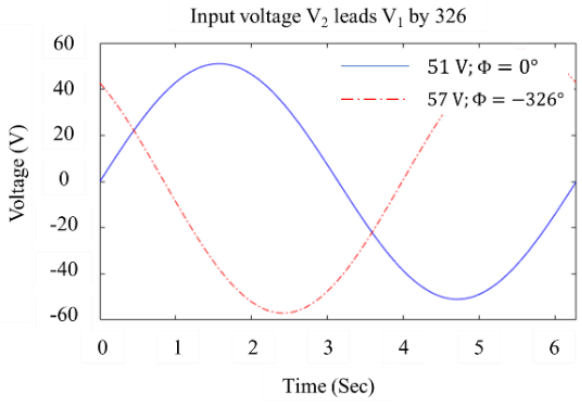

Fig. 2.11 Range of input voltages with phase shifts

The results of the experimental analysis were verified by using the speculative model. Figure 2.11 indicates the sine form of two input voltages and the phase difference between voltages V_1 and V_2. The frequency response function for the cantilever structure was plotted based on Equation (30) and is shown in Fig. 2.12. It is observed, based on the clamping mechanism, that the experimental values diverge.

The results of the experiment confirmed that in order to reduce the amplitude of flutter experienced by activating one piezo layer, the second layer has to be initiated by a voltage with a phase shift.

In real applications, the prerequisite phase shifts are obtained by tuning the piezo system while using the appropriate resonant circuit or voltage inverters. This mechanism is an analogous technique used for quiver amortization in skis, tennis rackets, and baseball bats, where, multiple PZT patches were used to achieve damping.

The current research is focused on a single composite structure composed of an elastic middle layer sandwiched between two PZT materials, as a means for attenuating vibration via the principle of changing the system resonance.

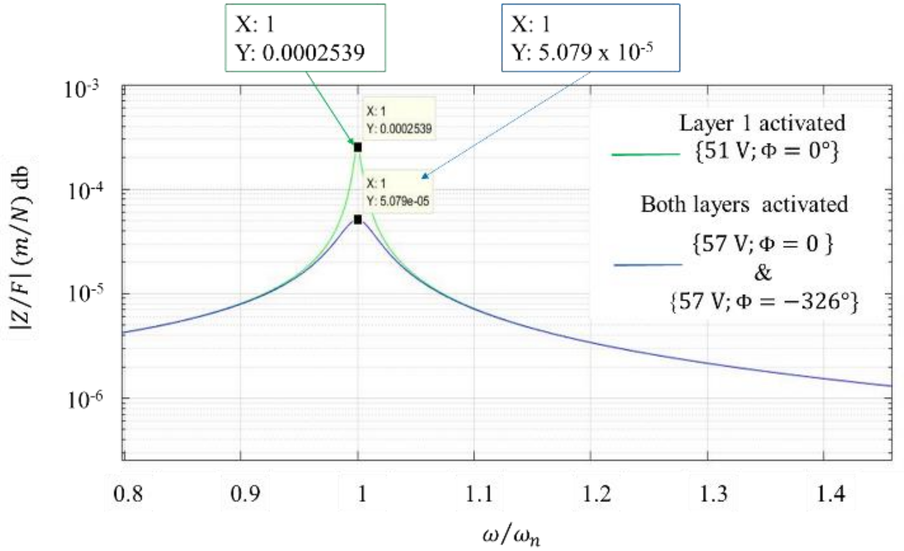

Fig. 2.12 Frequency response function of the cantilever structure

Steffen and Inman [75] clarified on the optimal design required for vibration attenuation in a mechanical system when several natural frequencies prevail in the frequency band of interest. The researchers explored active and passive vibration damping techniques while using PZT materials. Their research results indicate that the actuator gain becomes significant when more than one mode requires damping. They addressed this problem by covering a significant part of the structure's surface with the PZT element.

The outcome of experimental setup – 1 led to the knowledge that covering the entire structure (the two opposite sides of the frame) with PZT material, rather than positioning patches of PZT elements at nodes, achieved attenuation [4, 21, 22].

Based on the research results concluded from experimental setup – 1, and in order to investigate the response of the structure for unmediated shunting of the passive and active layer, an industrialized PZT bimorph was considered in experimental setup – 2. Here, the experiments will be performed at the first natural frequency of cantilever setup as the objective is to verify the possibility to attenuate micro-vibration on the structure by directly shunting the layers.

Initially, an impulse test was performed for the cantilever setup to analyze damping ratio δ, damping coefficient ς, and natural frequency f_n. The tests were executed for a shunt-free system, and also for the respective combinations involving the shunting of the passive and active layers. The impulse test result is shown in Table 2.1.

The obtained results show that the damping ratio, the damping coefficient values, and the natural frequency of the cantilever system varied between the shunted terminals. This empirical result supports the mechanism stated in Equations (6) and (7) that the mechanical stiffness of the material reduces when the active layers are electrically shunted.

Table 2.1 Impulse test results.

Terminal of connection	Damping ratio δ	Damping coefficient ς	Natural frequency f_n (Hz)
No terminal connected	0.181	0.0288	220
A + *B*	0.282	0.0398	221
A + *E*	0.123	0.0196	213.5
B + *E*	0.146	0.0233	213
A + *B* + *E*	0.1306	0.0208	208.5

From the table above it can be determined that the natural frequency of the cantilever bimorph setup for a shunt free system is close to 220 Hz. Therefore, the tests will be performed at frequencies between 190 Hz and 240 Hz, where the maximum flutter of the bimorph can be experienced.

The flutter experienced in the cantilever setup concerning different excitation frequencies, and for a possible combination of the shunting-circuit, are recorded and shown in Fig. 2.13 and Fig. 2.14. These results provide insight into the broadening of the resonance frequency spectrum of a structure, as it relates to the unmediated shunting combinations of the terminals. Thus, the results also highlight that the resonance frequency of the structure can be broadened without changing the mass and the length of the structure.

Figure 2.13 and Fig. 2.14 illustrate the possible resonance extremities of the cantilever PZT bimorph system when mechanically excited using a dynamic shaker at the systems' corresponding natural frequencies. Based on shunting combinations: *no terminal connected*, *A* + *B*, *A* + *E*, *B* + *E*, and *A* + *B* + *E*, the cantilever mechanism uncovered five different natural frequency values, indicated as F_n, F_{n1}, F_{n2}, F_{n3}, and F_{n4} in the plots shown in Fig. 2.13 and Fig. 2.14. The magnitude of flutter during each combination of shunts and at their respective natural frequencies also revealed discrete gains, such as 404 µm, 410 µm, 412 µm, 401 µm, and 397 µm.

Accordingly, Fig. 2.13 illustrates the notion that, when mechanically triggered, a composite beam analogous to a PZT bender can go through more than one resonance periphery corresponding to the discrete values of excitation.

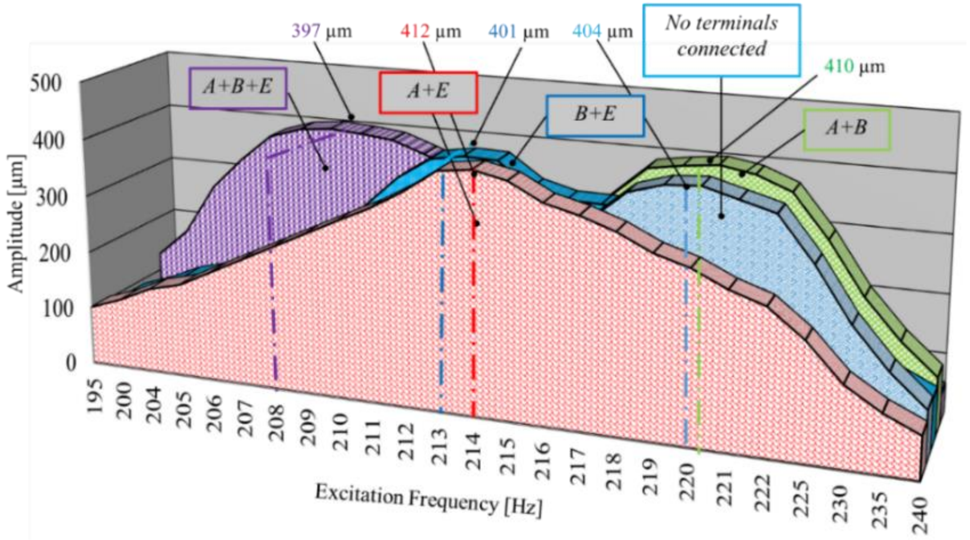

Fig. 2.13 The amplitude of flutter for the different excitation frequencies corresponding to the unmediated shunting combinations of terminals

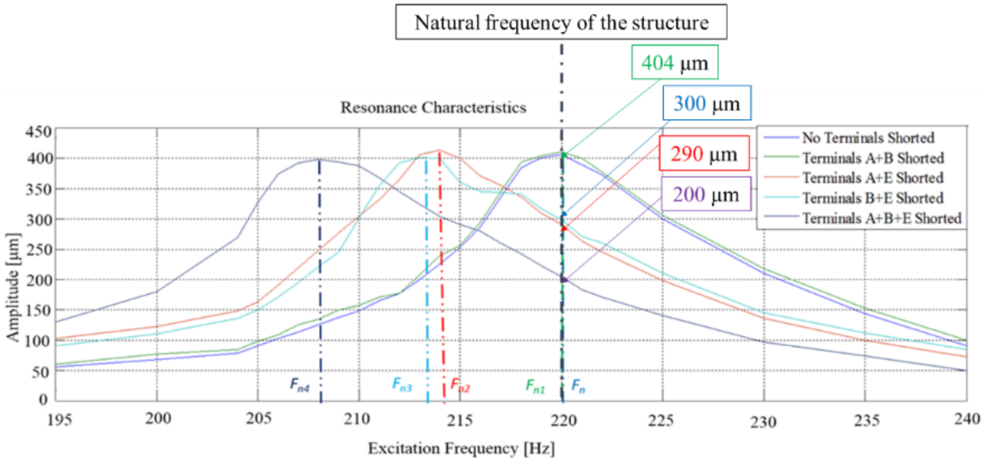

Fig. 2.14 Plot showing shudder attenuation by shifting the resonance extremity of a system

Additionally, the plot shown in Fig. 2.14 reveals that, when the PZT cantilever mechanism was triggered at a frequency of 220 Hz, the maximum experienced flutter was 404 µm for the shunt *no terminal connected* setup. When the system was subjected to shunting at an excitation frequency of 220 Hz, *A* + *B*, *A* + *E*, *B* + *E*, *A* +

$B + E$, and their corresponding discrete gains were logged as 405 µm, 290 µm, 300 µm, and 200 µm, respectively. Thus, the obtained results (peak values) highlight the possibility of attenuating the shudder experienced in a composite structure, similar to the PZT bimorph cantilever structure presented herein, by 50%.

The results of experimental setup – 2 clearly confirmed the proposed aim of the research for mitigating the quiver promulgating via a composite brace, effected via the unmediated shunting of the passive and active layers of the same composite structure.

The research results in the present study show that:

- the existing system does not exhibit sophisticated design or control [8], where the dependency of the mechanism could be problematic in the long run; and that
- the 50% mitigation in flutter achieved through unmediated shunting of the active and passive layers, where external shunt circuits are used for dissipation of energy, is not required.

2.6 Implementation of current research

The current understanding of attenuation of vibration using a PZT bimorph bender investigated in this research recalls the topic addressed in Section 2, Fig. 2.1 (a), that is, the conceptual mechanical design of four composite beams separating the active and the interface plate. By introducing more smart composite beams to the mechanism, the combinations for shunting will increase.

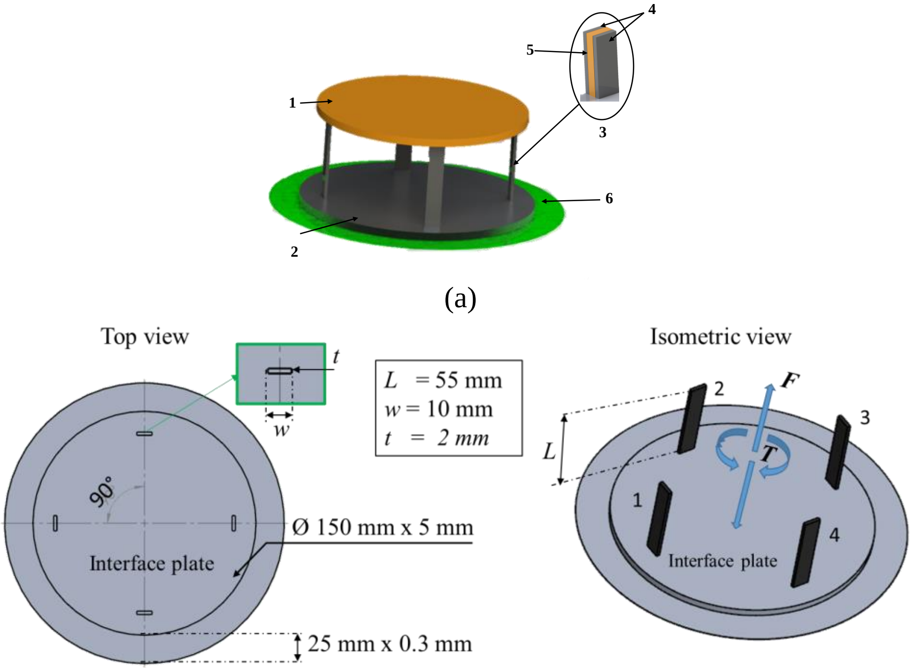

(a)

(b)

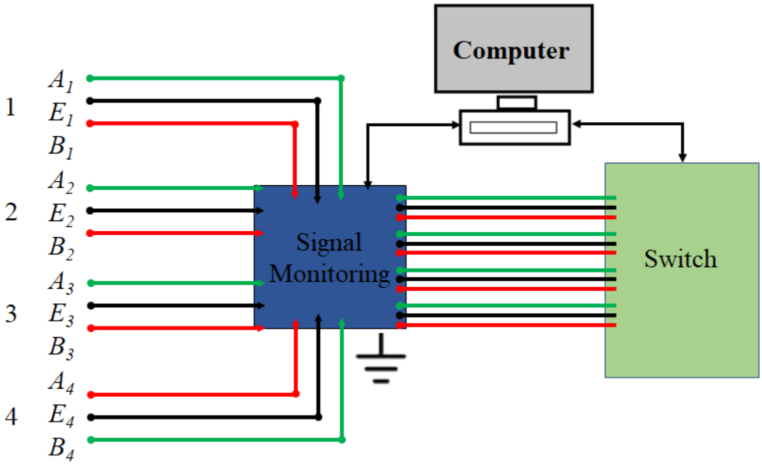

(c)

Fig. 2.15 Consideration for future research: (a) Considered conceptual mechanical design of beam-type structure that connects the active plate and the interface plate: 1 – active plate; 2 – interface plate; 3 – isolator; 4 – smart material; 5 – interconnecting structure; 6 – support area; (b) detailed mechanical design and (c) combination for direct shunting of piezo without additional shunt circuits and active monitoring

Thus, as a follow-up to the present research, we will engage in detailed investigation of the conceptual mechanical design (Fig. 2.15 (a) and (b)) by considering the orientation of a transitional composite structure, and by pursuing answers to the ambiguous (unclear) response of the system as it relates to quiver in axial and lateral spaces. The future research will also include control for shunted piezoelectric dampers through various types of electrical or electronic circuits, but the main objective will still be to investigate the combination of direct shunting of piezo without additional shunt circuits and through active monitoring, see Fig. 2.15 (c).

2.7 Conclusions of the section

In this chapter, theoretical and experimental investigation to attenuate micro-vibration propagating through a transitional structure is investigated by considering a PZT bimorph bender:

The following points are concluded from the current research:

1. A conceptual mechanical design based on problem analysis of four beams separating an active plate and an interface plate is considered as an example for research applications. Here, the primary intent of the current investigation is to mitigate the shudder propagating through the transitional structure, where the transitional structure is considered to be a composite structure. Therefore, a cantilever setup from a piezoelectric bimorph (or trimorph) bender was considered for further investigation.

2. A currently existing constitutive equation for evaluating a set of extensive and internal parameters of bimorph benders is derived (by using the energy conservation model) and expressed in the 4x4 matrix format. In this research, the currently available constitutive equation is modified by considering the effect of two input voltages with phase shifts and the correlation of the deflection of the bimorph bender to the stiffness parameter, by treating the beam as a continuous beam model. The theoretical model described in this research can be used to model any piezoelectric bimorph beam that comprises a passive layer sandwiched between two active layers with known polarization segments.
3. Experimental setup – 1, out of the two considered experimental setups, focused on the nature of the input voltage and the phase shift required to attenuate the flutter in the cantilever structure. The outcome of experimental setup – 1 supported the underlying working principle of experimental setup – 2.
4. Experimental setup – 2 empirically interpreted the proposed research aim for mitigating the shudder propagating through a transitional composite structure. This was achieved by evaluating the combination of unmediated shunting of the passive and the active layers.
5. 50% alleviation in flutter was obtained with a single composite beam and without external shunt circuits.

3. THEORETICAL ANALYSIS AND MODELLING TO ATTENUATE MICRO-VIBRATION BY CONTROLLED FRICTION

For the current research, the control of the normal force acting between two steel plates, while using an external magnetic field, is investigated. Here, in order to introduce the magnetic flux through steel plates, the principle of magnetic latching is used. For this research, we shall consider the coefficient of friction as μ and magnetic permeability as μ.

Latching is a process to provide a force of attraction between two surfaces. The latching application can be categorized as contact and non-contact (a.k.a. contactless) [76]. In contact latching, the magnet is attracted to another member which can be a magnet or soft magnetic material, such as iron. Here, the magnetic material is placed in direct contact with the magnet. In non-contact latching, the magnet and the members are separated by a gap, and the magnet must project its field across the gap so that to exert a force of attraction (Fig. 3.1). The poles of the magnet must be minimally separated so that the field will span the gap. The magnetic force of attraction between the magnet and the plates can be explained by using magnetic circuit analysis [76]. There are numerous latching circuits, and most of them can be designed and optimized by using the magnetic circuit theory [76].

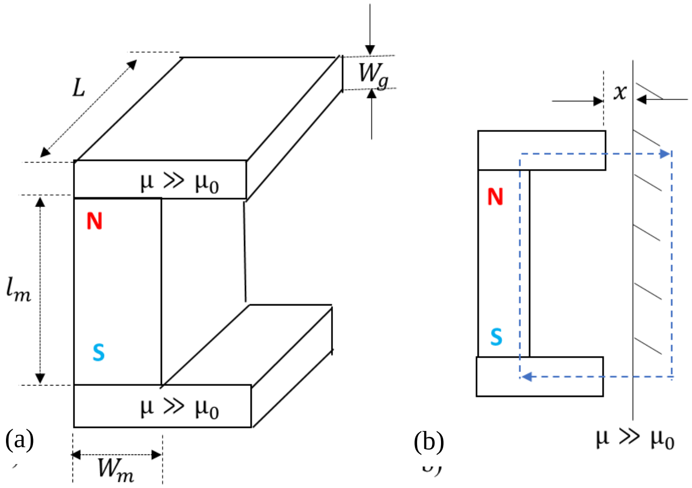

Fig. 3.1 Noncontact latching: (a) magnet with two attached flux plates; (b) latching circuit [76]

For the current research, we shall be considering an arrangement as shown in Fig. 3.1 (a), and the magnetic circuit of the given model is as shown in Fig. 3.1 (b) [76]. Here, the magnet with attached flux plates is attracted to a wall made of a soft magnetic material, where there exists gap *x* between the magnetic structure and the wall, and $x > 0$. The permeability of the structure and the wall considered to be as infinite permeability. Also, the magnetization of the magnet is a linear second quadrant demagnetization curve [42–44] of the form: $B_m = B_r + \mu_m H_m$ and $\mu_m =$

$\frac{B_r}{H_c}$; where, B_r is the remanence of the magnet, H_c is coercivity and μ_m is permeability of magnet. From Fig. 3.1 (a), L and W_g are the length and the width of the flux plate, respectively. Whereas, l_m and w_m are the length and the width of the magnet in use. By using the magnetic circuit theory [76], the force between the magnetic setup and the wall, at distance x, is [76]:

$$\mathrm{F}\,(\mathrm{x}) = \frac{B_r^2 A_m^2}{\mu_0 A_g \left(1+2(\mu_m/\mu_0)(A_m/A_g)(x/l_m)\right)^2}\hat{n}; \tag{31}$$

where, $A_m = L\ w_m$ is the area of the magnet, and $A_g = L\ w_g$ is the area of the gap. Here, the outward normal $\hat{\boldsymbol{n}}$ of the wall points towards the magnet, and, therefore, the force is attractive.

The force of attraction between two magnetized surfaces can also be explained by using Gilbert Modelling [79]. The equation is valid only for cases in which the effect of fringing is negligible, and the volume of the air gap is much smaller than that of the magnetized material [79]:

$$\mathrm{F} = \frac{\mu_0 H^2 A}{2} = \frac{B^2 A}{2\mu_0}\ ; \tag{32}$$

where, A is the area of each surface in m^2, H is their magnetizing field in A/m, the permeability of space is $\mu_0 = 4\pi \times 10^{-7}\,\frac{\mathrm{H}}{\mathrm{m}}$ and B is the flux density in Tesla, at the area of contact between the two surfaces.

3.1 Theoretical analysis for controlling the stiffness by using friction

A method to control frictional damping by controlling the normal force between two surfaces is investigated in this section. Two different theoretical test setup models are considered and analyzed for this investigation.

Also, for the theoretical modelling, the following parameters are considered:

a. two highly permeable surfaces sliding along each other without any stick-slip;
b. supporting an ambient environment;
c. maintaining plane-to-plane parallel contact;
d. the contact between the surfaces is kept dry and clean;
e. for modelling, we disregard/oversee the Van der Waals force and any internal deformation taking place, and
f. we consider three significant laws for friction [35–37] as:
    i. the frictional force is proportional to the normal force,
    ii. the frictional force is independent of the apparent contact area, and
    iii. the frictional force is independent of the sliding speed.

3.1.1 Investigation of the influence of magnetic field for a steel plate to freely slide over a steel platform, at given inclination

For the first theoretical analysis, a free body diagram is considered, where a steel plate is placed parallel to a steel platform, which is at an inclination θ, as shown in Fig. 3.2. The dimension of the steel plate is 130 mm x 50 mm x 10 mm; therefore, it possesses a weight of 5 N. Here, the design parameters were considered based on the possibility to build a real system for the test.

Table 3.1 shows the characteristics of steel C10 for the plate and the steel platform.

Table 3.1 Characteristics of steel C10 [80]

Material	Coefficient of friction (Dry contact)		Density of mild steel (*g/cm*^{3})
	Static (μ_s)	Sliding (μ_k)	
Steel C10	0.74	0.57	7.85

The frictional force between steel plates is equal to the effect of gravitational pull, as the steel plate starts sliding over the steel platform. That is, $f = F$, where

$$\mu_s mg \cos\theta = mg \sin\theta; \tag{33}$$

$$\tan\theta = \mu_s \tag{34}$$

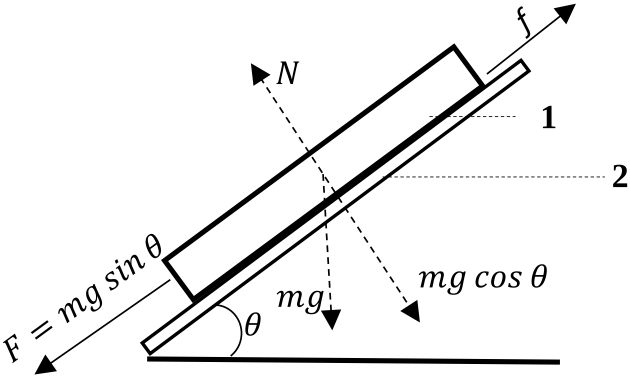

Fig. 3.2 Free body diagram: 1 – steel plate (130 mm x 50mm x 10 mm); 2 – steel platform (200 mm x 150mm x 10 mm)

Equation (33) determines that the steel plate starts sliding from the steel platform in the direction of gravitational pull at an inclination 36.50°. Even if the mass of the steel plate varies, the minimum inclination required for the steel plate to slide is 36.50°. When the plate starts to slip, then, the magnitude of the gravitational pull is equal to the frictional force of 2.97 N.

As the force of attraction between the steel plates increases, the frictional force also increases. For the current research, the attraction force between the steel plates is controlled by using a varying magnetic field. Therefore, a model (Design-1), Fig. 3.3, is set up in order to verify the proposed idea. Here, a neodymium magnet provides the required magnetic flux to bring the force of attraction between the two steel plates. The 35-grade neodymium magnet of dimensions 50 x 50 x 10 mm, with the magnetization direction along 10 mm, is used for Design – 1.

Here, the model is designed by using a linear second quadrant demagnetization curve of the form: $B_m = B_r + \mu_m H_m$, for the magnetization of the magnet, where $\mu_m = \frac{B_r}{H_c}$ and $B_r = 1.17$ T, and $H_c = 859000$ A/m.

For the current research, *FEMM 4.2* software is considered to model Design –1 (Fig. 3.3) and to perform a numerical simulation of the varying magnitude of flux density through the steel plates. The received results from *FEMM 4.2* are shown in Fig. 3.4, whereas Fig. 3.5 illustrates the flux density through the steel platform. Figure 3.6 shows the flux density at the area of contact between the steel platform and the steel plate. Here, the average of the flux density at the contact area was found to equal 0.01 T.

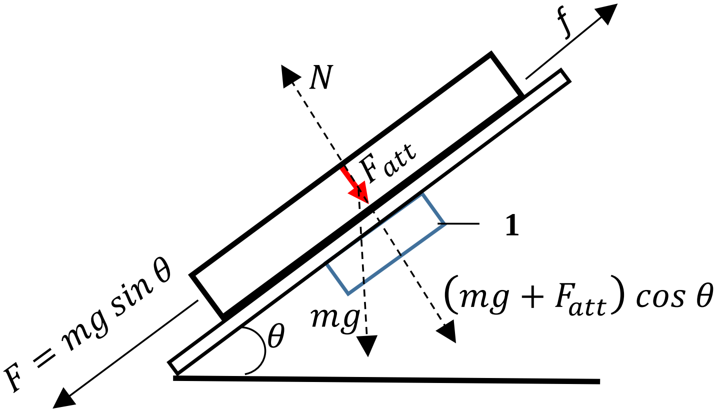

Fig. 3.3 Design – 1: to investigate the influence of the magnetic field on a steal plate to freely slide over a steel platform, at a given inclination: 1 – neodymium magnet (50 mm x 50 mm x 10 mm)

From Equations (31) and (32), the force of attraction between the plates can be obtained as **F** = 0.26 N.

With the presence of the magnetic latching, the equation for static friction gets modified as:

$$|f| = \mu\left((W + F)\cos\theta\right) \tag{35}$$

The magnitude of frictional force (Equation (35)) acting between the steel plates with magnetic flux passing through steel plates was obtained as $|f| = 3.128$ N.

Here, the mass of the steel plate is not affected by magnetizing the surfaces. Therefore, the rate of the gravitational pull of 2.97 N, acting on the steel plate, remains the same. Since the frictional force f = 3.128 N is higher than the gravitational pull F = 2.97 N, the steel plate maintains its position to the steel platform at an inclination 36.50°, and the improved angle at which the plate starts to slide becomes 38.74°.

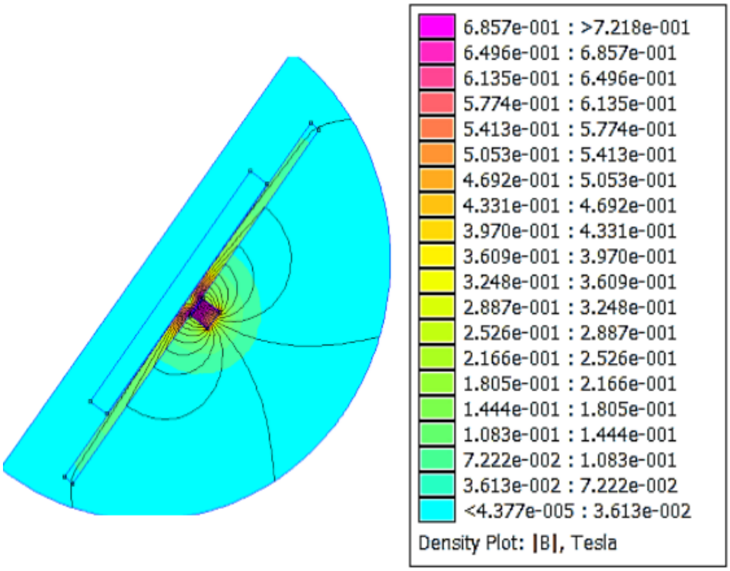

Fig. 3.4 *FEMM* results for Design – 1

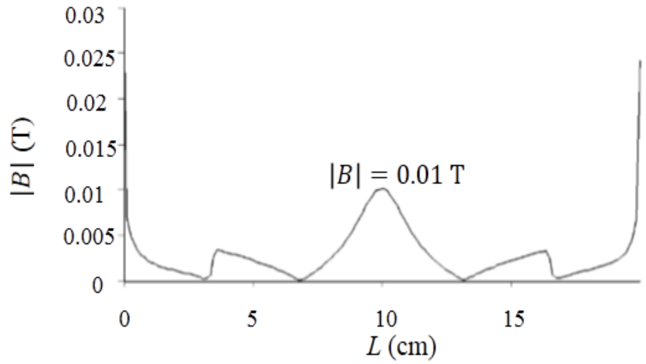

Fig. 3.5 Magnitude of the flux density passing by the steel platform in Design – 1

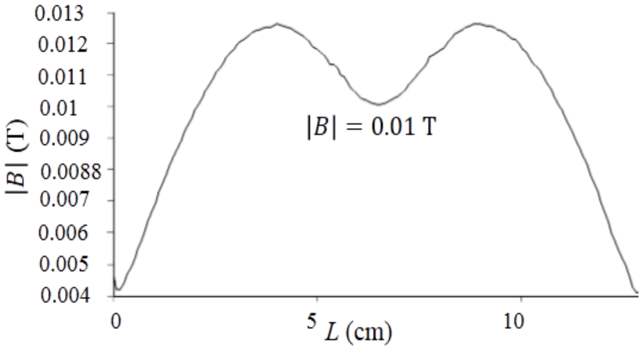

Fig. 3.6 Magnitude of the flux density at the area of contact between the sliding plate and the platform for Design – 1

3.1.2 Enhancement of the magnetic flux passing through steel plates

In Design – 1, the magnetic flux through the steel platform to the steel plate is 0.01 T, which results in a low magnitude of the attractive force between the steel plates. The small scale of the attractive force between the steel plates is improved by considering Design – 2.

In Design – 2, the magnetic field through the plates is amplified, by considering the magnetic circuit. The magnetic circuit helps to complete a path that allows the magnetic field to flow through the steel plates from the north pole to the south pole of the magnet. Here, it is significant to separate the poles of the magnet effectively for the field to span the gap [76].

Design – 2 consists of a table-type model with two legs, see Fig. 3.7. The leg consists of two steel plates, sections 1 and 2. The body of the table is a neodymium magnet which connects the two steel plates. Here, a 35 grade neodymium magnet of dimensions 50 mm x 10 mm x 30 mm, with the magnetization direction along 30 mm considered for Design – 2 modelling and simulation.

Figure 3.8 illustrates the free-body diagram for Design – 2, where, section – 1 is subjected to load W_1, and section – 2 takes in the total weight of the table, W_{total}. In reality, the weight distribution depends on the change in the inclination of the platform [81–83]. Therefore, the load on section – 1 is the sum of the weight of section – 1 itself, the attached magnet, and section – 2. Here, the weight of section – 1 and section – 2 is 1.923 N each, and the magnet weighs 1.0731 N. Therefore, the total weight of Design – 2 is $W_{total} = 4.9191$ N.

For Design – 2, the minimum inclination θ required for the setup to slide over the steel platform is 45.83°.

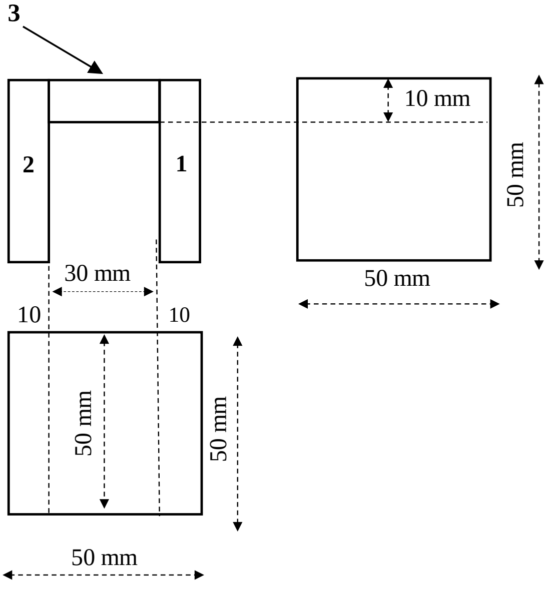

Fig. 3.7 Model and dimensions of the moving surface: 1, 2 – mild steel (50 x 50 x 10); 3 – neodymium magnet (50 x 10 x 30)

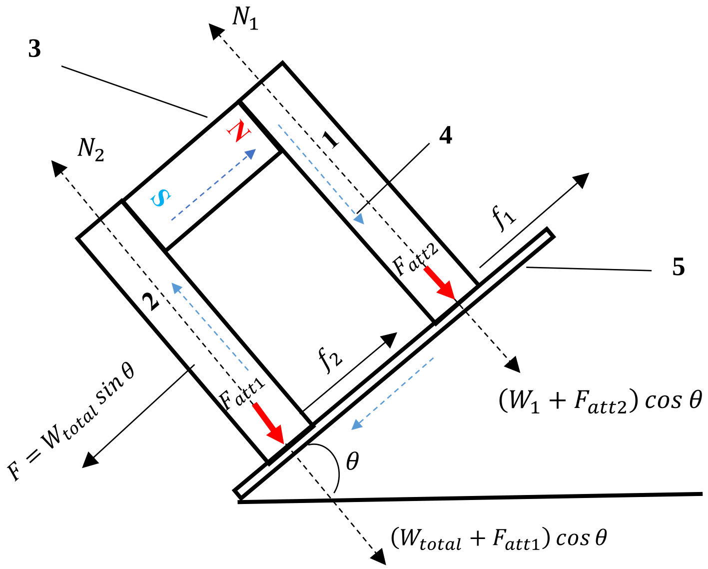

Fig. 3.8 Design – 2: Model and dimensions of the moving surface: 1, 2 – mild steel (50mm x 50mm x 10mm); 3 – neodymium magnet (50mm x 10mm x 30mm); 4 – direction of magnetic field lines; 5 – steel platform (200mm x 150mm x 5mm)

The magnitude of frictional force f_1 at the area of contact (Fig. 3.8) for an inclination 45.83° and without considering the flow of the magnetic field through the plates is determined by:

$$\mu_s W_1 cos\ \theta\ = 0.992\ \text{N}$$

The magnitude of frictional force f_2 at the area of contact for an inclination of 45.83° and without considering the flow of the magnetic field through the plates is:

$$\mu_s W_{total}\ cos\ \theta\ = 2.536\ \text{N}$$

Therefore, the total magnitude of the frictional force is: $f_1\ +\ f_2$ = 3.528 N.

At an inclination of 45.83°, the gravitational pull on the stand equals:

$$F\ = W_{total}\ sin\ \theta\ = 3.528\ \text{N}$$

As the frictional force and the gravitational pull are 3.528 N each at an inclination of 45.83° without the magnetic field passing through the model, therefore, the model slides over the platform. The minimum slope required for the device to slip is 45.83°.

The magnitude of flux density passing through the steel plate is investigated (Fig. 3.9) by considering that there is a magnetic flux flow in the model, which completes the magnetic circuit. This is modelled by using *FEMM* simulation.

Figure 3.10 illustrates the magnitude of the flux density through section – 2 and section – 1. Whereas, Fig. 3.11 shows the rate of the flux density through the platform plate at the area of contact with the two sections.

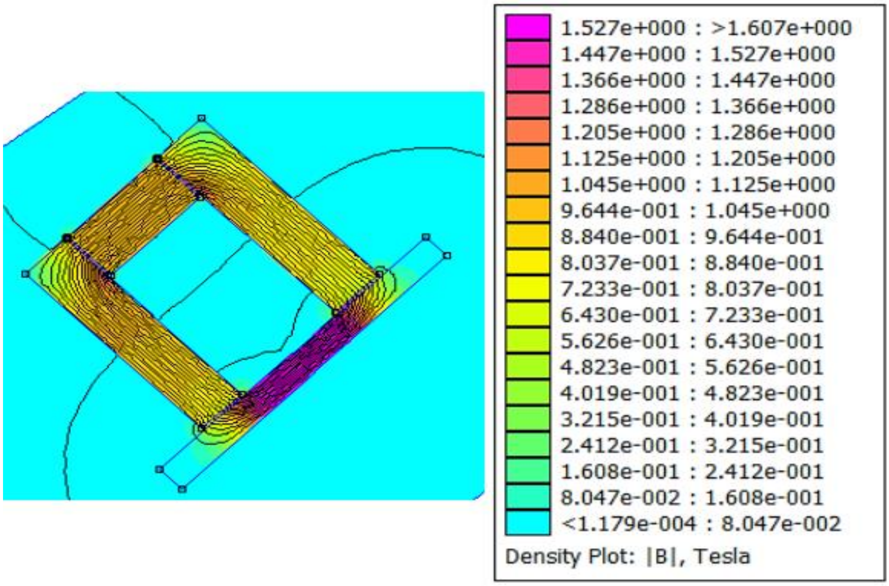

Fig. 3.9 Simulation results of second theoretical analysis using Design – 2

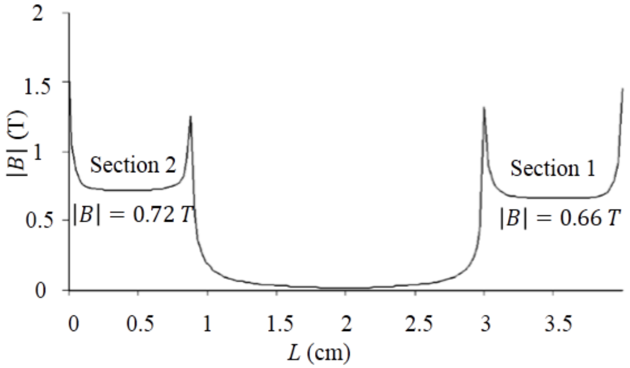

Fig. 3.10 Flux density experienced at the area of contact for section – 1 and section – 2

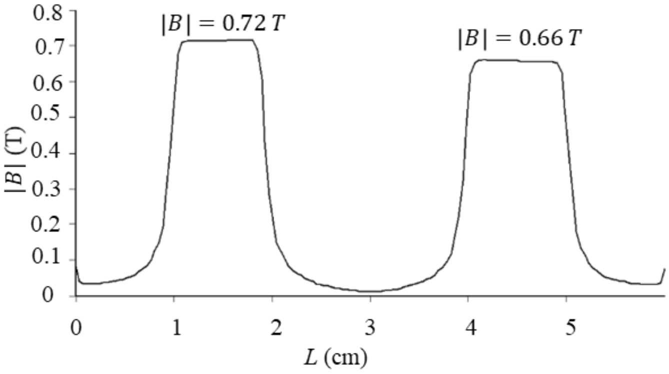

Fig. 3.11 Flux density experienced by platform plate at the contact area

Fig. 3.10 and Fig. 3.11 illustrate that the magnetic flux density for section – 1 and section – 2, at the point of the contact, is 0.66 T and 0.72 T, respectively. By using Equations (31) and (32), the force of attraction at the area of contact for section – 1 and section – 2 is $\mathbf{F_1}$ = 86.7 N and $\mathbf{F_2}$ = – 103.13 N. The negative sign for $\mathbf{F_2}$ states that the direction of force is upward and opposite to the direction of $\mathbf{F_1}$.

The static friction when considering the magnetic flux flow and using a free-body diagram (Fig. 3.8) is:

$$f_s = f_1 + f_2 = \mu\,(W + \mathbf{F_1})cos\,\theta\ + \mu\,(W_{total} - \mathbf{F_2})cos\,\theta$$

$$f_s = \mu\,cos\,\theta\ \left[(W + \mathbf{F_1}) + (W_{total} - \mathbf{F_2})\right] \tag{36}$$

The frictional force is obtained from Equation (36) as f_s =– 4.9 N, where the frictional force is acting upward and opposite to the direction of the gravitational pull of F = 3.528 N.

Since the force due to the gravitational pull is lower than the frictional force, the platform table remains in its position, at an inclination of 45.83°.

3.2 Theoretical implementation of the research result

In this section, we shall investigate the free vibration response for controlled dry friction damping by using the results from the first and second theoretical analysis. This is achieved by theoretically analyzing the response for free vibration of the SDOF spring-mass system with Coulomb damping, provided by the friction between two steel surfaces. Therefore, here, we shall consider a SDOF spring-mass system by using a steel plate of mass *m*, attached to a fixed surface with a spring of spring-constant *k*. The steel plate will be sliding over another steel surface as shown in Fig. 3.12. When the steel plate is displaced from the equilibrium position, it oscillates with a damped natural frequency, where the governing equation is:

$$m\ddot{x} + kx = \mu mg \text{ for } \dot{x} < 0 \tag{37}$$

$$m\ddot{x} + kx = -\mu mg \text{ for } \dot{x} > 0 \tag{38}$$

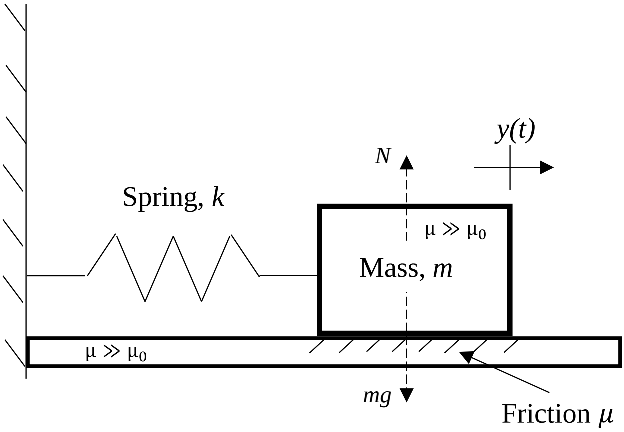

Fig. 3.12 SDOF spring-mass system

For theoretical analysis, we shall consider a steel plate of 5 kg mass, attached to a spring of k = 20 kg/s^2 sliding over a steel platform subjected to sliding friction μ_k = 0.57. Here, two initial conditions are tested, such as: (i) the mass is displaced by 5 cm from the equilibrium, and (ii) the mass displaced by 7 cm from the equilibrium. The particular problem is solved by using *ode45 function* in *MATLAB*. The obtained response plot (Fig. 3.13) illustrates displacement time histories and phase portraits. The displacement time histories explain the response of the mass depending on the displacement from the equilibrium, whereas the phase portraits explain the diminishing nature of velocity on the mass with respect to the displacement from the equilibrium.

The plot, Fig. 3.13 (a) and (b), illustrates that the displacement of the system depends on the force applied to move mass m from the equilibrium, and the resulting response of the system to achieve equilibrium position is determined by the value $m\mu g/k$, which is constant. The displacement histories plot (Fig. 3.13 (a)) demonstrates that, based on the initial displacement of mass m from the equilibrium position, the mass comes to a rest at different positions. Therefore, when the mass is displaced from the equilibrium by y_0 = 5cm, then, after the recoil depending on stiffness k and coefficient of friction μ, the mass comes to rest at a point -0.8 cm away from equilibrium position. Similarly, when the mass is displaced from the equilibrium by y_0 = 7cm, then the mass comes to rest at a point 1.5 cm away from the initial position. We note that the negative or positive signs of the resting position represent the location of the mass from the equilibrium point.

The phase portrait plot (Fig. 3.13 (b)) helps to understand that, based on the initial displacement of mass m from the equilibrium position, the initial velocity (v_0) remains zero, but the velocity achieved from the recoil of mass varies, where, the magnitude of velocity depends on stiffness k, coefficient of friction μ, and moving mass m. The maximum magnitude of velocity achieved by mass m, when the mass is displaced from equilibrium by y_0 = 5cm and y_0 = 7cm are 3.8 cm/s and 5.8 cm/s, respectively.

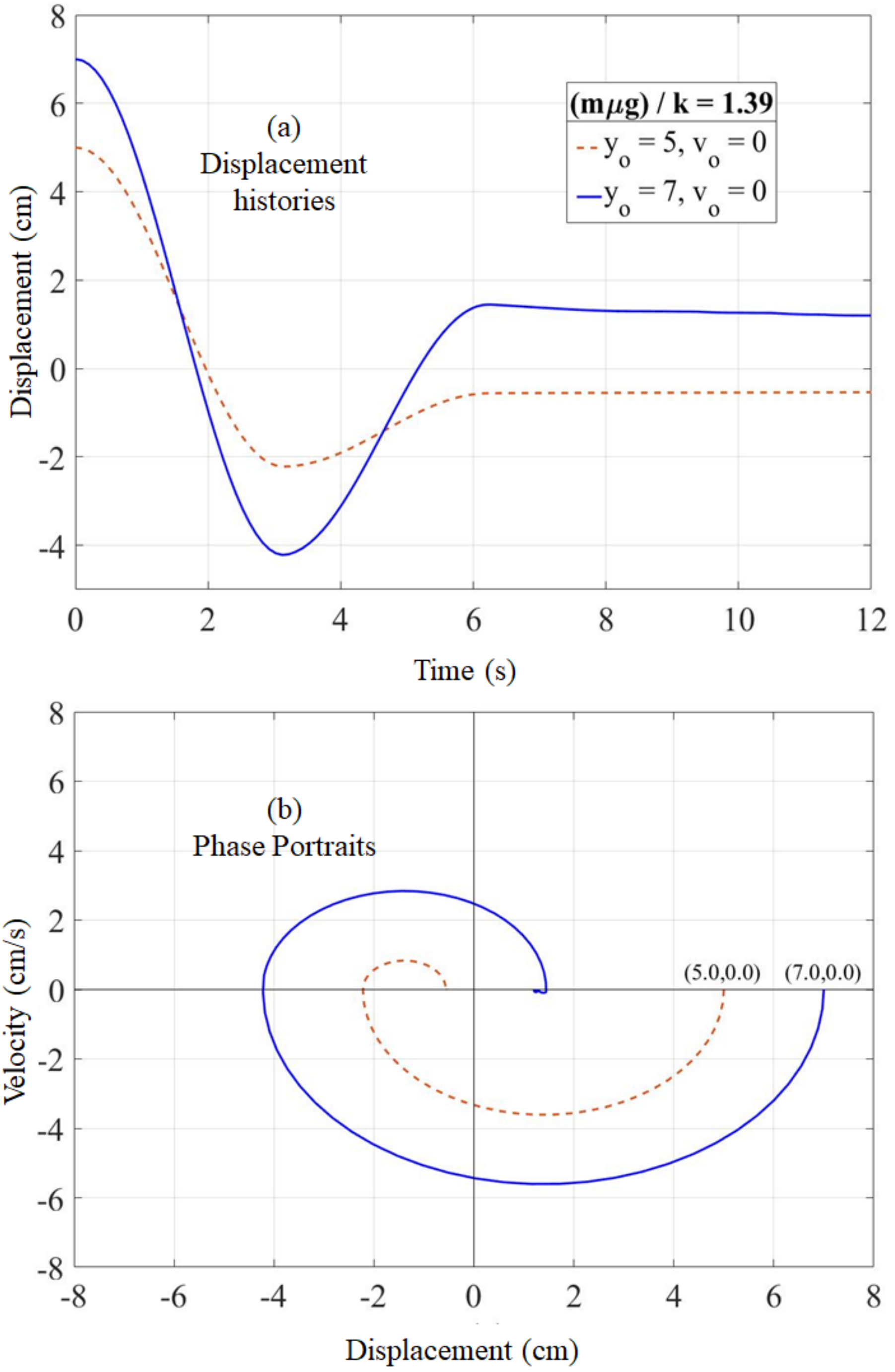

Fig. 3.13 Response plot for ***mμg /k***: (a) displacement histories; (b) phase portraits

Now, by considering the system with magnetic latching so that to increase the normal force, we shall be analyzing the free vibration response (Fig. 3.14). In reality, the steel plate will be subjected to nonlinearity in the force of attraction, based on how close the moving steel plate is to the source of the magnetic flux in an area. For the current theoretical investigation of free-response vibration, we shall consider that the steel plate is moving within an area where the force of attraction is constant (linear).

Similar to the above conducted analysis (Fig. 3.13), for the steel plate of 5 kg mass, attached to a spring of k = 20 kg/s^2, sliding over a steel platform with sliding friction μ_k = 0.57; it is subjected with varying force of attraction. The force of attraction is controlled by using a varying magnetic flux passing through the area of the contact between the steel plate and the platform. The SDOF spring-mass system and the force schematic for magnetic latching is shown in Fig. 3.14. The force of attraction that can be obtained by using the varying magnetic flux are considered to be: 0.0N, 0.08 N, 0.5N, 0.8 N. Also, two initial conditions are considered: (i) the mass displaced by 5 cm from the equilibrium, and (ii) the mass displaced by 7 cm from the equilibrium. The particular problem is then solved in *MATLAB* by using *ode45 function*.

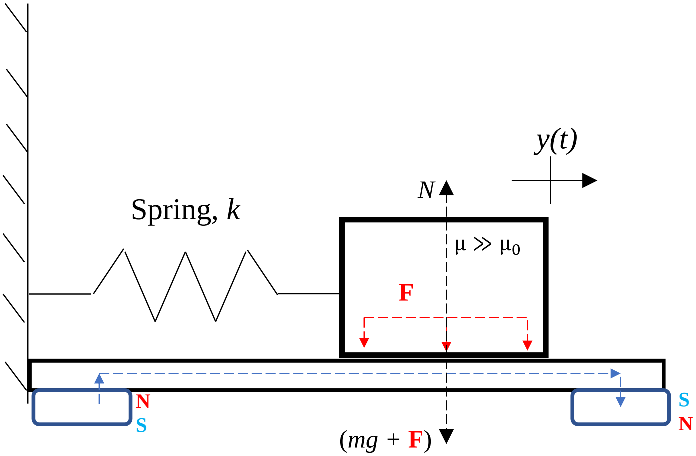

Fig. 3.14 SDOF spring-mass system and the force schematic for magnetic latching

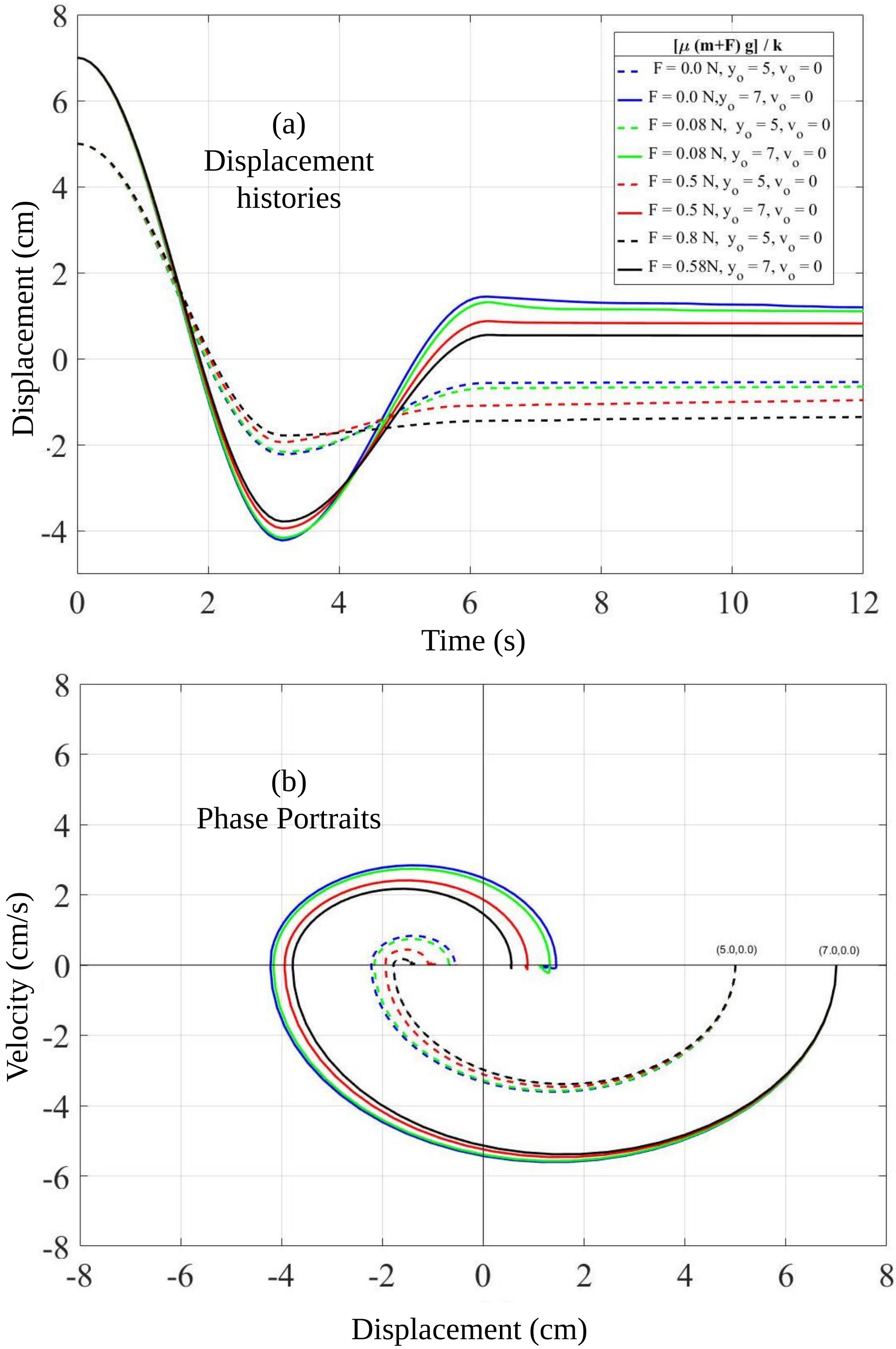

Fig. 3.15 Response plot for $\boldsymbol{\mu}(\boldsymbol{m}+\boldsymbol{F_i})g\,/k$: (a) displacement histories; (b) phase portraits

Plot Fig. 3.13 (a) and (b) verified that the displacement of the system depends on the force applied to move mass m from the equilibrium and the resulting response of the system is defined by $m\mu g/k$, where the value remains constant. Whereas, plot Fig. 3.15 (a) and (b) demonstrates the response for $\mu(m + F_i)g/k$. Here, F_i is the varying values of the attractive force obtained through controlled distribution of the magnetic flux between sliding steel surfaces. The displacement histories plot, Fig. 3.15 (a), demonstrates that, when mass m is displaced from the equilibrium position, then, the mass comes to rest at different positions after the recoil effect. Here, the recoil effect depends on constant values of k and μ and a varying value of the normal force which is directly proportional to F_i.

From Fig. 3.15 (a), when the mass is displaced from the equilibrium by $y_0 = 5$cm, then, the mass comes to rest at points -0.5 cm, -0.64 cm, -0.93 cm and -1.36 cm, for the magnitude of the force of attraction: 0.0N, 0.08 N, 0.5N and 0.8N, respectively. Similarly, for the magnitude of the force of attraction with 0.0N, 0.08 N, 0.5N and 0.8N, if the mass is displaced from the equilibrium by $y_0 = 7$cm, then, the final resting points will be 1.14 cm, 1.07 cm, 0.8 cm and 0.54 cm, respectively, from the equilibrium position.

The phase portrait plot (Fig. 3.15 (b)) helps to understand, based on the initial displacement of mass m from the equilibrium position, where the initial velocity (v_0) on the mass remains zero but the velocity achieved from the recoil of the mass varies, where, the magnitude of the velocity depends on stiffness k, coefficient of friction μ, moving mass m, and varying values of attractive force F_i . The maximum magnitude of the velocity achieved by mass m, when the mass is displaced from the equilibrium by $y_0 = 5$cm and for varying values of attractive force F_i: 0.0N, 0.08 N, 0.5N and 0.8 are 3.8 cm/s, 3.72 cm/s, 3.54 cm/s and 3.36 cm/s, respectively. In the case of the mass being displaced from the equilibrium by $y_0 = 7$cm, the maximum magnitude of the velocity achieved for varying values of attractive force F_i will be 5.63 cm/s, 5.45 cm/s, 5.27 cm/s and 5.09 cm/s.

For the cases ($y_0 = 5$cm or $y_0 = 7$cm) mentioned in designs Fig. 3.12 and Fig. 3.14, the maximum velocity on the mass is recorded at ±1cm from the equilibrium position.

Measurement of the varying frictional force in a real situation would be challenging. Yet, this can be accomplished by measuring the response of the system to the varying force of attraction for system $\mu(m + F_i)g/k$.

For critical damping effects, a model for interlocking the surface by using magnetic latching can be proposed. This is shown in the form of the block diagram in Fig. 3.16. Figure 3.16 explains that, initially, static friction f_s is greater than applied force F, and it results in the steel plates to stay static or interlocked. When the applied force is greater than static friction, then, the surfaces start to move with respect to each other. The steel plates attract each other with force **F** by the method of magnetic latching. This increases the magnitude of normal force $N = mg$ (where m is the mass of the sliding object, and g is acceleration due to gravity) acting between the steel plates. According to the law of friction, the normal force is proportional to the frictional force, so the magnitude of the frictional force also increases with an increase in the magnitude of the normal force, thereby the steel plates will be kept interlocked.

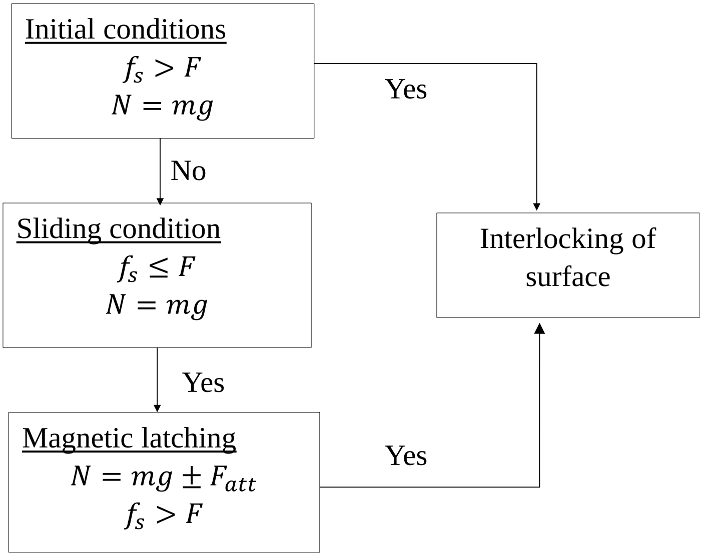

Fig. 3.16 Model for the interlocking of the steel plates by using magnetic latching designed to achieve critical damping effect

3.3 Conclusions of the section

In this section, the friction between steel plates sliding over each other under the influence of the magnetic flux passing through steel was theoreticaly analyzed. The results show that:

1. The magnitude of frictional force f between steel plates can be improved by increasing the magnitude of normal force (N), where the magnitude of the normal force is improved by introducing the force of attraction **F** between steel plates by using the method of magnetic latching.
2. The minimum inclination required for any value of the mass of steel plates to slide from each other under the effect of gravitational pull is $\theta = 36.50°$. At the point of sliding, the magnitudes of gravitational pull and frictional force are equal: $F = f = 2.97$ N. When the steel plates are magnetized, the magnitude of the frictional force was calculated as 3.128 N, which is greater than the magnitude of gravitational pull $F = 2.97$ N. Since the magnitude of the frictional force is slightly greater than the magnitude of gravitational pull, this demonstrates that the steel plates can be static with respect to each other at an inclination $\theta = 36.50°$ as it was explained in the initial theoretical analysis.
3. The intensity of the magnetic flux passing through steel plates can be enhanced by forming a magnetic circuit setup. That means that the magnetic flux from magnet's north pole is directed to the magnet's south pole by using steel plates. This is shown in the second theoretical analysis. From the first theoretical analysis and the second theoretical analysis, the obtained simulation results state that the magnitude of the flux density between steel plates for the first theoretical analysis is $|B| = 0.01$ T, whereas, for the second theoretical analysis,

i.e., for the completed magnetic circuit theory, it is $|B| = 0.69$ T (average value).

4. The minimum inclination required for the stand to slide from the steel platform in the case of the second theoretical analysis is $\theta = 45.83°$. At the time of sliding, it was observed that the magnitudes of the gravitational pull and the frictional force are equal: $F = f = 3.528$ N. Also, the magnitude of the frictional force, when the magnetic flux is passing through steel plates, is calculated as 4.9 N, which is greater than the magnitude of the gravitational pull $F = 3.528$ N. This results in keeping the stand static with respect to the steel platform at an inclination $\theta = 45.83°$.
5. The theoretical implementation of the research result is done by considering the response for free vibration of the SDOF spring-mass system with Coulomb damping, where two steel surfaces slide over each other. Two theoretical setups are considered:
   a. Analysis of spring mass Coulomb damping and the investigation of response for $m\mu g/k$ by using *MATLAB*.
   b. In the second part, analysis was done for controlled Coulomb damping, and a response plot for $\mu(m + F_i)g/k$ was produced by using *MATLAB*.
   c. Measuring the varying frictional force would be challenging in a real-life situation. Yet, this can be accomplished by measuring the response of the system to the varying force of attraction for system $\mu(m + F_i)g/k$.
6. Finally, a model for interlocking of steel plates was designed in the form of a block diagram. This idea can be further used to develop the control system for critical damping.

4. ANALYSIS OF THE POSSIBILITY FOR ELECTROMAGNETIC DEVICES TO ATTENUATE MICRO-VIBRATION BY VARYING THE RESONANCE OF THE SYSTEM

Previous chapters addressed structural damping concerning the direct contact between surfaces. This chapter shall investigate the aspects of vibration attenuation by generating counterforce while using an additional damping unit (as electromagnetic devices without any fluid) in which, the target structure is suspended.

In the current research, the ability to use electromagnetic devices to create the required counterforce to attenuate vibration by varying the stiffness of the system is investigated. In the previous research work on the development of the electromagnetic damper [38], a working principle consisting of three stages of vibration attenuation was evaluated. Stage – 1 was achieved by utilizing the counterforce generated from moving a magnetic piston along a copper pipe. Stage – 2 and Stage – 3 were achieved by using a two-coil system. Here, the coils were excited by using feedback control with the help of a displacement sensor and a microcontroller so that to oppose the downward movement of the magnetic piston.

Working Principle

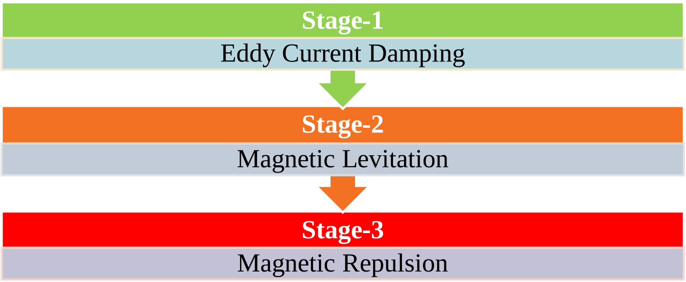

Coil activation sequence

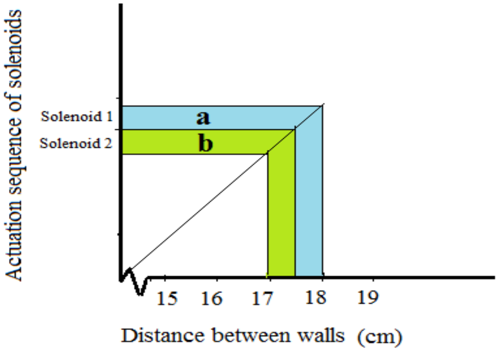

Fig. 4.1 Development of electromagnetic damper [38]

4.1 Theoretical analysis of the development of electromagnetic dashpot

In this section, theoretical analysis is considered to understand the electrodynamic forces generated when a magnetic piston moves through:

a. a copper pipe where eddy current and Lorentz force generation is analyzed, and
b. a two-coil system supplied with direct current resulting in electrodynamic repulsive forces.

4.1.1 Analysis of Lorentz force in eddy current damping

The Lorentz force generated in the walls of a copper tube, due to the eddy current formation from sudden movement of a permanent magnet, can be used to design passive dampers so that to attenuate vibration.

Let us consider a thin circular loop of a copper tube where the magnet passes through, as shown in Fig. 4.2. Then, the electromagnetic force generated due to the eddy currents at point $P(R, \theta, z)$, on the copper wall, is illustrated in the schematics of the circular magnetic strip. Here, current density $\vec{J}$ is induced in the copper walls, thus experiencing velocity $\vec{v}$:

$$\vec{J} = \sigma(\vec{v} \times \vec{B}), \tag{39}$$

where, σ is the conductivity of a conducting material, $(\vec{v} \times \vec{B})$ is the electromotive force driving the eddy current $\vec{J}$, $\vec{B}$ is the magnetic flux density at point P.

We apply the Biot-Savart law [64] at the vector of infinitesimal strip $d\vec{l}$:

$$d\vec{B} = \frac{\mu_0 M_0}{4\pi} \frac{d\vec{l} \times \hat{R}_1}{R_1^2}, \tag{40}$$

where, μ_0 is the permeability of a conducting material, M_0 is magnetization per unit length, $\hat{R}_1$ is the vector from the source point to the field point, $d\vec{l}$ is the vector of the infinitesimal strip.

The electromagnetic force due to the eddy current can be expressed as:

$$\vec{F} = \int_r \left(\vec{J} \times \vec{B}\right) dV. \tag{41}$$

Damping force $\vec{F_d}$ due to the eddy current in z direction is:

$$\vec{F_d} = v.\, 2\pi\sigma\delta\, y \int B_y^2\, (y, z, z_1) dz\, (-\vec{a}_2), \tag{42}$$

where, δ is the thickness of a copper tube, v is the vertical velocity of the magnet.

Here, the eddy current damping coefficient can be expressed as:

$$c_d = v.\, 2\pi\sigma\delta\, y \int B_y^2\, (y, z, z_1) dz\, . \tag{43}$$

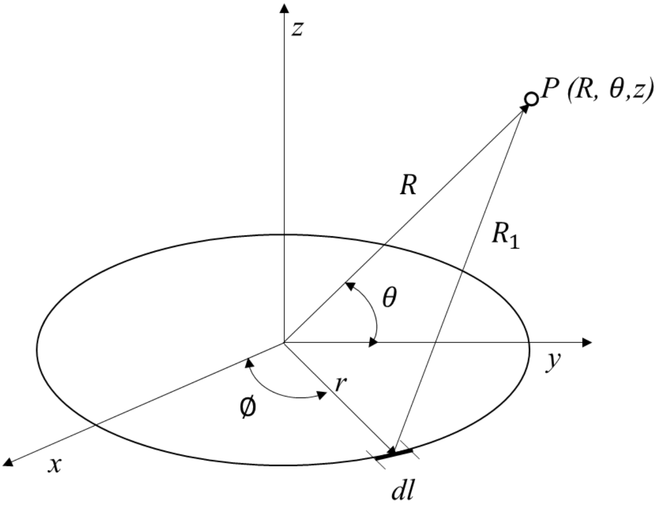

Fig. 4.2 Schematics of circular magnetic strip

The governing equation of a magnet of mass ***m*** falling through a copper tube is:

$$W - F_d = mg - c_d v = m\frac{dv}{dt}, \tag{44}$$

Integrating the above equation gives the following relation of damped velocity:

$$v(t) = \frac{mg}{c_d}\left(1 - e^{\frac{c_d}{m}t}\right). \tag{45}$$

Let us consider a magnetic piston head of the following dimensions: height *h* = 18 mm and diameter = 15 mm which is considered to move through a copper pipe of 0.2 mm thickness and 16 mm inner diameter. The Lorentz force generated in the setup is then evaluated by using *COMSOL Multiphysics 5.3*.

Figure 4.3 shows the magnetic flux density formed inside the system, whereas Fig. 4.4 represents the plot of the increasing Lorentz force with respect to velocity. It was noticed that the force generated inside the system increases gradually and comes to a constant value. The maximum achievable value by using the current setup is observed as 0.26 N.

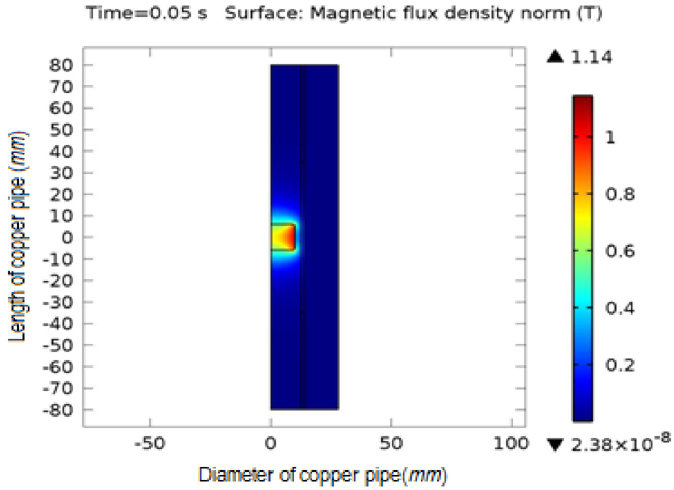

Fig. 4.3 Magnetic flux density formed inside the system

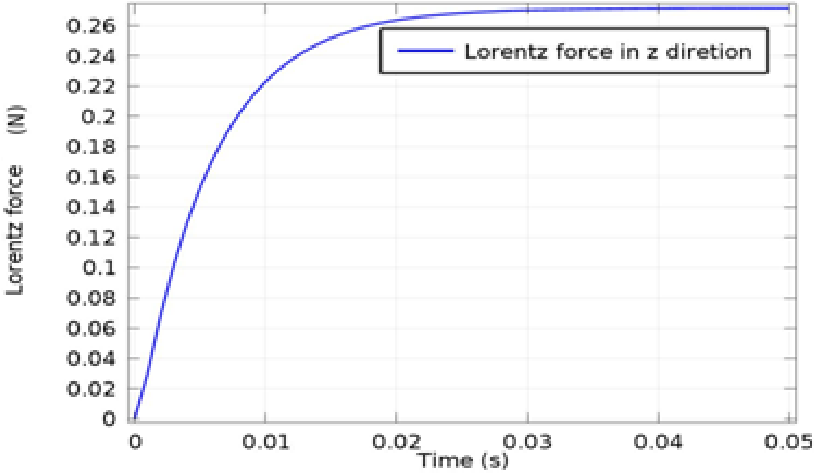

Fig. 4.4 Lorentz force generated inside the system

4.1.2 Analysis of electromagnetic force generated inside solenoid setup

As the eddy current effect results in the Lorentz force, an excited coil and a permanent magnet can also be used for creating the repulsive and attractive electrodynamic forces. The generated forces can be used for designing the dashpot to attenuate vibration.

Here, the resultant force by the coil depends on the length, the air gap, the number of turns in the coil, the applied current, and the type of the permanent magnet in use. The force diagram for one turn of the coil excited with current *i* is presented in Fig. 4.5.

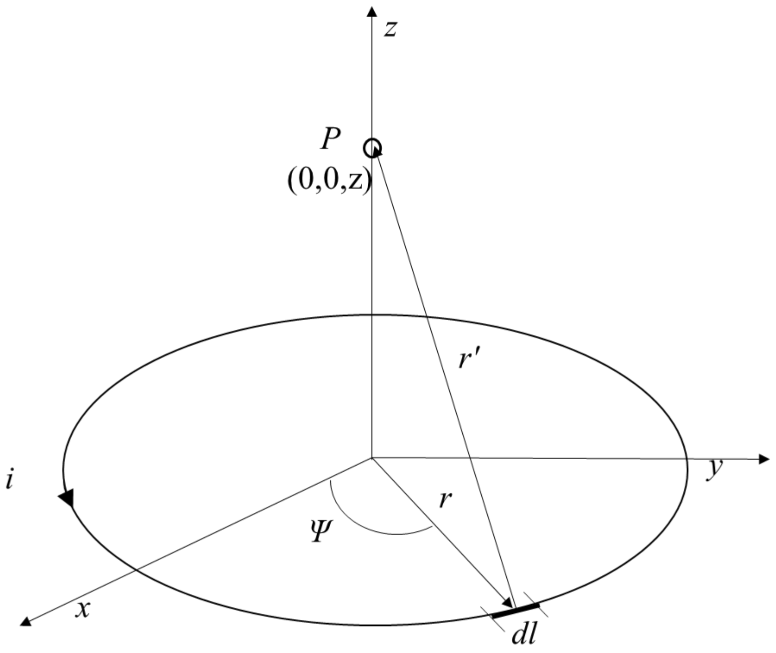

Fig. 4.5 Force diagram for one turn of coil excited with current *i*

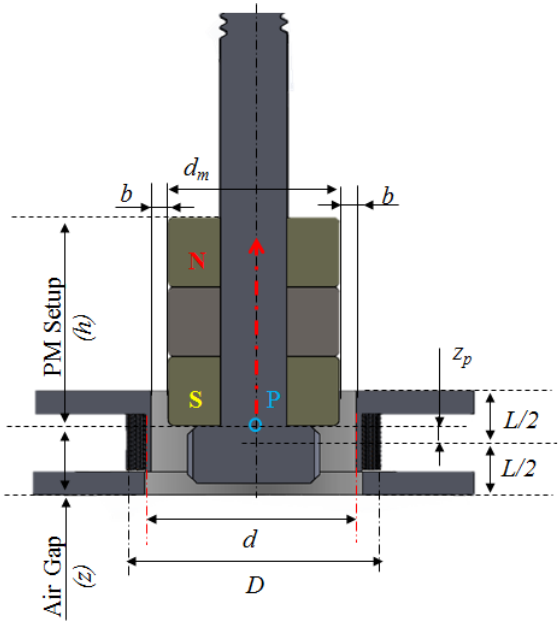

Fig. 4.6 Parameters of electromagnetic dashpot

The magnetic field along the axis of a circular current loop of radius *r* and steady current *i* (Fig. 4.5) can be expressed by using the Biot-Savart law [64]:

$$B = \frac{\mu_0 i}{4\pi}\int \frac{dl\prime \times r\prime}{|r\prime|^3}\,, \tag{46}$$

where, dl' and r' are the line segment and the distance from the viewpoint to the source charge and the permeability of vacuum $\mu_0 = 4\pi \times 10^{-7}$ Wb/Am.

From the force diagram (Fig. 4.5): $' = Rd\psi\hat{\psi}$, $r' = z\hat{z} - r\hat{r}$ and $|r'| = \sqrt{z^2 + r^2}$. The magnetic field by the coil $B_{coil,z}$ at arbitrary point P on the axis of the current loop is:

$$B_{coil,z} = \frac{\mu_0 i r^2}{4\pi}\int_0^{2\pi} \frac{d\psi}{(r^2+z^2)^{\frac{3}{2}}}\hat{z} = \frac{\mu_0}{2}\frac{ir^2}{(r^2+z^2)^{\frac{3}{2}}}\hat{z}. \tag{47}$$

The following design parameter for the electromagnetic dashpot (Fig. 4.6) is considered:

a. a coil of length L, outer diameter D and inner diameter d;
b. air gap z;
c. the height of the magnet h;
d. the distance of point P from the center of the solenoid z_p, and
e. the thickness of the guider b.

The electromagnetic field of the coil can be obtained by using Ampere's law in its integral form. By introducing the electromagnetic dashpot parameters, the axial electromagnetic field of the coil is expressed by using Equation (47):

$$B_{coil,z} = \int_0^L \int_{\frac{d}{2}}^{\frac{D}{2}} \frac{\mu_0 n i r^2}{2\left[r^2+\left(z_p+\frac{L}{2}-z\right)^2\right]^{\frac{3}{2}}}\hat{z}drdz, \tag{48}$$

where, $n = N/L$ represents the turn density per unit length.

The air gap or the moving distance of the permanent magnet inside the solenoid is given by $z = L/2 + z_p$. The electromagnetic field at point P thus becomes:

$$\begin{aligned} B_{coil,z} = {} & \frac{\mu_0 Ni}{2L(D-d)}\left(L+2z_p\right)ln\left[\frac{D+\sqrt{D^2+\left(L+2z_p\right)^2}}{d+\sqrt{d^2+\left(L+2z_p\right)^2}}\right] \quad . \\ & +\frac{\mu_0 Ni}{2L(D-d)}\left(L-2z_p\right)ln\left[\frac{D+\sqrt{D^2+\left(L-2z_p\right)^2}}{d+\sqrt{d^2+\left(L-2z_p\right)^2}}\right]\hat{z}. \end{aligned} \tag{49}$$

The electromagnetic force acting on the permanent magnet can be expressed as:

$$\begin{aligned} F_z(z,i) = {} & \int\left(-\nabla \cdot M_{mag}\right)B_{coil,z}dV \\ & +\int\left(M_{mag}\cdot\hat{n}\right)B_{coil,z}ds, \end{aligned} \tag{50}$$

where, the external magnetic field produced by the $B_{coil,z}$ is equal to $B_{coil,z}\hat{z}$.

Magnetic flux ϕ is equal to the direction of the external magnetic field $B_{coil,z}$ and its magnitude can be calculated from Equation (49). Taking into account that the magnet has a fixed and uniform magnetization $M_{mag} = -M\hat{z}$ in the direction of the longitudinal axis of the coil, the unit surface normal vector $\hat{n}$ becomes $-\hat{z}$ for $z = 0$, and $\hat{n}$ becomes $\hat{z}$ for $z = h$. Hence, surface charge density σ_m can be calculated as:

$$\sigma_m = M_{mag} \cdot \hat{n} = \left\{ \begin{array}{l} M, z=0 \\ -M, z=h \end{array} \right. . \tag{51}$$

Initially, the north pole of the permanent magnet enters the field of the coil. Since uniform magnetization M_{mag} has no divergence, it helps to define $M = \frac{B_r}{\mu_0}$, where B_r is the remnant flux density of the permanent magnet. Here, the magnetic volume charge density is $\rho_m = -\nabla \cdot M_{mag} = 0$. Finally, the expression for the electromagnetic force can be written as:

$$\begin{aligned} F_z(z,i) &= \int \sigma_m B_{solenoid,z} ds \\ &= \frac{B_r}{\mu_0} B_{solenoid,z} \int_0^{2\pi} \int_0^{d/2} r dr d\psi \\ &= \frac{B_r B_{solenoid,z} A}{\mu_0} \hat{z} \end{aligned} \tag{52}$$

where, $A = \pi(\frac{d}{2})^2$ is the area by the inner diameter of the coil.

Here, the electromagnetic force is proportional to the magnetic field by the coil $B_{coil,z}$ and the remnant flux density of magnet B_r. The electromagnetic force can be analyzed numerically by using Equation (52), and, for the theoretical analysis, an ideal magnetic circuit is considered, where the magnetic fringe and the magnetic leakage are ignored.

For simulation, let us consider a coil of inner diameter $d+b$ = 19.2 mm, outer diameter D = 22.3 mm, and length L = 20 mm. The coil is constructed by using a wire of diameter 1 mm, and the number of windings in the coil is N = 60 turns. Inside the coil, a cylindrical magnetic piston head setup of height h = 18 mm and outer diameter d_m = 15 mm is used. Here, the coil is excited at 1 Amp.

Simulation is done to analyze the electromagnetic force at point P for different values of z_p by using software *FEMM 4.2*. Point P of the magnet is considered to move downwards from above the center of the coil at height z_p = 12.55 mm till the center of the coil is z_p = 0 mm as shown in Fig. 4.7.

The electromagnetic force acting at point P for different values of z_p is analyzed. It can be observed that, by reducing distance z_p of the electromagnetic force, the force on the magnet is reduced, and it is at its maximum at a region just above the coil (Table 4.1). The force increases slightly (Table 4.1 – Nos.: 12–16) near the edge of the coil and then diminishes as the magnet head reaches the center of the coil. The result is illustrated as a graphical plot in Fig. 4.8.

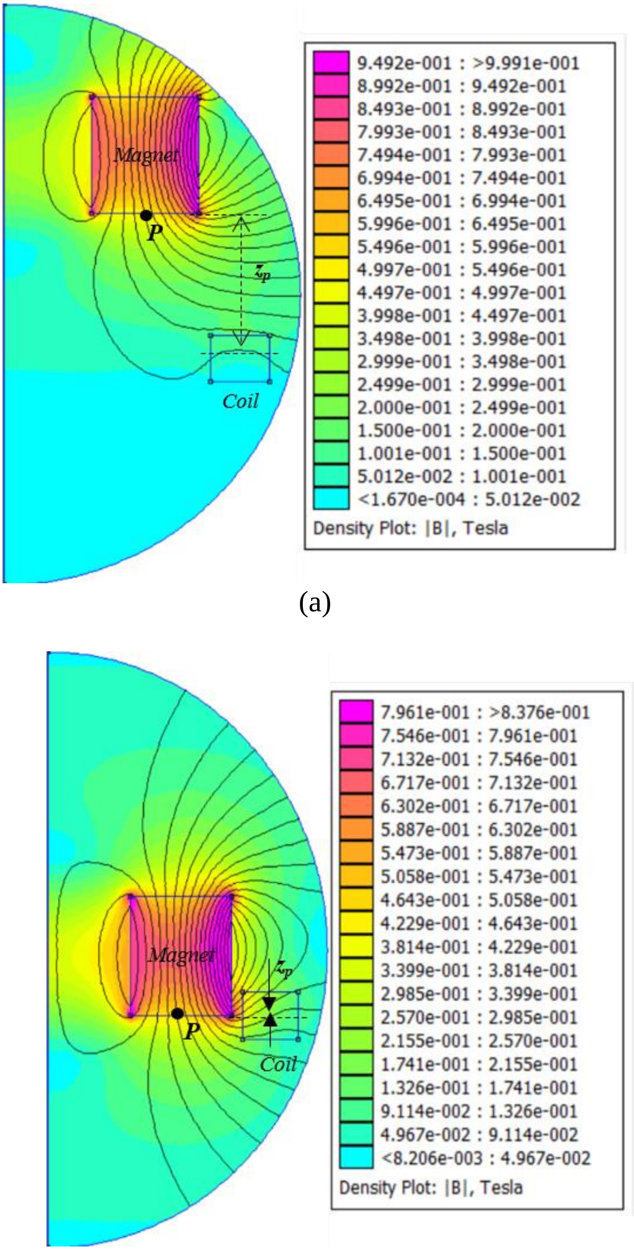

(a)

(b)

Fig. 4.7 Flux density plot: (a) above center $z_p = 12.55$ mm; (b) at the center $z_p = 0$ mm

Table 4.1 Electromagnetic force acting at point P for various values of z_p

No.	Point *P* from the center of coil z_p, mm	Electromagnetic force at point *P*, *N*
1	12.5	63.7337
2	11.71875	52.1639
3	10.9375	44.1328
4	10.15625	38.2141

5	9.375	34.4884
6	8.59375	31.1854
7	7.8125	29.087
8	7.03125	27.3833
9	6.25	26.5266
10	5.46875	25.9332
11	4.6875	25.8288
12	3.90625	26.0789
13	3.125	26.4515
14	2.34375	26.6119
15	1.5625	26.9047
16	0.78125	26.3681
17	0	24.5376

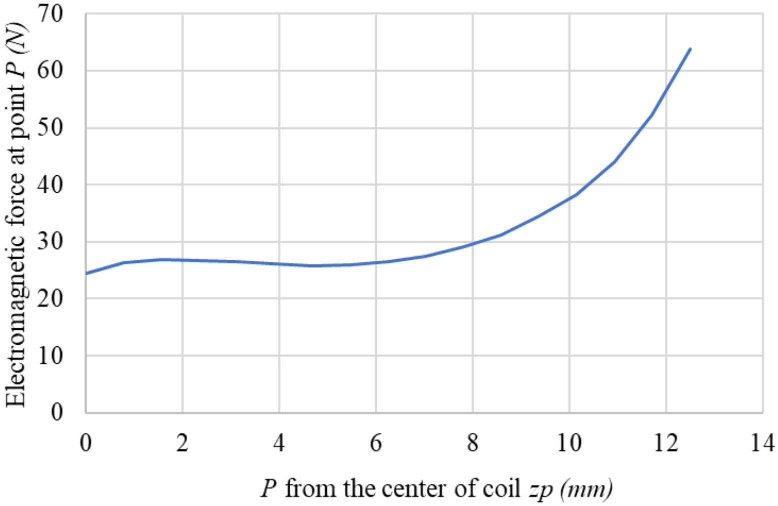

Fig. 4.8 Plot: electromagnetic force acting at point P with respect to z_p

4.2 Design and development of test setup

For the current section (Section 4), two types of attenuation methods are overlooked and investigated. One is the use of the Lorentz force from eddy current dampers to attenuate micro-vibration, Fig. 4.9 (a), whereas the second type is the force generated due to the electrodynamic effect from two excited coils, Fig. 4.9 (b). In order to experimentally study the two different dashpots, a dedicated test setup is necessary. Therefore, a test setup is developed by considering: (i) the design of a magnetic piston, (ii) the study of the development of test setup requirement, (iii) the study of eccentric rotating mass for harmonic excitation, and (iv) analysis of the response of the active plate where the measurement for vibration will be logged.

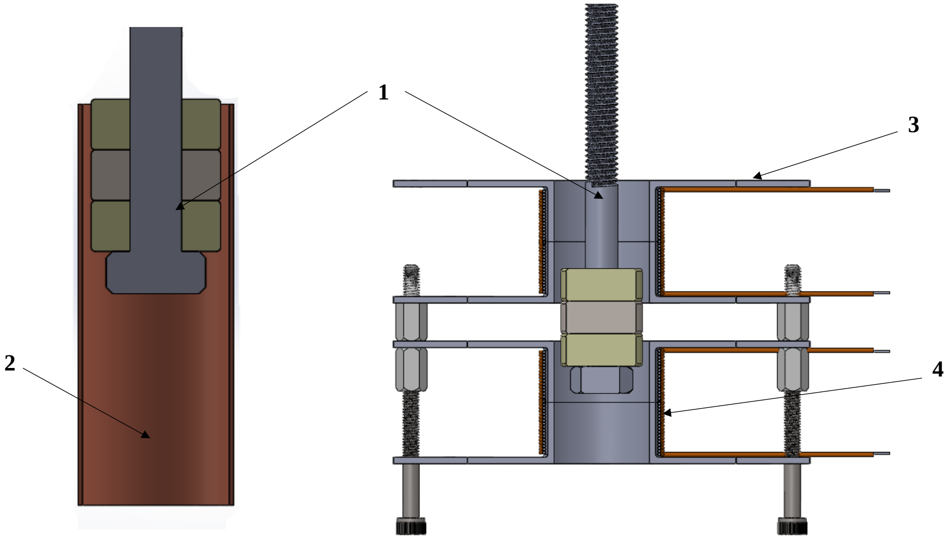

(a) (b)

Fig. 4.9 Dashpot concepts: (a) magnetic piston inside a coper pipe, and (b) magnetic piston inside a coil
1 – magnetic piston; 2 – copper pipe; 3 – coil – 1; 4 – coil – 2

4.2.1 Design of magnetic piston

The magnetic piston consists of an M6 steel bolt, in which, a circular steel spacer is sandwiched between two neodymium magnets. The steel spacer helps to get an arrangement where the south poles of the magnets are forced to stay together (Fig. 4.10 (a)). Bringing the two repulsive poles together helps to increase the span of the magnetic flux density in the area near the steel spacer, thereby providing enhanced repulsive force while it is displaced inside the excited coil’s magnetic field.

The neodymium magnet in use is NdFeB, of dimensions Ø 15 x 6 x 6 mm, with coating Ni-Cu-Ni and a strength of 50.4 N. The weight of each magnet is 6.8 g, and the maximum working temperature is 80 °C. The steel spacer is of the same dimensions as magnets, and its weight equals 7 g.

Based on the early-stage research on the development of an electromagnetic damper [38], it was observed that it should have a two-coil system so that to enhance the counterforce. Therefore, a two-coil system shall be used to analyze the electromagnetic dashpot, where the magnetic piston will be placed in such a way that the repulsive forces are at their maximum (Fig. 4.8).

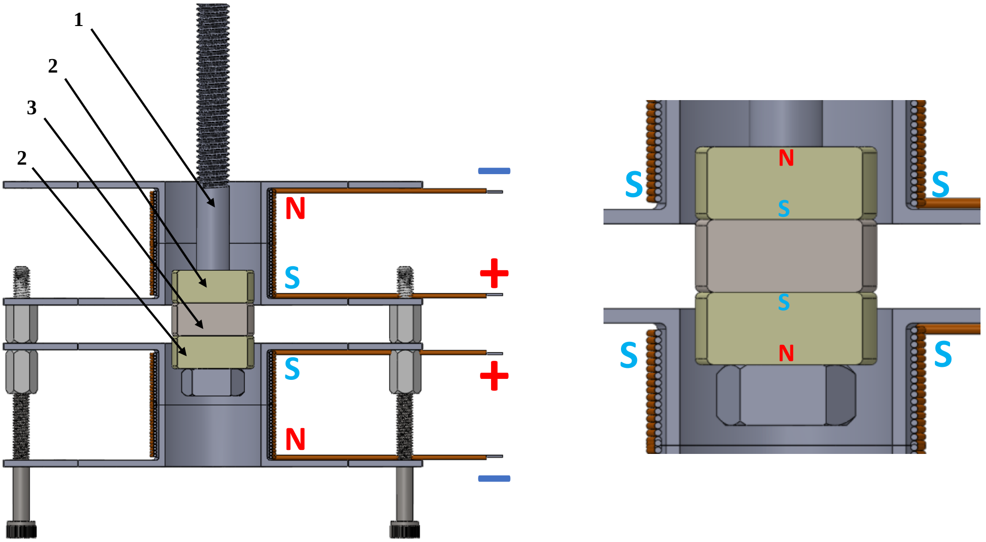

Fig. 4.10 Magnetic piston arrangement inside a two-coil system: 1 – steel bolt; 2 – neodymium magnet; 3 – steel spacer

4.2.2 Requirements for the test setup

It is necessary to have a test setup which supports a low amplitude and varying frequency ranges while conducting experiments related to the electromagnetic dashpot. It is also required that there is no other electromagnetic interference during the experimental tests. Therefore, electrodynamic shakers are avoided, and a test setup similar to the concept illustrated in the Fig. 1.2 (Section 1.1) is considered. Here, the excitation of the system will be provided by the eccentric rotating mass. The considered experimental test setup is shown in Fig. 4.11.

The setup consists of 3D printed parts from PLA so that to avoid the force of attraction from ferrous surfaces. The metal parts in the design are placed in such a way that there is no influence of attractive forces, which can exert influence on the forces inside the dashpot. The frequency ranges of the system are tuned by loading the springs, and an eccentric mass rotation (EMR) system is used for harmonic excitation. In order to avoid external disturbance, the test is conducted on an optical table. Therefore, a wooden block is mounted in between the test setup and the optical table as the working surface of the optical table is from stainless steel.

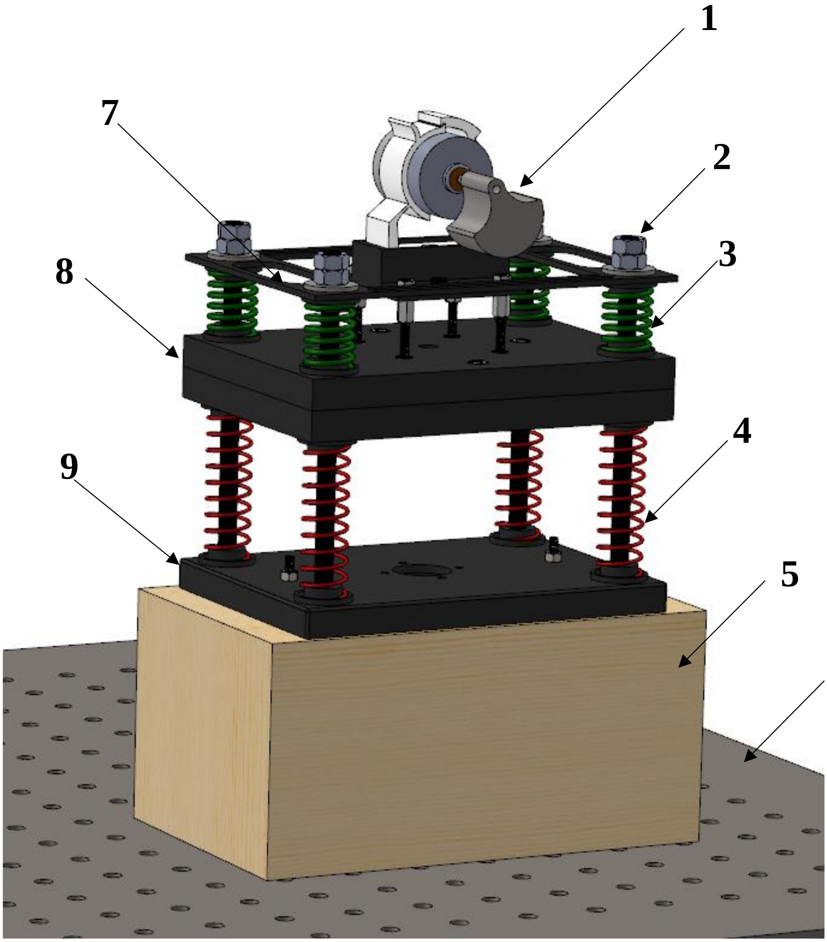

Fig. 4.11 Concept of the experimental test setup: 1 – eccentric rotating mass; 2 – tuning nuts; 3 – tuning springs; 4 – support springs; 5 – wooden block; 6 – optical table (working surface from stainless steel); 7 – alignment plate (PLA); 8 – active plate (PLA); 9 – base plate (PLA)

4.2.3 Modelling of eccentric rotating mass (ERM)

The required harmonic excitation force and frequency is controlled by using ERM, hence, modelling of the required ERM system is necessary. The force generated by such a system is nonlinear, yet, for the current test, we shall consider only the lateral force presently treated as a linear force. The objective of using ERM is to displace the active plate which is supported by 4 springs, in parallel, by 5 to 10 mm. Here, the spring constant of each spring is $k = 1.30667$ N/mm.

Let us consider a SDOF system as shown in Fig. 4.12. Here, e is eccentricity of mass, m_u is unbalanced mass, M is the total mass of the active plate, k is the spring constant, c is the damping coefficient of the spring, x is the displacement, Ω is the rotating speed of the shaft (motor), t is the time period, and Ωt is the angular displacement.

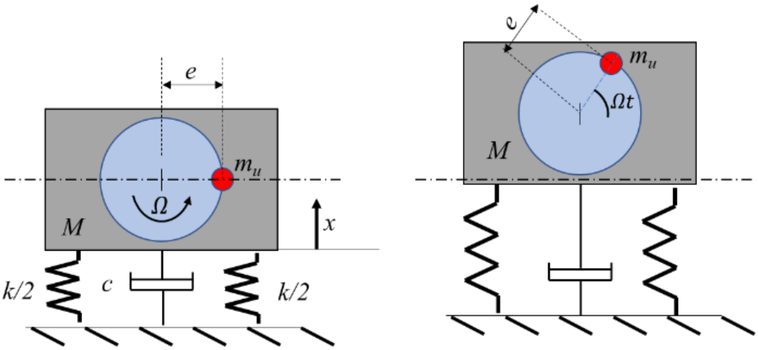

At time $t = 0$, in equilibrium

After a period t.

Fig. 4.12 SDOF model for ERM

The respective equation of motion for the above model is given by:

$$M\ddot{x} + c\dot{x} + kx = F_0 \ \sin\omega \ . \tag{51}$$

This can be rewritten as:

$$M\ddot{x} + c\dot{x} + kx = (m_u\Omega^2 e) \ sin\,\omega \ , \tag{52}$$

where:

$$F_0 = m_u\Omega^2 e \ . \tag{53}$$

By considering the force that ERM has to produce is between 0–60 N, then, the following values are implemented as m_u = 0.5 kg, Ω = (1000 rpm *2 π) /60 = 104.71975512 rad/s, and e = 0.011 m = 1.1 cm. Based on Equations (51), (52), and (53), a design chart is formulated by using *MATLAB*, and this is illustrated in Fig. 4.13.

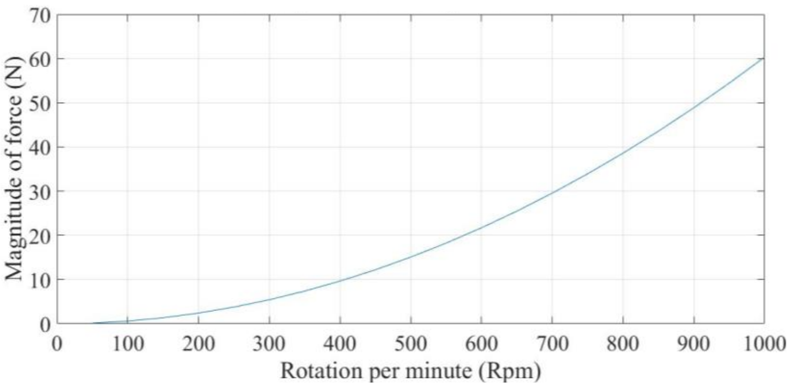

(a)

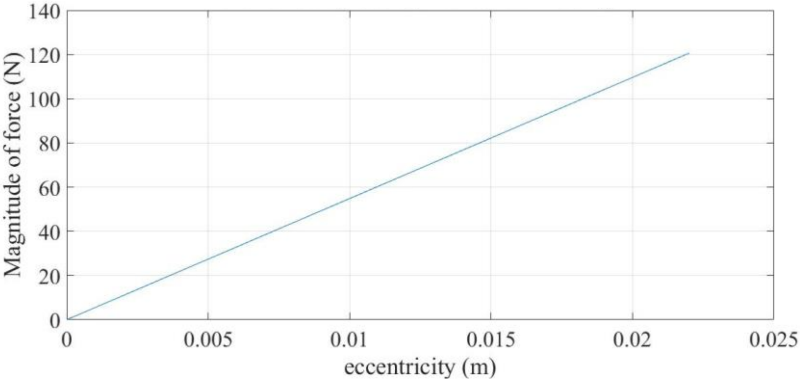

(b)

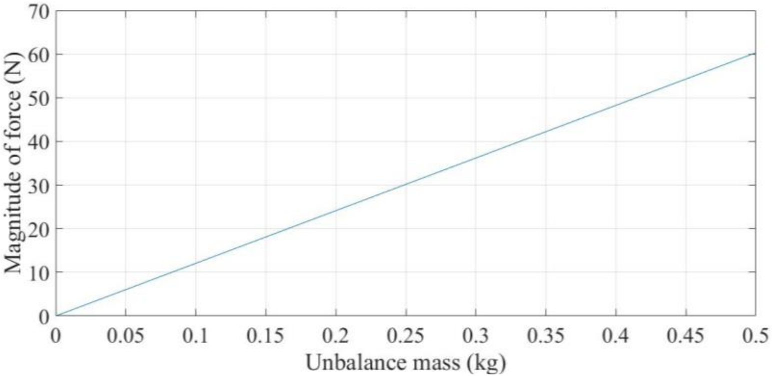

(c)

Fig. 4.13 Design chart to model the necessary ERM: (a) varying magnitude force with respect to varying rpm; (b) varying force with respect to varying eccentricity value, and (c) varying force concerning the varying eccentric mass

From the charts (Fig. 4.13), eccentric mass m_u = 0.3 kg, motor of Ω < 1000 rpm and eccentricity less than 15mm are considered for the development of ERM for the experimental setup.

4.2.4 Active plate response analysis

The active plate is the suspended part between the support spring and the tuning spring, see Fig. 4.11. The response of the system is analyzed in the active plate. Therefore, understanding the free response of the plate is significant.

Three cases were considered (Fig. 4.14): one without bearing, the second with linear ball bearing, and the third with polymer bushing. The three cases were evaluated separately through the impulse test. For each case, the plates were mounted as per design shown in Fig. 4.11, and the tuning nut was adjusted to known limits so that to avoid large deviation in spring constants.

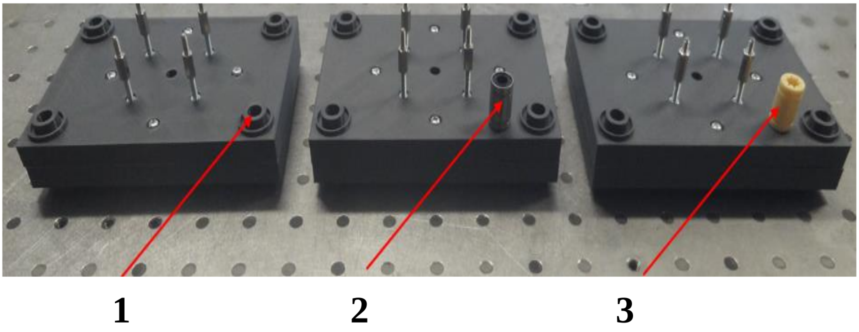

Fig. 4.14 Three cases of the active plate response design: 1 – without bearing; 2 – linear ball bearing; 3 – polymer bushing

The impulse test is done by striking on the plate's center, where ERM is mounted by using a tool with medium hard rubber. Then, the response of the system is recorded by focusing the rays of a laser displacement sensor LK-G82 on the top of an active plate, Fig. 4.17. Throughout the experimental research, the spot of the ray will be focused on the same place.

The tool used here was a handle of a screwdriver tip. The strikes may vary; therefore, five different samples were made for each case. After analyzing the samples for each case, the considered response result is presented in Fig. 4.15.

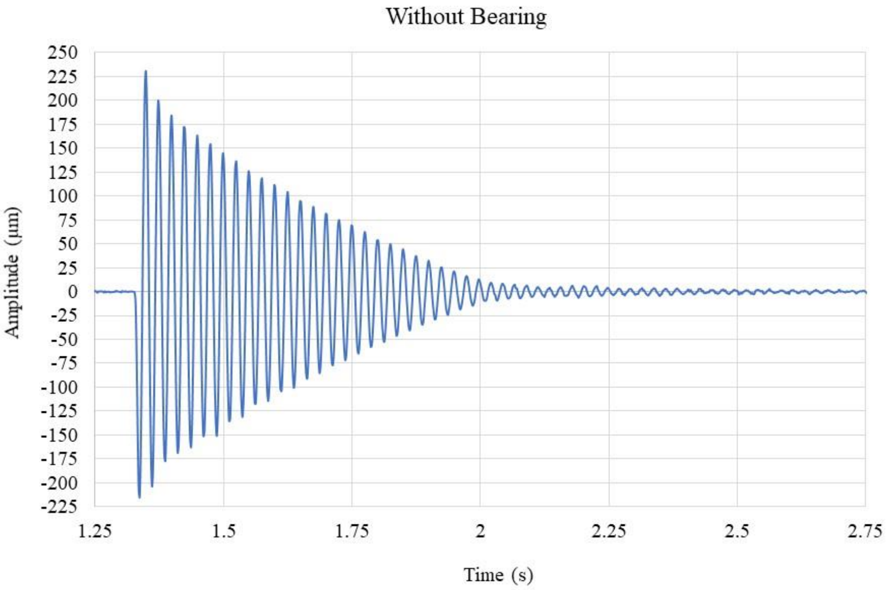

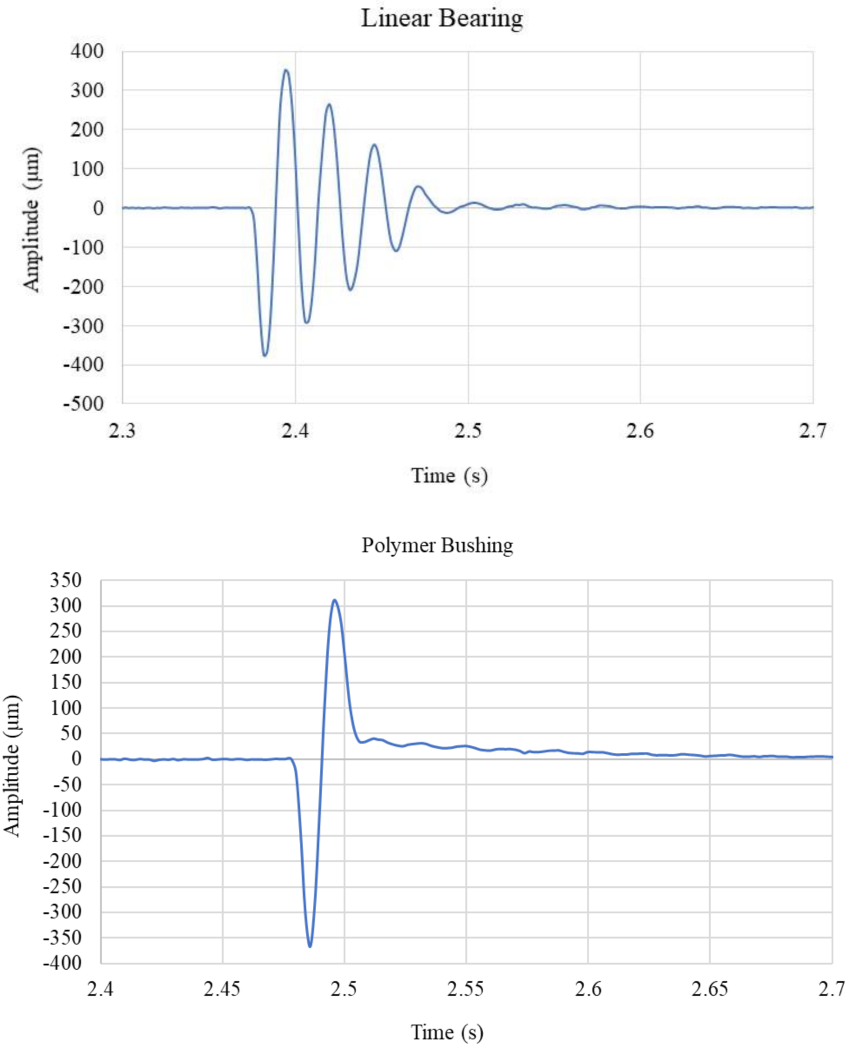

Fig. 4.15 Impulse test results for different types of bearing in use

Through the impulse test, the results for the desired motion of the active plates were determined (Fig. 4.15). Without bearing, the observed damping ratio is 0.02071, whereas the polymer bushing showed strong damping properties with a damping ratio value of 0.35766. The linear ball bearing showed a damping ratio of 0.14761, which is the optimal damping, and the response nature of the test setup showed closer resemblance to a realistic problem of structural vibration, where the structure can possess structural damping.

4.2.5 Final test setup

Based on the results from the previous sections, the final mechanical design of the test setup is illustrated in Fig. 4.16. Figure 4.16 (a) shows a system with a dashpot to test the attenuation of vibration by using the Lorentz force, and Fig. 4.16 (b) is the system with a two-coil system.

A motor controller is used to control the force generated from ERM. The coil for generating the repulsive electromagnetic force is controlled by using a separate PWM motor controller which supports the max current of 20 Amp, and the max power of 1200 W, which is manually controlled

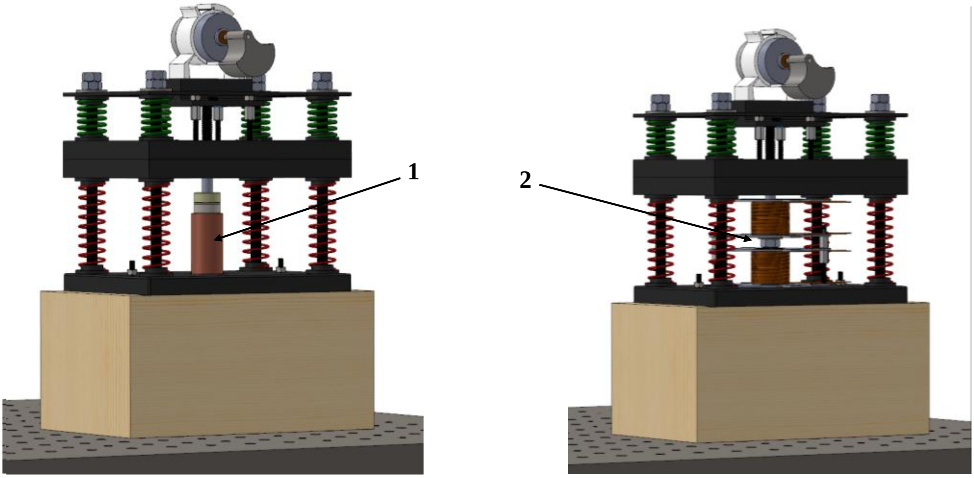

(a) (b)

Fig. 4.16 Required experimental test setups: (a) dashpot from a copper pipe, and (b) dashpot from the two-coil system
1 – dashpot from copper pipe; 2 – dashpot from the two-coil system

4.3 Experimental analysis and discussions

In this section, the attenuation of micro-vibration using the Lorentz force and a two-coil system is experimentally investigated. The experimental investigation also included the study of the heat build-up in the two-coil system.

4.3.1 Experimental setup

An experimental setup as illustrated in Fig. 4.17 is used for the test. The required amplitude and frequency of vibration is created by using ERM; control is performed by using an ERM controller. Also, the frequency of vibration can be slightly varied by using the tuning nut. Here, the micro-displacements are analyzed by using a laser displacement sensor LK-G82. The reading from the sensor is collected by using a PicoScope which is connected to a computer.

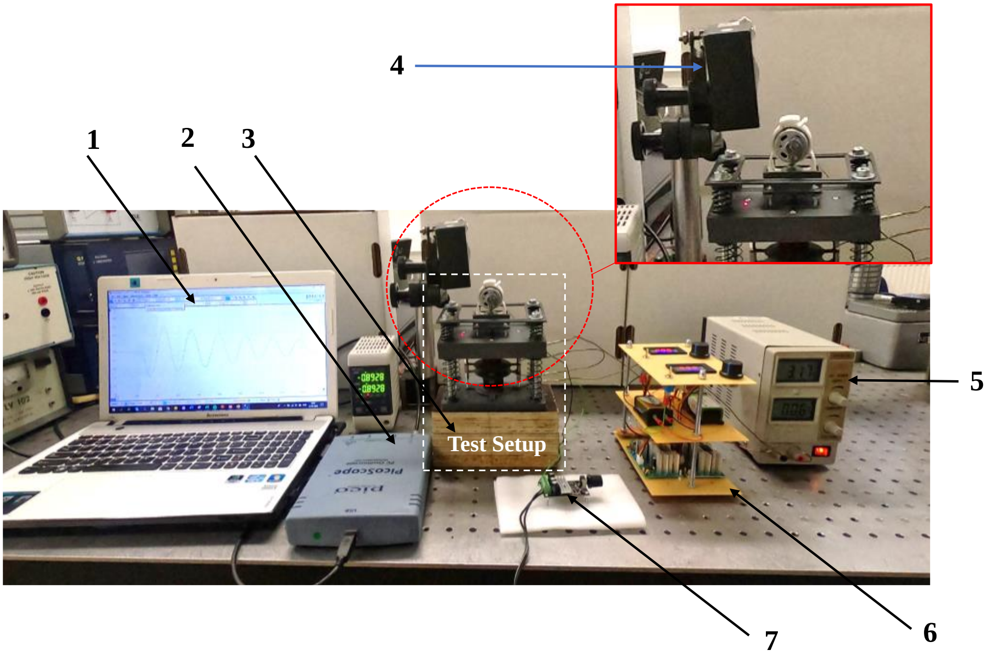

Fig. 4.17 Experimental setup: 1 – computer; 2 – PicoScope; 3 – test setup; 4 – laser displacement sensor LK-G82; 5 – power supply; 6 – two-coil controller; 7 – ERM controller

4.3.2 Experimental investigation of micro-vibration attenuation using Lorentz force

A magnetic piston head with dimensions: height *h* = 18 mm and diameter = 15 mm is considered to move through a copper pipe with a wall thickness of 0.2 mm is used. The setup is shown in Fig. 4.18.

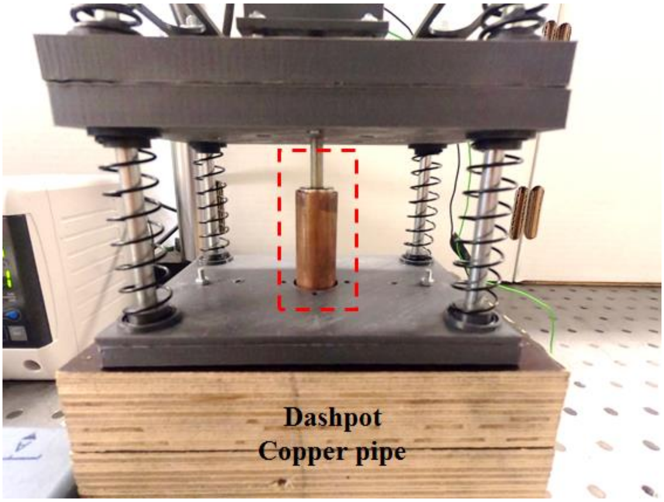

Fig. 4.18 Dashpot from a copper pipe and a magnetic piston

Initially, an impulse test was conducted, and damping is investigated. The response of impulse test – 1 is recorded and presented in Fig. 4.19. Table 4.2 summarizes the damping parameters of impulse test – 1.

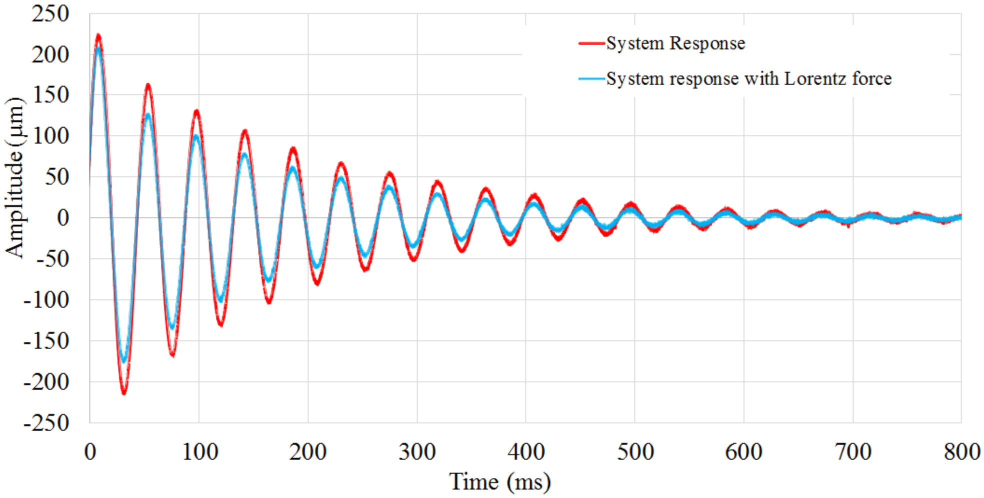

Fig. 4.19 Impulse test – 1: response for the dashpot from a copper pipe

Table 4.2 Damping parameters from impulse test – 1

Nature of system	Damping ratio ς	Damping coefficient c, Ns/m	Natural frequency f_n, Hz
without the Lorentz force	0.00567	3.21064	28.03
with the Lorentz force	0.034783	3.86785	27.75 (damped)

For harmonic excitation, ERM was switched on. By using the ERM controller, the various response of the test setup was analyzed. The first point of resonance was observed around 27 Hz with 40 μm of amplitude. When the dashpot with a copper pipe featuring a wall thickness of 0.2 mm and the magnetic piston were used, then, there was no noticeable attenuation of vibration. The reason for this is the low magnitude of the generated Lorentz force varying within 0–0.26 N (Fig. 4.4) due to micro displacement. In order to increase the counterforce with micro-vibration, either the magnetic piston of higher magnetic flux should be created, or a thicker copper pipe should be used.

4.3.3 Investigation of micro-vibration attenuation by using a two-coil system

A two-coil system is installed into the test setup, as illustrated in Fig. 4.20. Initially, an impulse test was conducted, and damping was investigated. The response of impulse test – 2 is shown in Fig. 4.21.

Table 4.3 summarizes the damping parameters of impulse test – 2.

Table 4.3 Damping parameters from impulse test – 2

Nature of the system	Damping ratio ς	Damping coefficient c, Ns/m	Natural frequency f_n, Hz
without the two-coil system	0.00567	3.21064	28.03
with the two-coil system	0.03627	3.70824	22.6 (damped)

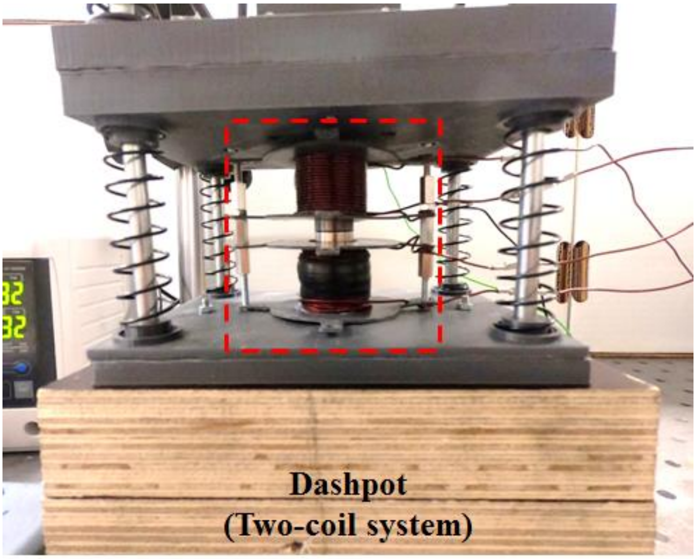

Fig. 4.20 Dashpot of the two-coil system

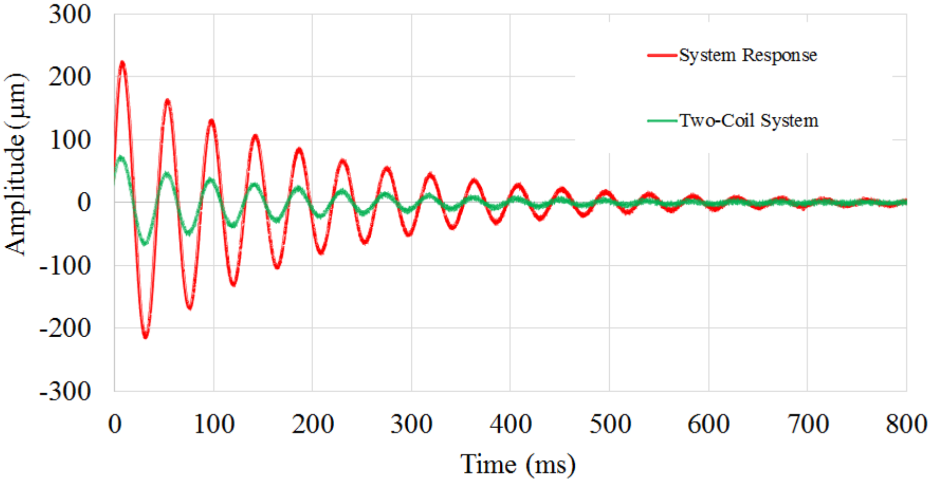

Fig. 4.21 Impulse test – 2 result for the dashpot of the two-coil system

Initially, the harmonic force is generated by using ERM. A response of an amplitude of 40 µm is noticed at 27 Hz. This specific range is considered to test the two-coil system. It should be noted, to generate the required counter force, the two-coil system has limitations, as the counter force generated depends on the magnitude of the current that passes through the coil.

At first, only one coil was excited, which resulted in 43.24% reduction in the amplitude of vibration. Yet, it is clearly visible from Fig. 4.22 that there is a phase shift in the response when using just one coil.

Secondly, by activating two coils simultaneously, a reduction of 81.08% in vibration was observed without any phase shift (Fig. 4.22). Here, both coils were activated with 3 Amp DC current.

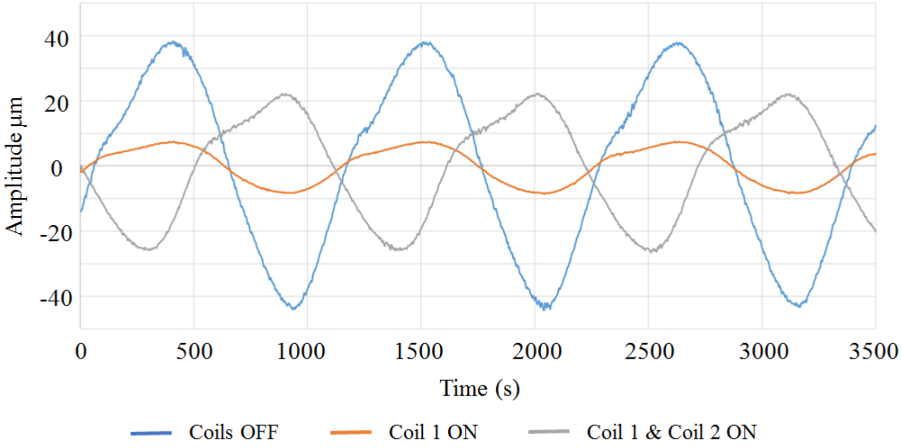

Fig. 4.22 Response plot of the two-coil system

The explanation for reduced vibration in the case of activating the two coils is similar to what was observed in Chapter 2. The system became stiffer, and the resonance of the system shifted, thereby not letting the system vibrate freely with respect to the excited force.

4.3.4 Investigation of heat generated inside the two-coil system

In the previous experiment (Section 4.3.3), it was observed that, after a certain period of continuous use, there was a temperature build-up inside the coil. There are limitations for permanent magnets because the optimal working temperature of the current permanent magnetic setup is below 80 °C. Therefore, it becomes a necessity to investigate the temperature build-up inside the coil with respect to the operating time.

An experimental setup, as shown in Fig. 4.23, is used to study the temperature rise in the two-coil system.

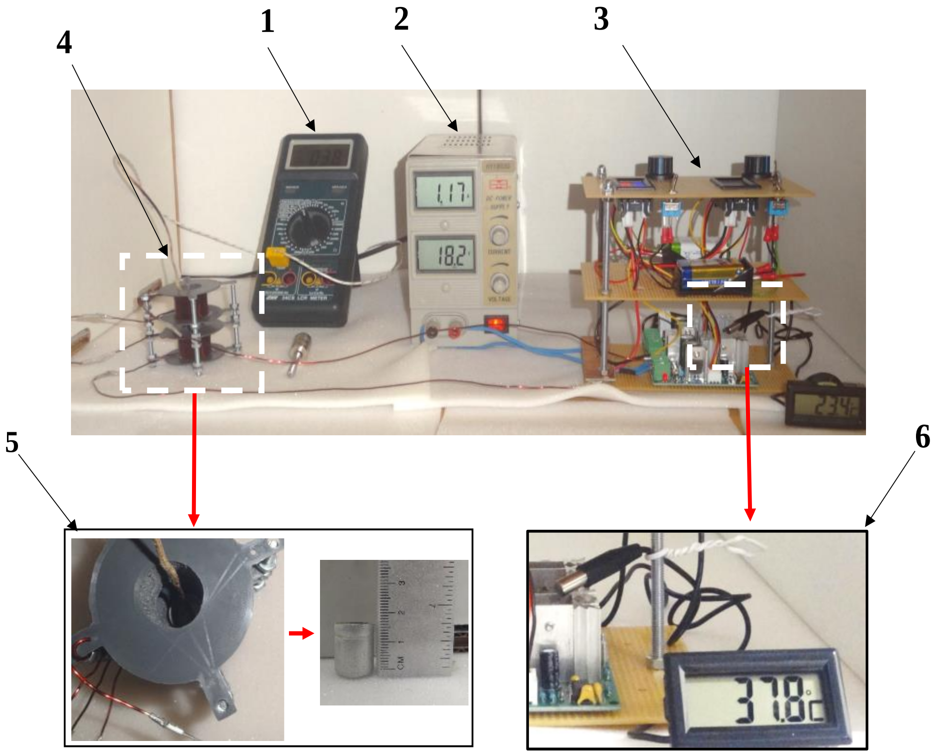

Fig. 4.23 Experimental setup to investigate the temperature build-up in the two-coil system: 1 – CHY 24CS; 2 – power supply; 3 – controller; 4 – two-coil system; 5 – temperature analysis inside the two-coil system; 6 – temperature analysis at the controller

The power source (HY1803D) is connected to the controller, through which, the current passing through the coil and the voltage across the coil is controlled. The temperature inside the two-coil system is measured by using an LCR meter – CHY 24CS model, of accuracy ± 0.1 °C. The probe of the LCR meter is kept in direct contact with an aluminum cap of 0.1 mm wall thickness.

Additionally, the temperature build-up within the controller is also analyzed by using a simple digital thermometer featuring an accuracy of ± 0.5 °C.

Two experiments are considered to evaluate the temperature build-up in the system that includes: investigation of the temperature inside the two-coil system and in the controller. The first experiment uses the conditions from Section 4.4.3, where the current in the coil is around 3 Amp. Analysis of the temperature build-up with respect to time is presented in two tables. Table 4.4 represents the data of the change in the voltage and the current with respect to time from the main power supply and from the controller to the coil.

The results of the temperature build-up inside the coil and in the controller are shown in Table 4.5. The maximum temperature after 1 hour of continuous operation was recorded as 55 °C. After this point, the temperature remained constant.

Table 4.4 First experiment

Main power supply reading (maintained at maximum discharge)	Time, min	Initial Value	After 10'	After 20'	After 35'	After 45'	After 60'
	Voltage, V	18.3	18.3	18.3	18.3	18.3	18.3
	Current, A	0.54	0.6	0.61	0.62	0.62	0.62
Supply voltage through the coil	Voltage, V	0.96	1.12	1.17	1.17	1.19	1.19
	Current, A	3.21	3.40	3.42	3.43	3.43	3.44

Table 4.5 Temperature build-up in the case of the first experiment

Time, min	Temperature of aluminum-cap, °C	Temperature around the heat sink in the controller, °C
0	17 (initial temperature)	18
4' 05"	25	19
4' 56"	30	21.5
7' 25"	35	23.6
10'	40	25.5
13' 30"	45	28.8
19' 55"	50	30.7
30'	53	38.5
42'	54	40.5
46'	54	42.1
60'	55	45.4
1h 07' 30"	55	44.4 (direct contact 59)

In the second experiment, the coils are activated at 5 Amp. It was noticed that there was intense temperature build-up in this case. The temperature on the aluminum piece reached 80 °C in a period of 10 minutes. The observed results are shown in Table 4.6. The temperature kept increasing, and there was a constant temperature rise in the controller as well.

Table 4.6: Second experiment

Main power supply reading (Maintained at maximum discharge)	Time, min	Initial Value	After 10'	After 20'	After 27'	After 45'	After 60'
	Voltage, V	9.5 V	9.1	9.2	3.19	-	-
	Current, A	3.	3.4	3.18	2.17	-	-
Supply voltage through the coil	Voltage, V	2	2.2	2.47	2.17	-	-
	Current, A	5.24	5.3	5.02	5.12	-	-

Table 4.7 Temperature build-up in the case of second experiment

Time, min	Temperature of the aluminum piece, °C	Temperature around the heat sink in the controller, °C
0	18 (Room temperature)	19.5
30"	20	21.4
2'	30	30
2' 30"	35	38
3' 10"	40	43.6
3' 30"	45	46.7
4' 14"	50	51
5'	55	58.4
5' 45"	60	63.2
6' 30"	65	65
7' 15"	70	71.5
8' 30"	75	75.5
9' 21"	77	77
9' 30"	79	78.5
10'	80	79.8
11'	85	84.8
14' 20"	90	87.5
15'	91	89
16'	92	89.7
16' 45"	93	90
17' 50"	94	90.8
18' 55"	95	91.5
20'	96	92.3
21' 30"	97	93.2
23' 30"	98	93.5
24' 45"	99	94.7
26' 30"	100	96.3

As mentioned at the beginning of this section, it is important to evaluate the temperature build-up in the system as the magnets have a limited working temperature range, and, beyond that, the magnets will start losing their magnetic properties. In order to reduce this temperature build-up, either an additional cooling system has to be considered, or else we need to increase the wire gauge and the number of turns in the coil. But, in both cases, the system will become heavier.

Therefore, based on the requirement of the amplitude of the counter force, the coil system must be designed, and the current passing through the coil must be minimal so that the temperature build-up remains constant.

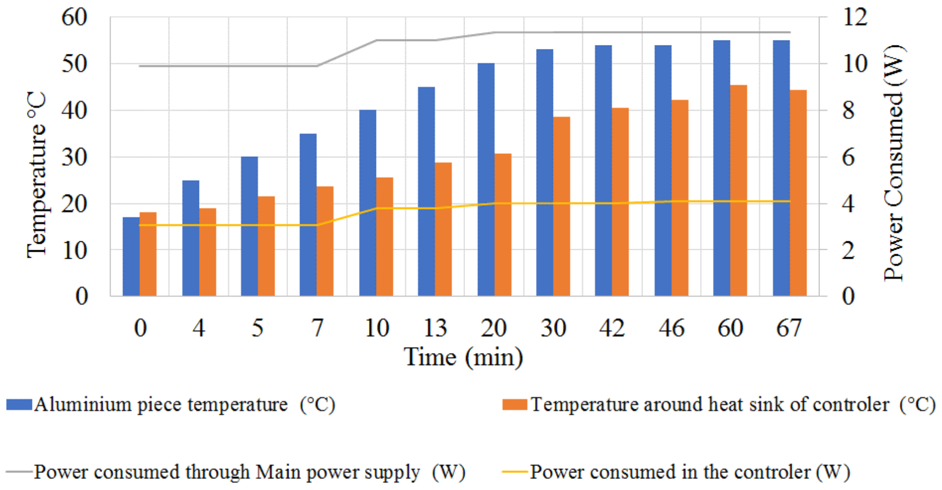

Fig. 4.24 Summary of temperature analysis when the current in the coil is around 3 Amp

A summarized graphical representation of the temperature build-up inside the coil and near the heat sink of the controller along with power consumed from the power supply and through the controller, when the current in the coil is around 3 Amp, is illustrated in Fig. 4.24.

4.3.5 Conclusion of experimental analysis

The mass of the active plate with ERM and the magnetic piston attached to it is 0.6kg, and the sprig constant value of the spring system in use is 5.2023N/m. Therefore, the results achieved from the experiments while using dashpots from a copper pipe (Table 4.2) and the two-coil system (

Table 4.3) can be evaluated and represented in the form of a Bode plot, see Fig. 4.25.

From the Bode plot, the magnitude of resonance for the damped free system is recorded to be 25 dB. When a dashpot from a copper pipe is introduced, then, due to eddy current damping, the magnitude of resonance is reduced to 8 dB without any change in the frequency unit.

In the case of introducing a dashpot from the two-coil system, the peak of resonance was further reduced to 5 dB, but, by a slight increase in the resonance frequency of the system by 3 Hz, the equilibrium position of the system also shifts down by 3 dB. The Bode plot is able to explain that the attenuation from the two-coil system is obtained by a slight change in resonance characteristics as the electromagnetic coil system tries to hold the active plate in its position. In this case, the equilibrium position of the active plate also changes.

From the current results, it can be concluded that, while using dashpots from a copper pipe (eddy current dampers), the magnitude of the vibration can be reduced only within a specific frequency unit, and, on top of that, in order to increase the magnitude of damping, the thickness of the copper pipe or a different grade of magnets with a higher magnetic field has to be used. This in turn increases the mass of the system.

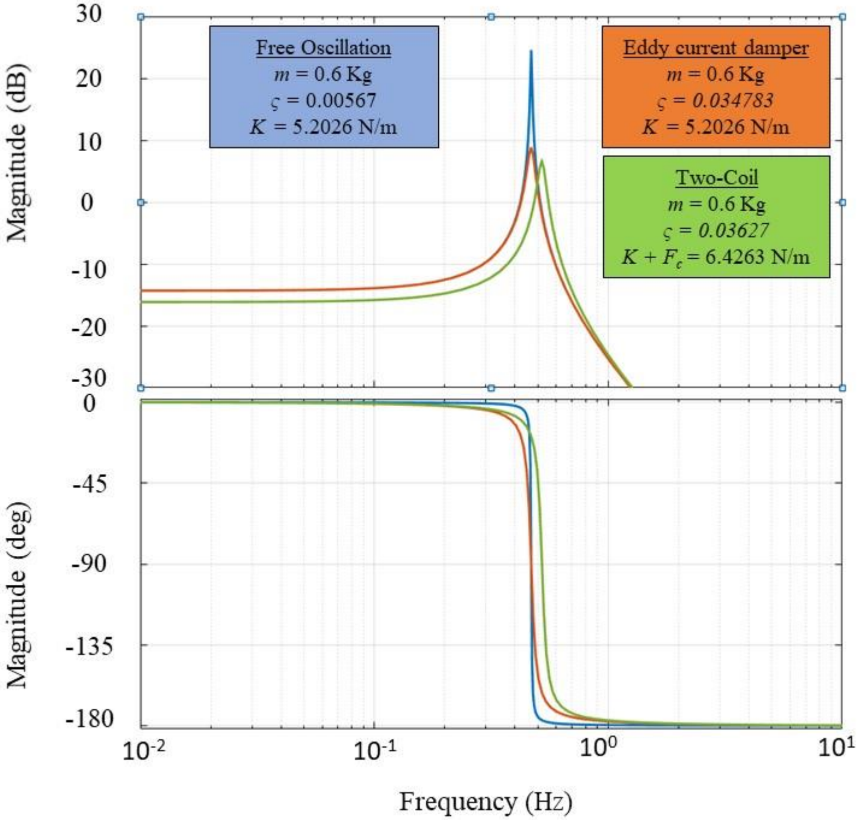

Fig. 4.25 Bode magnitude plot of experimental results

In the case of the dashpot from the two-coil system, the magnitude of the vibration can be reduced for different ranges of frequencies which are within the limit that the system can handle. Here, the frequency limit is defined by the capacity of the electromagnetic device. The main limitation for the two-coil system is the heat generation in the system that can limit the usage by affecting the magnetic properties of permanent magnets. An increase of the parameters of the dashpot can increase the power consumption as well as the mass budget of the system used for attenuation.

4.4 Conclusion of the section

In the current chapter, the possibility to use electromagnetic devices with the objective to create the required counterforce to attenuate vibration by varying the stiffness of the system is investigated. The following points were concluded from this section:

1. Theoretical research for the development of an electromagnetic dashpot by analyzing the Lorentz force in a copper pipe, and the repulsive electromagnetic force generated inside a coil system were conducted.

2. Based on the test requirement, a test setup was designed and developed by considering the following:
    a. design of the magnetic piston;
    b. study of the development of the test setup requirements;
    c. study of the eccentric rotating mass for harmonic excitation, and
    d. analysis of the response of the active plate where the measurements for vibration shall be taken.
3. For experimental analysis, the attenuation of micro-vibration when using the Lorentz force and a two-coil system was investigated. Additionally, heat build-up in the two-coil system was experimentally analyzed so that to study the limitations of the two-coil system.
4. For the comparison of dashpots made from the Lorentz force and a two-coil system, the results obtained from experimental analysis were concluded and represented in the form of a Bode plot. The obtained results confirmed that, for the currently used dashpots, the dashpot from the Lorentz force was able to provide 70% attenuation of the amplitude of vibration without any change in frequency. Whereas, the dashpot from the two-coil system provided 80% attenuation with a slight increase in the resonance frequency of the system by 3 units. For the two-coil system, it was also noticed that there was a shift by 3 units down from the equilibrium position of the system

5. RESEARCH DISCUSSION

The objective of the current research is to investigate the research aim that micro-vibration can be attenuated by shifting the resonance characteristic of a transitional structure which connects the vibration source and the target structure and demands vibration mitigation.

The most common method to achieve attenuation of vibration is by controlling damping ratio ζ and to reduce the vibration within the selected natural frequency of the system. The Bode plot in Fig. 5.1 shows the response of a system with constant mass and stiffness values subjected to a varying damping ratio. For the following values of damping ratio ζ : 0.005, 0.03, 0.08 and 0.12, the observed magnitudes of resonance amplitude were 25 dB, 13 dB, 0.5 dB and -1 dB, respectively.

While working with ζ, attenuation is possible only at a chosen frequency. In other points of natural frequencies, this system is not optimal.

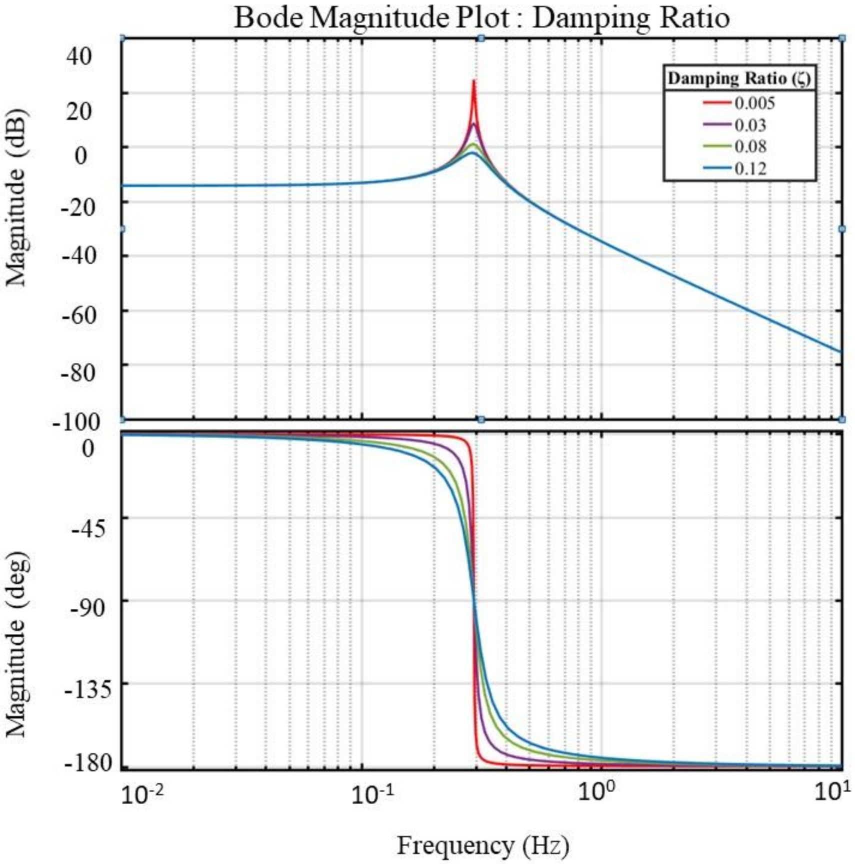

Fig. 5.1 Response of the system by varying damping ratio ζ

Equation (1) (the first chapter) represents the governing equation of an SDOF system with mass M, stiffness k and damping coefficient c which is excited at $F(t) = F_0 \cos(\omega t)$. To attenuate the excitation, external force F_c is introduced in the system. F_c can be achieved with a varying or tuned mass system, varying friction, a composite structure that is able to self-excite, and an electromagnetic dashpot that can exert the required force at specific points.

In order to switch the frequency of the system and to achieve attenuation at different bands of frequencies, a mass tuned damper can be used, where the variation of the mass influences the natural frequency of the system. Figure 5.2 shows the Bode plot where the response of the system with constant stiffness and the damping parameter are subjected to varying values of the mass. The default natural frequency of the system is obtained from 0.6 kg of mass. The natural frequency of the system can be varied by increasing or decreasing the magnitude of the mass. When the mass was varied by 0.6 kg, 1.6 kg, 2.1 kg, and 3.1 kg, the system obtained the following natural frequencies: 2.8 Hz, 1.95 Hz, 1.78 Hz and 1.62 Hz, respectively. The maximum magnitude of resonance obtained under each set of conditions of a varying mass was recorded close to 25 dB.

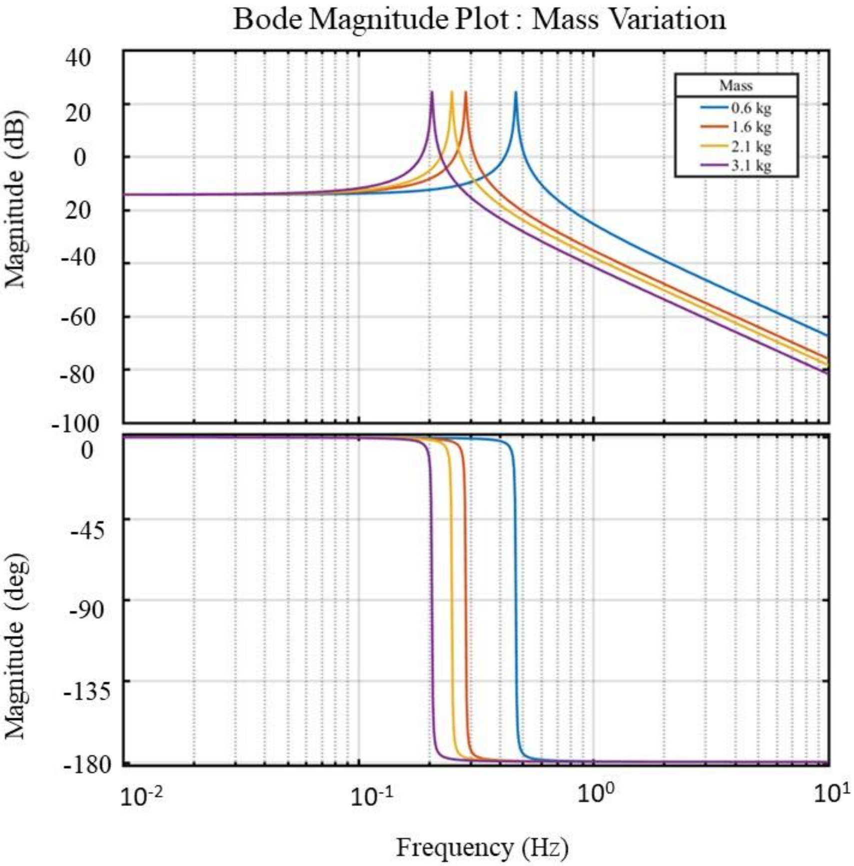

Fig. 5.2 Response of a system by varying the mass

Vibration can also be reduced by the external forces acting on the system. When an external force acts on the system, then the stiffness of the system changes, thereby changing the natural frequency. Also, there will be shifts in the equilibrium position of the system; this is noticeable from the Bode plot above, see Fig. 5.3.

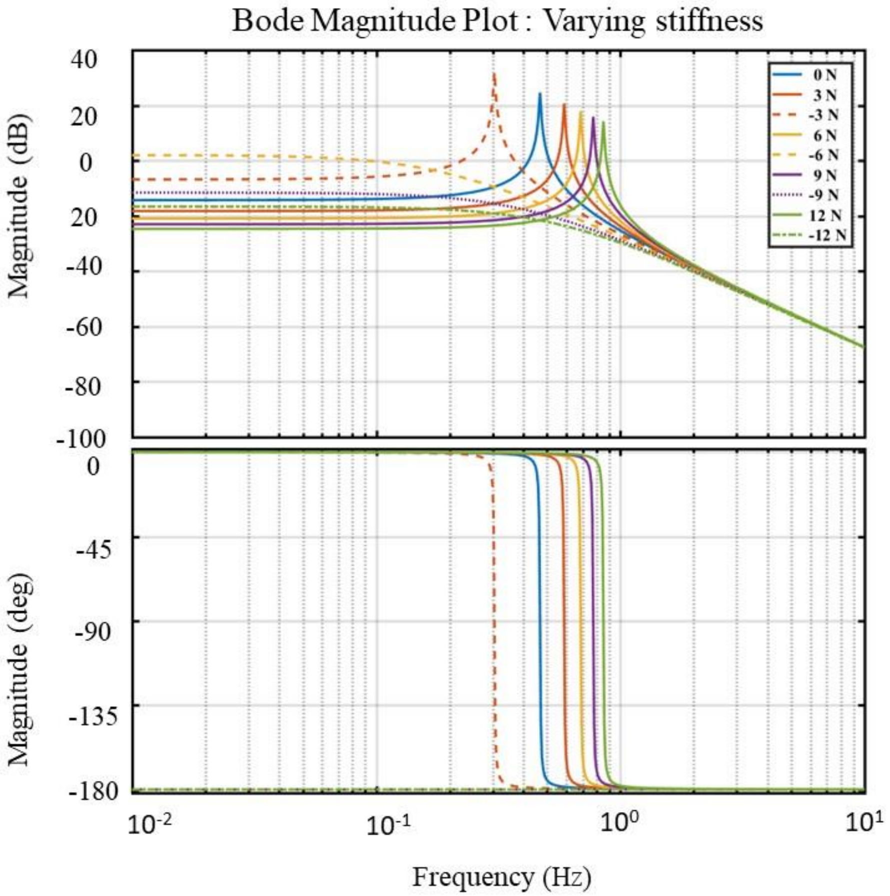

Fig. 5.3 Response of a system under the influence of varying external forces

When there is no force acting on the system, the equilibrium position of the system is -14.32 dB, and the highest magnitude of the system response is recorded to be 24.58 at 2.95 Hz.

When there is an attractive force or a pulling force acting on the system, the magnitude of the equilibrium position shifts from -14.32dB to lower positions. When the system is subjected to attractive forces: 3N, 6N, 9N and 12N, then, the system will possess -18.28 dB, -20.98 dB, -23.04 dB and -24.7dB equilibrium positions, and the highest magnitudes of the system response were recorded as 20.63 dB at 3.89 Hz, 17.92 dB at 4.79 Hz, 15.86 dB at 5.88 Hz and 14.2 dB at 7.08 Hz, respectively.

When the system is subjected to repulsive or pushing forces: -3N, -6N, -9N and -12N, then, the system will possess -6.874 dB, -1.894 dB, -11.61 dB and -16.66 dB equilibrium positions, respectively. The highest magnitude of the system response when the repulsive force is -3 N is recorded to be 27.18 dB at 1.99 Hz. In the case of repulsive forces: -6N, -9N and -12N, the magnitude of the system response recorded a flat curve. The possible explanation for this could be that the system is pushed beyond the stiffness constant of the system where the natural frequency of the highest magnitude of the system lies before 0.01Hz (in the log scale 10^{-2}). This situation is practically impossible to achieve. Therefore, a detailed research focusing on a selected method to generate counterforce and also focusing on its application must be further conducted.

In the current research the idea was to apply an external force to a transitional structure which connects the vibration source and the target structure that demands vibration mitigation. In terms of the practical application of the current hypotheses, there are limitations and difficulties which are clearly understood from previous research works dating back to more than a decade. These research works specifically provide good insight into experiments; our experiments yielded promising results for vibration attenuation in the laboratory environment. Yet, these techniques have not been implemented until now due to the nature of their design, control, dependency, and the maintenance required in the long run.

Therefore, it was necessary to evaluate three different techniques based on the different working principles which include:

a. Structural attenuation (the composite structure);

b. Controlled Coulomb attenuation;

c. Controlled counterforce to attenuate the amplitude of micro-vibration by using an electromagnetic device.

The results from the second chapter (Fig. 2.13 and Fig. 2.14) showed the possibility to attain 50% alleviation in the flutter with a single composite beam and without external shunt circuits for energy dissipation. There, by empirically supporting the proposed research aim, for mitigating the shudder propagating through a transitional composite brace.

The third chapter explains the concept how to increase the frictional force between two steel surfaces by varying the magnitude of the normal force. Here, the magnitude of the normal force is improved by introducing an additional force of attraction F between steel plates by using the method of magnetic latching. The obtained results (shown in Fig. 3.15, Fig. 3.17 and Fig. 3.18) explain the idea how to further implement the concept to attenuate vibration by the method of controlled friction.

The possibility to use electromagnetic devices to control the resonance extremity is analyzed in the fourth chapter. Here, an eddy current damper and an active electromagnetic deceive are theoretically and experimentally investigated. The obtained result (Fig. 4.28) clearly states the difference of using damping or stiffness as control parameters for vibration attenuation.

The three techniques used to generate a counter force have a different working principle and must be used based on design requirements, such as: the space to position the device, the amplitude of oscillation, and the frequency of oscillation. Therefore, it is hard to define the correlation between the three techniques, but, based on the application requirements, the optimal technique can be selected.

The utilization of composite structures is the most supporting technique that goes with the current aim of the research to attenuate micro-vibrations by shifting the resonance characteristic of a transitional structure which connects the vibration source and a target. For the technique of composite structures, the advantages are as follows:

a. The design can be made simple, with less dependency between the modules and a less sophisticated mechanism.
b. The possibilities to provide multiple combinations of direct shunting of the passive and active layers without external shunt circuits result in different possibilities of natural frequencies.

CONCLUSIONS

This research investigated different methods with the objective to develop a system to attenuate micro-vibration by shifting the resonance characteristic of a transitional structure.

1. Through problem analysis, the application of the research aim was defined. Then, literature study for different methods and devices used for micro-vibration control was performed. From the studies, it was observed that the currently available research works do not emphasize the control of mechanical transmissibility by the control of stiffness k. Also, these research works do not emphasize on the methods to generate additional forces to vary stiffness, to attenuate vibrations. Therefore, three different methods capable of fulfilling the research aim were suggested and considered for further investigation, such as: (i) controlling the structural stiffness by using a composite structure; (ii) varying system stiffness through controlled friction; and (iii) controlling stiffness by generating counterforce in the system while using an electromagnetic device.
2. To control the structural stiffness using composite structure, initially, a conceptual design was suggested, from which, the problem to investigate the research aim was defined. For further investigation, a PZT bimorph bender was considered. From the theoretical studies for the mechanism of a PZT bimorph bender, an enhanced constitutive equation by considering the effect of two input voltages with phase shifts was obtained and expressed in the 4x4 matrix format. The equation was verified by using an experimental setup (Experimental setup – 1), where 80% reduction in vibration was observed for numerical analysis, as well as for experimental analysis. Through another experiment (Experimental setup – 2), the aim of the research to attenuate vibration by controlling stiffness was analyzed by direct shunting of the active and passive layers. The result obtained in this test stated that, for an externally excited PZT cantilever beam, 50% reduction in vibration is attainable by the combination of unmediated shunting of the passive and active layers of the PZT bimorph beam.
3. A novel method to control friction between two steel plates using a magnetic latching principle was proposed and investigated in this research. Here, the force of attraction between steel plates was increased by using the method of magnetic latching, thereby, the magnitude of the normal force acting between the plates increased and resulted in better friction. Two different designs were considered so that to theoretically compare the effects of magnetic latching with the direct influence of a magnet through a steel plate. The obtained simulation results in the first theoretical analysis showed that the magnitude of the flux density between the steel plates is $|B|$ = 0.01 T, and, in the second theoretical analysis (the completed magnetic circuit theory), it is $|B|$ = 0.69 T. This shows that that it is possible to obtain a 50% increase in the magnitude of friction through the magnetic latching design.

4. Two existing electromagnetic devices were considered and developed to investigate the process of generating counterforce in the system so that to vary the stiffness. The considered electromagnetic dashpot to create counterforces consisted of an eddy current damper and a two-coil system. The results obtained from experimental analysis were concluded and represented in the form of a Bode plot. The results confirmed that the eddy current damper was able to provide 70% attenuation of the amplitude of vibration without any change in the frequency in the system. Whereas, the dashpot from the two-coil system provided 80% attenuation by a slight increase in the resonance frequency of the system by 3 Hz. For the two-coil system, it was also observed that there was a shift by 3 dB down from the equilibrium position of the system. The observations and the understanding derived from the current research states that the use of the two-coil system is suitable for generating the required counter force so that to vary stiffness and to achieve micro-vibration attenuation.
5. Attenuation of vibrations is possible by varying the damping ratio, varying the mass, and varying the stiffness of the system. With the help of a Bode plot, these three methods were compared and analyzed. All the three methods considered in this research are categorized under varying stiffness of the system. Since these three methods have different working principles, it is hard to achieve correlation, but, based on the design requirements, such as: the space to position the device, the amplitude of oscillation and the frequency of oscillations, the most suitable method could be used. According to the current research, the utilization of smart composite structures is the most supporting technique which supports the current research statement to attenuate micro-vibrations by shifting the resonance characteristic of a transitional structure. By using smart composite structures, the observed advantages were: (a) the design can be implemented within a limited space, and, (b) the possibilities were obtained to provide a multiple combination of direct shunting of the passive and active layers without external shunt circuits, which results in broadening the natural frequency characteristics.

REFERENCES

[1] G. S. Aglietti, R. S. Langley, E. Rogers, and S. B. Gabriel, “Model building and verification for active control of microvibrations with probabilistic assessment of the effects of uncertainties,” *Proc. Inst. Mech. Eng. Part C J. Mech. Eng. Sci.*, 2004.

[2] C. Liu, X. Jing, S. Daley, and F. Li, “Recent advances in micro-vibration isolation,” *Mechanical Systems and Signal Processing*. 2015.

[3] R. G. Cobb *et al.*, “Vibration isolation and suppression system for precision payloads in space,” *Smart Mater. Struct.*, 1999.

[4] G. Smet and S. Patti, “A Mechanisms Perspective on Microvibration-Good Practices and Lessons Learned,” in *Proceedings of the 44th Aerospace Mechanisms Symposium, NASA Glenn Research Center,* 2018, pp. 191–204.

[5] B. De Marneffe, M. Avraam, A. Deraemaeker, M. Horodinca, and A. Preumont, “Vibration isolation of precision payloads: A six-axis electromagnetic relaxation isolator,” *J. Guid. Control. Dyn.*, 2009.

[6] I. A. Abu Hanieh, A. Preumont, and N. Loix, “Piezoelectric Stewart platform for general purpose active damping interface and precision control,” in *European Space Agency, (Special Publication) ESA SP*, 2001.

[7] W. Chi, D. Cao, D. Wang, J. Tang, Y. Nie, and W. Huang, “Design and Experimental Study of a VCM-Based Stewart Parallel Mechanism Used for Active Vibration Isolation,” *Energies*, vol. 8, no. 8, pp. 8001–8019, Jul. 2015.

[8] D. Kamesh, R. Pandiyan, and A. Ghosal, “Modeling, design and analysis of low frequency platform for attenuating micro-vibration in spacecraft,” *J. Sound Vib.*, 2010.

[9] V. Preda, J. Cieslak, D. Henry, S. Bennani, and A. Falcoz, “A H ∞ /μ solution for microvibration mitigation in satellites: A case study,” *J. Sound Vib.*, 2017.

[10] D. Addari, G. S. Aglietti, and M. Remedia, “Experimental and numerical investigation of coupled microvibration dynamics for satellite reaction wheels,” *J. Sound Vib.*, 2017.

[11] W. Shi, L. Wang, Z. Lu, and H. Wang, “Experimental and numerical study on adaptive-passive variable mass tuned mass damper,” *J. Sound Vib.*, vol. 452, pp. 97–111, Jul. 2019.

[12] J. A. B. Gripp and D. A. Rade, “Vibration and noise control using shunted piezoelectric transducers: A review,” *Mechanical Systems and Signal Processing*. 2018.

[13] Y. Wei-ming, W. Bao-shun, and H. Hao-xiang, “Research of mechanical model of particle damper with friction effect and its experimental verification,” *J. Sound Vib.*, vol. 460, p. 114898, Nov. 2019.

[14] Y. G. Wu *et al.*, “Design of semi-active dry friction dampers for steady-state

vibration: sensitivity analysis and experimental studies," *J. Sound Vib.*, vol. 459, p. 114850, Oct. 2019.

[15] B. Yan, H. Ma, N. Yu, L. Zhang, and C. Wu, "Theoretical modeling and experimental analysis of nonlinear electromagnetic shunt damping," *J. Sound Vib.*, vol. 471, p. 115184, Apr. 2020.

[16] C. A. Morales, "Complete results for free and forced vibrations of inerter-added one-degree-of-freedom systems," *J. Vibroengineering*, vol. 21, no. 6, pp. 1564–1573, Sep. 2019.

[17] M. Javanbakht, S. Cheng, and F. Ghrib, "Control-oriented model for the dynamic response of a damped cable," *J. Sound Vib.*, vol. 442, pp. 249–267, Mar. 2019.

[18] I. Valiente-Blanco, J. L. Perez-Diaz, and C. Cristache, "Potential reduction of the inertial mass of tuned vibration absorbers by means of mechanical impedance matching," *J. Sound Vib.*, vol. 442, pp. 90–107, Mar. 2019.

[19] N. G. R. de Melo Filho, L. Van Belle, C. Claeys, E. Deckers, and W. Desmet, "Dynamic mass based sound transmission loss prediction of vibro-acoustic metamaterial double panels applied to the mass-air-mass resonance," *J. Sound Vib.*, vol. 442, pp. 28–44, Mar. 2019.

[20] N. Jalili and D. W. Knowles IV, "Structural vibration control using an active resonator absorber: Modeling and control implementation," *Smart Mater. Struct.*, 2004.

[21] L. Vaillon, C. Champetier, V. Guillaud, J. Alldridge, and C. Philippe, "Passive and active microvibration control for very high pointing accuracy space systems," *Eur. Sp. Agency, (Special Publ. ESA SP*, 1997.

[22] E. F. Crawley and J. De Luis, "Use of piezoelectric actuators as elements of intelligent structures," *AIAA J.*, 1987.

[23] T. Bailey and J. E. Ubbard, "Distributed piezoelectric-polymer active vibration control of a cantilever beam," *J. Guid. Control. Dyn.*, 1985.

[24] K. D. Dhuri and P. Seshu, "Multi-objective optimization of piezo actuator placement and sizing using genetic algorithm," *J. Sound Vib.*, 2009.

[25] S. Hanagud, M. W. Obal, and A. J. Calise, "Optimal vibration control by the use of piezoceramic sensors and actuators," *J. Guid. Control. Dyn.*, 1992.

[26] D. Casagrande, P. Gardonio, and M. Zilletti, "Smart panel with time-varying shunted piezoelectric patch absorbers for broadband vibration control," *J. Sound Vib.*, 2017.

[27] L. Dal Bo, P. Gardonio, D. E. Casagrande, and S. Saggini, "Smart panel with sweeping and switching piezoelectric patch vibration absorbers: Experimental results," *Mech. Syst. Signal Process.*, 2019.

[28] J. H. Griffin, "A Review of Friction Damping of Turbine Blade Vibration,"

Int. J. Turbo Jet Engines, vol. 7, no. 3–4, pp. 297–308, 1990.

[29] D. Laxalde, F. Thouverez, J.-J. Sinou, and J.-P. Lombard, "Qualitative Analysis of Forced Response of Blisks With Friction Ring Dampers," *Eur. J. Mech. A/Solids*, vol. 26, no. 4, pp. 676–687, Jan. 2008.

[30] E. P. Petrov and D. J. Ewins, "Analytical formulation of friction interface elements for analysis of nonlinear multi-harmonic vibrations of bladed disks," *J. Turbomach.*, vol. 125, no. 2, pp. 364–371, Apr. 2003.

[31] J. H. Wang, W. K. Chen, and J. H. Wang Professor W K Chen Graduate Student, "Investigation of the Vibration of a Blade With Friction Damper by HBM," vol. 115, p. 10, 1993.

[32] M. Hutter *et al.*, "ANYmal - toward legged robots for harsh environments," *Adv. Robot.*, 2017.

[33] Y. G. Wu, L. Li, Y. Fan, S. Zucca, C. Gastaldi, and H. Y. Ma, "Design of dry friction and piezoelectric hybrid ring dampers for integrally bladed disks based on complex nonlinear modes," *Comput. Struct.*, vol. 233, p. 106237, Jun. 2020.

[34] L.-Y. Lu, S.-Y. Chu, H.-H. Wu, J.-R. Cheng, and) Taiwan, "Development of a Semi-Active Friction Damper for Seismic Structures by Using Leverage Mechanism," 2017.

[35] G. Biresaw and K. L. Mittal, *Surfactants in tribology*, vol. 3. CRC Press, 2013.

[36] J. Takadoum, *Materials and Surface Engineering in Tribology*. Wiley-ISTE, 2010.

[37] R. Gohar and H. Rahnejat, *Fundamentals of tribology: 2nd edition*. Imperial College Press, 2012.

[38] S. Krishnamoorthy and I. Skiedraite, "Development of electromagnetic damper," *Mechanika*, vol. 21, no. 3, pp. 226–233, 2015.

[39] P. Paul, C. Ingale, and B. Bhattacharya, "Design of a vibration isolation system using eddy current damper," *Proc. Inst. Mech. Eng. Part C J. Mech. Eng. Sci.*, vol. 228, no. 4, pp. 664–675, Mar. 2014.

[40] S. M. M. Mofidian and H. Bardaweel, "Theoretical study and experimental identification of elastic-magnetic vibration isolation system," *J. Intell. Mater. Syst. Struct.*, vol. 29, no. 18, pp. 3550–3561, Nov. 2018.

[41] F. Chen and H. Zhao, "Design of eddy current dampers for vibration suppression in robotic milling," *Adv. Mech. Eng.*, vol. 10, no. 11, Nov. 2018.

[42] P. Gardonio and L. D. Bo, "Scaling laws of electromagnetic and piezoelectric seismic vibration energy harvesters built from discrete components," *J. Sound Vib.*, p. 115290, Mar. 2020.

[43] T. Vyhlídal, D. Pilbauer, B. Alikoç, and W. Michiels, "Analysis and design aspects of delayed resonator absorber with position, velocity or acceleration

feedback," *J. Sound Vib.*, vol. 459, p. 114831, Oct. 2019.

[44] C. N. Loong, J. Shan, Z. Shi, and C. C. Chang, "Approximate analysis of eddy-current force under time-varying velocity motion for structural control," *J. Sound Vib.*, vol. 475, Jun. 2020.

[45] J. Pérez-Díaz, I. Valiente-Blanco, and C. Cristache, "Z-Damper: A New Paradigm for Attenuation of Vibrations," *Machines*, vol. 4, no. 2, p. 12, 2016.

[46] S. Zhu, W. Shen, and Y. Xu, "Linear electromagnetic devices for vibration damping and energy harvesting: Modeling and testing," *Eng. Struct.*, vol. 34, pp. 198–212, 2012.

[47] W. K. Ao and P. Reynolds, "Optimal Analysis, Design and Testing of an Electromagnetic Damper With Resonant Shunt Circuit for Vibration Control of a Civil Structure," pp. 1–8, 2016.

[48] S. Zhu, W. Shen, and X. Qian, "Dynamic analogy between an electromagnetic shunt damper and a tuned mass damper," *Smart Mater. Struct.*, vol. 22, no. 11, 2013.

[49] R. Palomera-arias, J. J. Connor, and J. A. Ochsendorf, "Feasibility study of passive electromagnetic damping systems," *J. Struct. Eng.*, vol. 134, no. January, 2008.

[50] S. Mirzaei, "A flexible electromagnetic damper," in *Proceedings of IEEE International Electric Machines and Drives Conference, IEMDC 2007*, 2007, vol. 2.

[51] A. Hassan, A. Torres-Perez, S. Kaczmarczyk, and P. Picton, "Vibration control of a Stirling engine with an electromagnetic active tuned mass damper," *Control Eng. Pract.*, vol. 51, pp. 108–120, 2016.

[52] S. Zhu, W. Shen, and X. Qian, "Dynamic analogy between an electromagnetic shunt damper and a tuned mass damper," *Smart Mater. Struct.*, vol. 22, no. 11, p. 115018, Nov. 2013.

[53] S. Symalla and M. Liu, "Boundary conditions of the hydrodynamic theory of electromagnetism," *Phys. B Condens. Matter*, vol. 255, no. 1, pp. 132–144, 1998.

[54] H. P. Olesen and R. B. Randall, "A Guide to Mechanical Impedance and Structural Response Techniques (17-179)," *Bruel Kjaer Appl. Note*, 1977.

[55] V. Ostasevicius, R. Didziokas, R. Gaidys, and V. Barzdaitis, "Vibration peculiarity of impacting variable cross section cantilever structure," in *Mechanisms and Machine Science*, 2019.

[56] S. S. Djokoto, E. Dragasius, V. Jurenas, and M. Agelin-Chaab, "Controlling of Vibrations in Micro-Cantilever Beam Using a Layer of Active Electrorheological Fluid Support," *IEEE Sens. J.*, 2020.

[57] S. S. Djokoto, M. Agelin-Chaab, V. Jurenas, and E. Dragasius, "Experimental

Investigation of Squeezed MRF Film Stopper and Its Effect on Vibrating Bimorph for Frequency Tuning of an Energy Generator," in *Conference Proceedings - IEEE SOUTHEASTCON*, 2019.

[58] K. Ragulskis, K. Kanapeckas, R. Jonušas, K. Juzenas, and K. Juz, "VIBRATIONS GENERATOR WITH A MOTION CONVERTER BASED ON PERMANENT MAGNET INTERACTION," *J. Vibroengineering*, vol. 12, no. 1, pp. 124–132, Mar. 2010.

[59] C. A. Morales, "Transmissibility concept to control base motion in isolated structures," *Eng. Struct.*, vol. 25, no. 10, pp. 1325–1331, Aug. 2003.

[60] M. A. Mitiu and D. Comeaga, "The control of transmissibility and mechanical impedance using electrodynamic actuators," in *2013 - 8th International Symposium on Advanced Topics in Electrical Engineering, ATEE 2013*, 2013.

[61] H. M. Zheng, D. D. Dong, and L. H. Zhu, "Tunable stiffness and damping vibration control strategy based on magnetorheological elastomer isolator," in *Applied Mechanics and Materials*, 2014.

[62] D. F. Ledezma-Ramírez, N. S. Ferguson, and M. J. Brennan, "Vibration decay using on-off stiffness control," in *Proceedings of ISMA2006: International Conference on Noise and Vibration Engineering*, 2006.

[63] A. Ramaratnam and N. Jalili, "A switched stiffness approach for structural vibration control: Theory and real-time implementation," *J. Sound Vib.*, 2006.

[64] C. W. Song and S. Y. Lee, "Design of a solenoid actuator with a magnetic plunger for miniaturized segment robots," *Appl. Sci.*, 2015.

[65] J. Ajitsaria, S. Y. Choe, D. Shen, and D. J. Kim, "Modeling and analysis of a bimorph piezoelectric cantilever beam for voltage generation," *Smart Mater. Struct.*, vol. 16, no. 2, pp. 447–454, Apr. 2007.

[66] Q. M. Wang and L. Eric Gross, "Constitutive equations of symmetrical triple layer piezoelectric benders," *IEEE Trans. Ultrason. Ferroelectr. Freq. Control*, vol. 46, no. 6, pp. 1343–1351, 1999.

[67] R. Dunsch and J. M. Breguet, "Unified mechanical approach to piezoelectric bender modeling," *Sensors Actuators, A Phys.*, vol. 134, no. 2, pp. 436–446, Mar. 2007.

[68] P. De Lit, J. Agnus, and N. Chaillet, "The constitutive equations of a piezoelectric duo-bimorph," in *Proceedings of the IEEE International Symposium on Assembly and Task Planning*, 2003, vol. 2003-January, pp. 1–6.

[69] S. A. Rios and A. J. Fleming, "A novel electrical configuration for three wire piezoelectric bimorph micro-positioners," in *2014 IEEE/ASME International Conference on Advanced Intelligent Mechatronics*, 2014, pp. 1452–1457.

[70] B. Ghosh, R. K. Jain, S. Majumder, S. S. Roy, and S. Mukhopadhyay,

"Experimental performance evaluation of smart bimorph piezoelectric actuator and its application in micro robotics," *Microsyst. Technol.*, vol. 23, no. 10, pp. 4619–4635, 2017.

[71] U. Kenji, *Ferroelectric devices*, no. April 2013. 2000.

[72] T. L. Schmitz and K. S. Smith, *Mechanical Vibrations*. 2012.

[73] S. Mustapha and L. Ye, "Bonding piezoelectric wafers for application in structural health monitoring-adhesive selection," *Res. Nondestruct. Eval.*, 2015.

[74] "Johnson Matthey Piezo technical sheet [www.piezoproducts.com]."

[75] V. Steffen and D. J. Inman, "Optimal Design of Piezoelectric Materials for Vibration Damping in Mechanical Systems," *J. Intell. Mater. Syst. Struct.*, vol. 10, no. 12, pp. 945–955, Dec. 1999.

[76] E. P. Furlani, *Permanent magnet and electromechanical devices : materials, analysis, and applications*. Academic, 2001.

[77] H. C. Lovatt and P. A. Watterson, "Energy stored in permanent magnets," *IEEE Trans. Magn.*, vol. 35, no. 1 PART 2, pp. 505–507, 1999.

[78] P. Campbell, "Comments on energy stored in permanent magnets," *IEEE Trans. Magn.*, vol. 36, no. 1 PART 2, pp. 401–403, 2000.

[79] I. S. Shanker Ganesh Krishnamoorthy, "Investigation of Permanent Magnet Levitating Inside Solenoid," in *Proceedings of 20th International Conference. Mechanika*, 2015, pp. 170–175.

[80] "Friction and Friction Coefficients." [Online]. Available: https://www.engineeringtoolbox.com/friction-coefficients-d_778.html. [Accessed: 10-Apr-2020].

[81] R. W. Carpick, E. E. Flater, J. R. Vanlangendon, and M. P. De Boer, "Friction in MEMS: From Single to Multiple Asperity Contact."

[82] R. W. Carpick, D. F. Ogletree, and M. Salmeron, "A general equation for fitting contact area and friction vs load measurements," *J. Colloid Interface Sci.*, vol. 211, no. 2, pp. 395–400, Mar. 1999.

[83] M. Erdmann, "Multiple-point contact with friction: Computing forces and motions in configuration space," in *1993 International Conference on Intelligent Robots and Systems*, 1993, pp. 163–170.

LIST OF PUBLICATIONS

Indexed in the Web of Science with Impact Factor

1. **Krishnamoorthy Shanker Ganesh**; Skiedraite Inga. Attenuation of micro-vibration by varying the resonance extremity of a transitional composite structure // Mechanics of advanced materials and structures. Philadelphia, PA: Taylor & Francis. ISSN 1537-6494. eISSN 1537-6532. 2020, vol. 00, p. 1–11. DOI:10.1080/15376494.2020.1716416. [Science Citation Index Expanded (Web of Science); Scopus] [IF: 2.873; AIF:3.477; IF/AIF: 0.826; Q1 (2018, InCites JCR SCIE)] [Science field: T009] [Input: 0.500]
2. Skiedraitė Inga; **Krishnamoorthy Shanker Ganesh**; Kondratas Alvydas; Diliūnas Saulius; Skvireckas Ramūnas. Friction between steel plates under the influence of magnetic field //Mechanika. Kaunas: KTU. ISSN 1392-1207. eISSN 2029-6983. 2017, vol. 23, iss. 2, p. 305–309. DOI: 10.5755/j01.mech.23.2.13839. [Science Citation Index Expanded (Web of Science); Scopus; Academic Search Complete] [IF: 0.529; AIF: 2.663; IF/AIF: 0.198; Q4 (2017, InCites JCR SCIE)] [Science field: T009] [Input: 0.200]

Articles in other peer-reviewed scientific publications

1. **Krishnamoorthy Shanker Ganesh**; Skiedraitė Inga; Djokoto Sylvester Sedem; Dragašius Egidijus; Skvireckas Ramūnas. Study of change in resonance characteristics for a passive bimorph damper

Articles in conference proceedings

1. Skiedraitė, Inga; **Krishnamoorthy, Shanker Ganesh**; Kondratas, Alvydas. Research of frictional force in respect to magnetized surface // Solid state phenomena : Mechatronic systems and materials VII : selected, peer reviewed papers from the 11th international conference Mechatronic Systems and Materials (MSM 2015), July 7–9, 2015, Kaunas, Lithuania / edited by I. Skiedraite, E. Dragašius, L. Zubrickaitė. Zurich: Trans Tech Publications. ISSN1012 - 0394. e ISSN1662-9779. 2016, vol. 251, p. 8–93. DOI:10.4028/www.scientific.net/SSP.251.89. [Scopus; Applied Science & Technology Source; IndexCopernicus][Science field: T009] [Input: 0.333].
2. **Krishnamoorthy Shanker Ganesh**; Skiedraitė Inga; Kondratas Alvydas. Analysis of electromagnetic force in the dashpot // Mechanika 2017: proceedings of the 22nd international scientific conference, 19 May 2017, Kaunas University of Technology, Lithuania / Kaunas University of Technology, Lithuanian Academy of Science, IFTOMM National Committee of Lithuania, Baltic Association of Mechanical Engineering. Kaunas: Kaunas University of Technology. ISSN 1822-2951. 2017, p. 201–204. [Science field: T009] [Input: 0.334]

3. **Krishnamoorthy Shanker Ganesh**; Mayalil Justin Mathews; Baltrukonis Justas. Damping force inside an energy harvesting damper // Pramonės inžinerija 2016 [e-resource]: a conference of junior researchers, 28 April 2016: book of presentations / Kauno technologijos universitetas. Mechanikos inžinerijos ir dizaino fakultetas. Kaunas: Kauno technologijos universitetas. ISSN 2538-6727. 2016, p. 108–111.DOI: 10.5755/e01.25386727. [Science field: T009, N002] [Input: 0.334]

UDK 62-752(043.3)

SL344. 2021-*-*, * leidyb. apsk. l. Tiražas * egz. Užsakymas * .
Išleido Kauno technologijos universitetas, K. Donelaičio g. 73, 44249 Kaunas
Spausdino leidyklos „Technologija“ spaustuvė, Studentų g. 54, 51424 Kaunas